KGi--192.

MEASUREMENTS OF AURORAL PARTICLES BY MEANS OF SOUNDING ROCKETS OF MOTHER–DAUGHTER TYPE

A. Falck

KGI REPORT 192
NOVEMBER 1985

KIRUNA GEOPHYSICAL INSTITUTE
KIRUNA SWEDEN

MEASUREMENTS OF AURORAL PARTICLES BY MEANS OF SOUNDING ROCKETS OF MOTHER-DAUGHTER TYPE

by

A. Falck
Kiruna Geophysical Institute
P.O. Box 704, S-981 27 KIRUNA, Sweden

KGI Report 192
November 1985

Printed in Sweden
Kiruna Geophysical Institute
Kiruna 1985
ISSN 0347-0405

Contents

	Page
1. Presentation of the S17 payloads	3
1.1 The scientific objective of the sounding rockets S17	3
1.2 S17 experiments	3
1.3 Physical characteristics of the payloads	3
1.4 Physical characteristics of the Nike-Tomahawk rocket	5
1.5 Nominal characteristics of flight events	7
1.6 Attitude measurements	8
1.7 Separation of the two payload units	20
1.8 Telemetry and data analyzing technique	33
2. Description of the instrumentation for the particle experiments in the S17 payloads	38
2.1 General theory of CEM - detectors	38
2.2 Calibration of the CEM - detectors	42
2.3 Solid state detectors in S17 payloads	44
2.4 Mounting of the detectors	48
2.5 The efficiency of channel multipliers	48
3. Review of the geophysical conditions during the S17 flights and presentation of some supporting observations	51
3.1 The auroral situation during S17 flights	51
3.2 Magnetic activity	51
3.3 Other supporting observations	56
3.4 The lowlightlevel-TV-system	56
4. Particle fluxes and electric currents coupling the magnetosphere and the ionosphere during a magnetospheric substorm	66
4.1 Review of some substorm terminology and definitions	66
4.2 Reference and comparisons of S17-2 measurements with the results of the IMS-study	75
4.3 Comparison of simultaneous particle observations at low ionospheric altitude (S17-1) and at the magnetic equatorial region (ATS-6)	91
4.4 Summary and conclusions	99
5. Spatial and temporal variations in the particle fluxes detected by the mother-daughter payloads	101
5.1 The mother - daughter philosophy	101
5.2 A trapped particle's motion along the magnetic field line	106
5.3 Discrimination between spatial and temporal variations in the fluctuations of the particle fluxes	107
5.4 Cross-correlation of data of electron fluxes ot different energies obtained on the same payload	109
5.5 Some selected analyses of S17 data implicating the fluctuations to be temporal variations or spatial structures	110
5.6 Summary of precipitated particles and electric field measurements by the rocket S17-1	122
5.7 Conclusions	129
References	131

1. Presentation of the S17 payloads

1.1 The scientific objective of the sounding rockets S17

The scientific objective of the S17 payloads was to study the ionosphere during auroral situations and especially with regards to the local fine structure and a possible separation of spatial and temporal variations of auroral phenomena. The desire to reach such a resolution of the auroral phenomena in time and space has created a payload construction with two separate units, called the mother and the daughter (see Figure 1.1). The daughter was separated from the mother payload during flight and carried its own set of experiments and telemetry system. The institutions taking part in the scientific projects with the two S17 sounding rockets were Kiruna Geophysical Institute (KGI) Sweden, Royal Institute of Technology (KTH) Sweden, Uppsala Ionospheric Observatory (UJO) Sweden and University of California San Diego (UCSD) USA.

1.2 S17 experiments

The S17 payloads were equipped with the following experiments: a) Determination of energy spectrum and pitch-angle distribution of energetic particles, in both mother and daughter (L. Andersson, R. Lundin and A. Falck, KGI); b) Measurements of the electric field, plasma temperature and density by means of a double probe experiment, in both mother and daughter (U. Fahlesson, KTH, in scientific cooperation with university of California); c) Measurements of electron and ion concentrations by means of a probe experiment in both mother and daughter (L. Björn, UJO).

1.3 Physical characteristics of the payloads

Below are listed the main physical parameter values of the S17 payloads.

Mother payload weight	43.6 kg
Daughter payload weight	39.3 kg
Total payload weight	105 kg
Diameter	305 mm
Length	2427 mm

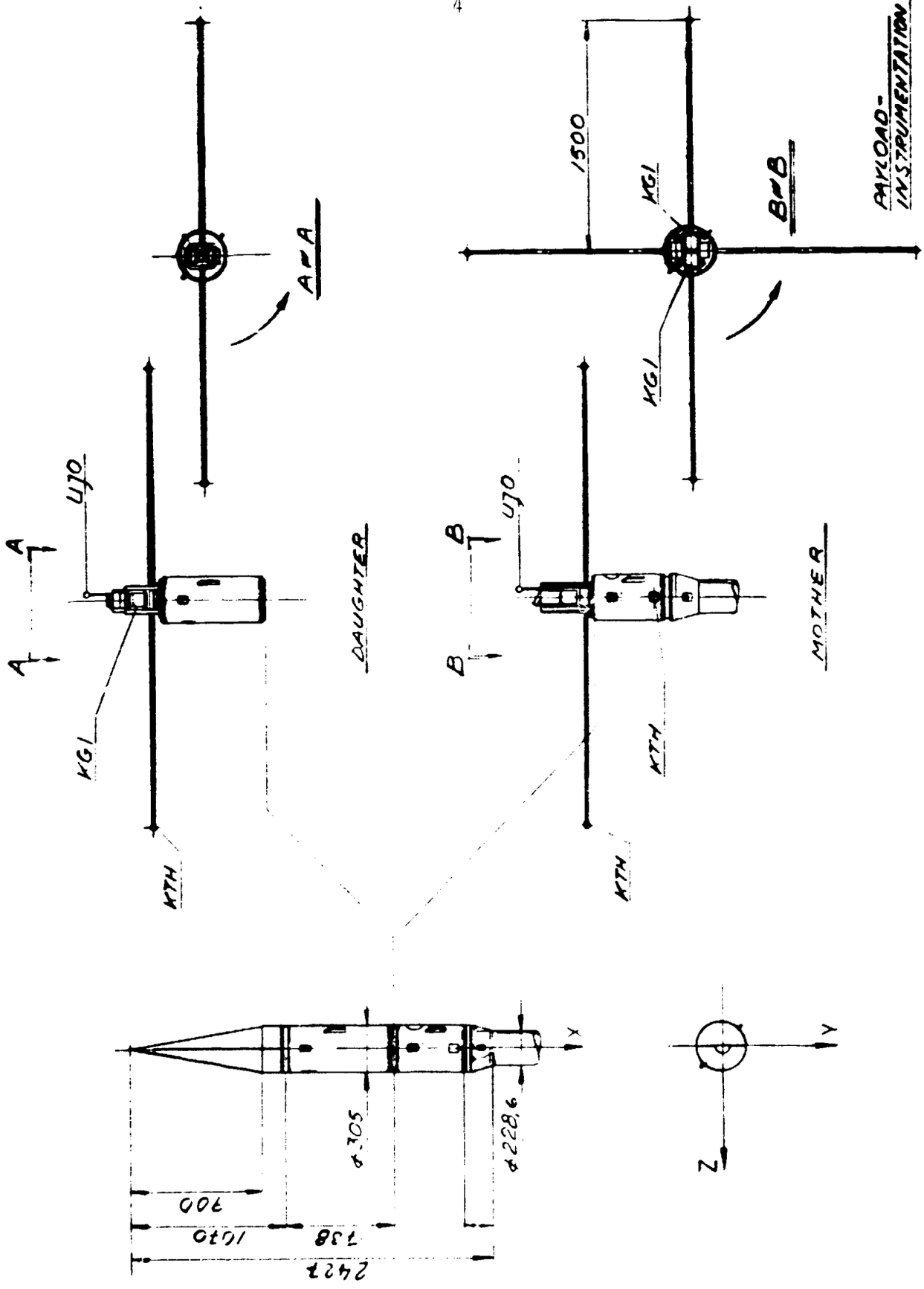

Figure 1.1. Payload S 17.

Telemetry

a) Mother payload

Telemetry system:	PCM/FM		
Frequency:	230.33 MHz		
Power:	2-3 W	PCM-Format:	
Antenna type:	quadraloop	Wordlength:	8 bits
Polarization:	linear	Word/frame:	34
Bit rate:	204.8 kbits/s	Frames/subframe:	32

b) Daughter payload

Telemetry system:	PCM/FM		
Frequency:	400.55 MHz		
Power:	2-3 W	PCM Format:	
Antenna type:	quadraloop	Wordlength:	8 bits
Polarization:	linear	Word/frame	34
Bit rate:	128 kbits/s	Frames/subframe:	16

The S17 payloads were carried by sounding rockets of the type Nike-Tomahawk (see Figure 1.3). The two rockets were successfully launched on January 22, 1976 (S17-1) and on March 6, 1976 (S17-2).

1.4 Physical characteristics of the Nike-Tomahawk rocket

The Nike-Tomahawk vehicle is a two stage rocket, where the Nike is the first stage. Both are solid propellant radial-burning rockets which are ignited with 5 amp squibs. A delay mechanism in the second stage gives Tomahawk ignition approximately 18 seconds after take-off.

Principal data for the rockets:

	Nike	Tomahawk
Length	3.783	3.57 m
Diameter	0.419 m	0.229 m
Gross weight	596 kg	221 kg
Propellant weight	330 kg	177 kg
Burning time	3.5 s	9 s

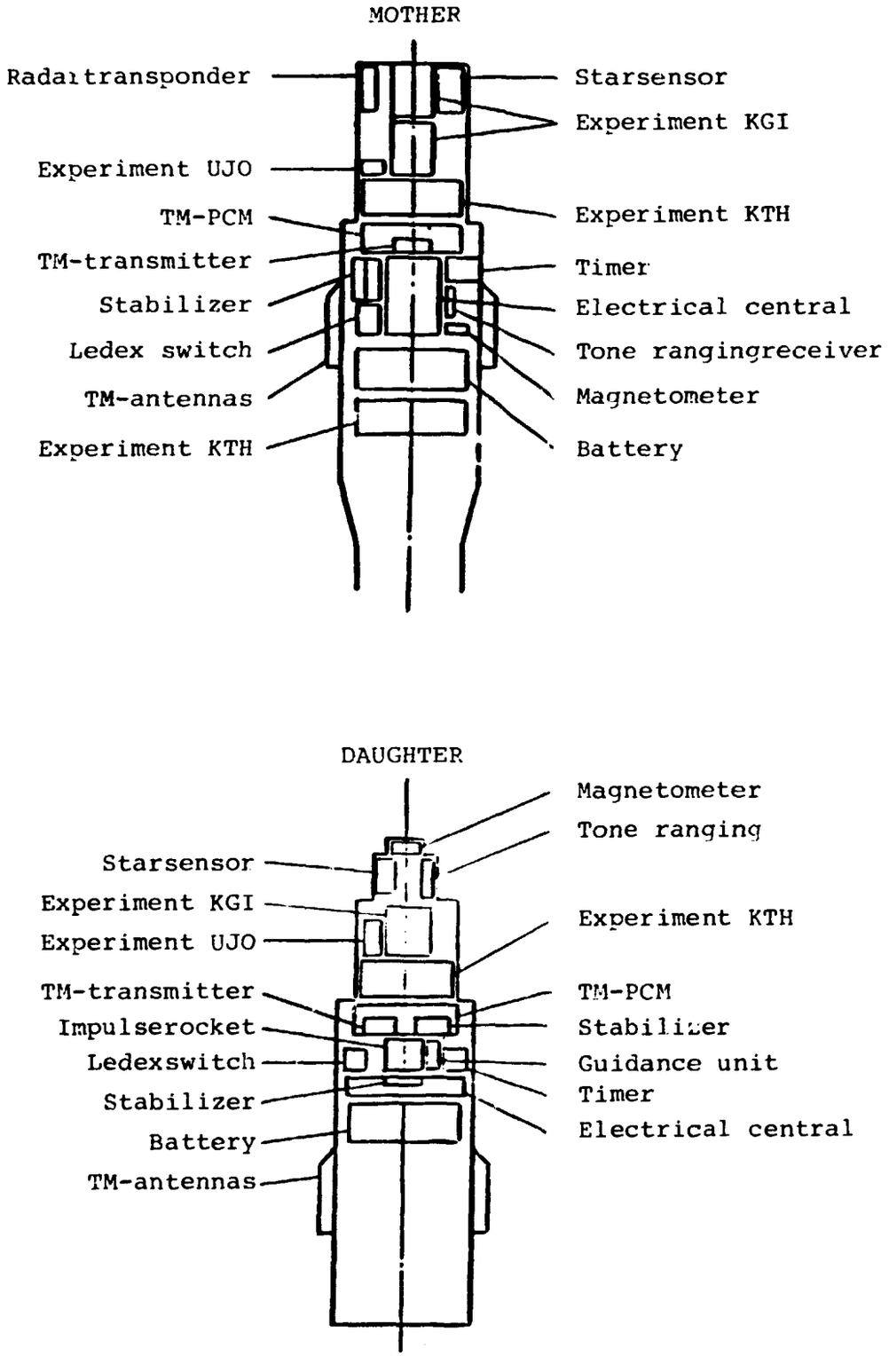

Figure 1.2. The location of the experiments in the S17 payloads.

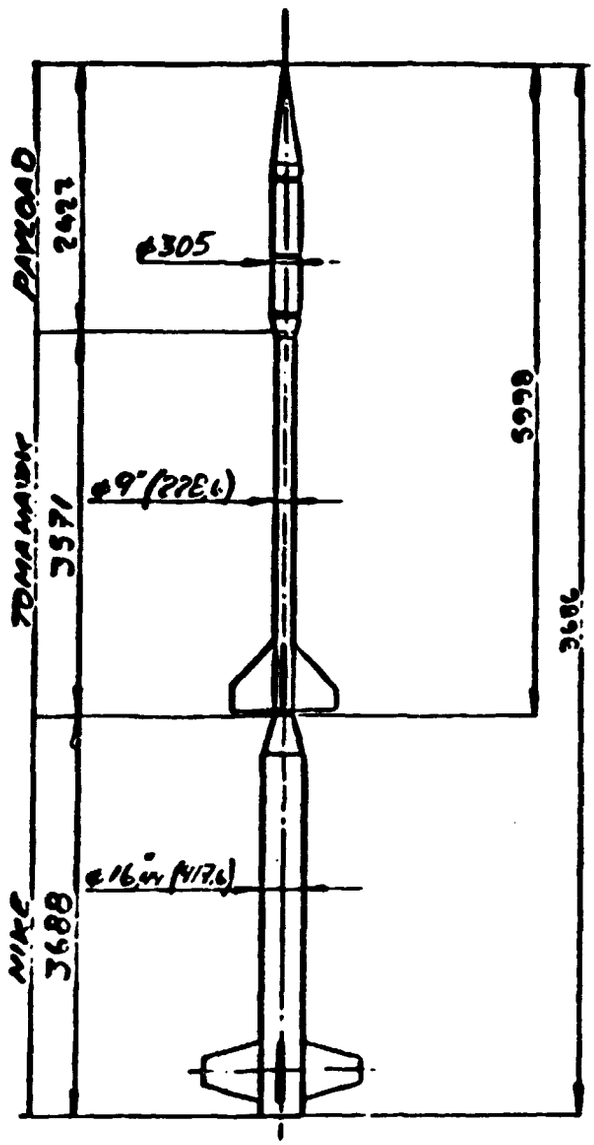

Fig. 1.3 A Nike-Tomahawk sounding rocket with S17 payload.

The interstage frustum is bolted to the front of the Nike motor and slips into the nozzle of the Tomahawk. The two stages are drag separated at Nike burn out.

1.5 Nominal characteristics of flight events

	time	altitude
Start de-spin unit	45.8 s	56 km
Nose-cone separation	48.2 s	60 km
Daughter payload separation	49.3 s	62 km
Apogee	236 s	222 km
Tomahawk separation	429 s	50 km

1.6 Attitude measurements

Both the mother and the daughter payload were equipped with a magnetometer for measurements of the angle between the spin axis of the payload and the earth's magnetic field. The mounting and the location of the magnetometers in the payloads are shown in Figures 1.2, 1.4 and 1.5 and Figure 1.6.

Notice the deviation of the nominal mounting angle for the x-axis of the magnetometer in the daughter payloads. Nominal angle was 0° but for S17 1D it was 23.6° and for S17 2D it was 34° (see Figure 1.5). Empirically was found that the magnetometers in the mother payloads were disturbed by metals in the attachment ring in the internal structure of the rocket. The disturbance was not seen at the calibration of the instruments.

A new type of attitude calculation was used for the first time in the S17 projects. That was a star sensor which was developed and built at KTH (K. Hyyppä, 1975) in cooperation with SSC. Such a star sensor was mounted on the top of both the mother and the daughter payloads (see Figure 1.2).

The star sensor worked well and gave very good accuracy of the angle calculation (0.1°) at an attitude reconstitution which was made for S17-1 and S17-2 mother payloads (B. Schmidtbauer, 1977). The attitude angles calculated from the star sensors in the mother payloads are in good agreement with the results from the determination of the attitude based on magnetometer data from the payloads.

For the star sensor the inertial frame had its x-axis in the direction of the vernal equinox (VE) and the z-axis pointing towards the celestial north pole (NP). The y-axis was chosen so as to complete an orthogonal righthand triad (Figure 1.6). The x-axis of the body frame was pointing along the major axis of minimum moment of inertia, also called the "spin" axis S.

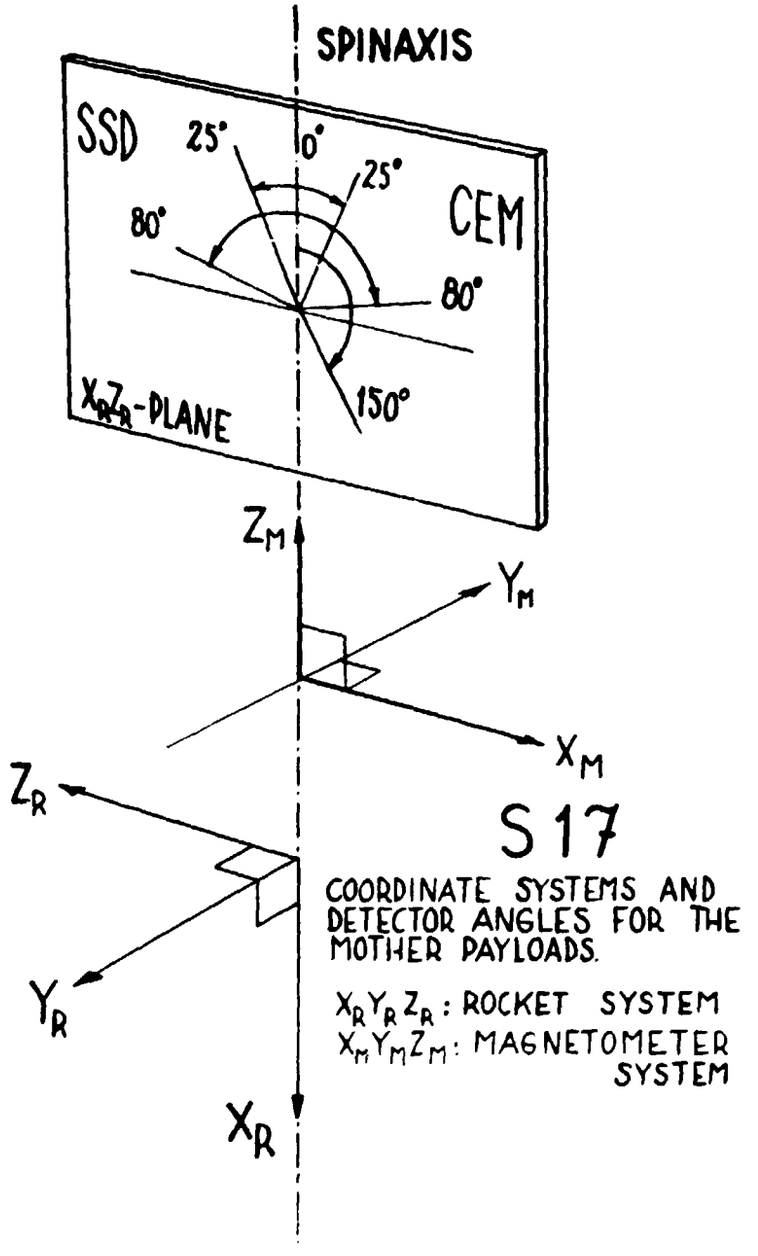

Figure 1.4. The rocket body frame of reference and the mounting of the detectors and the magnetometer. Mother payload.

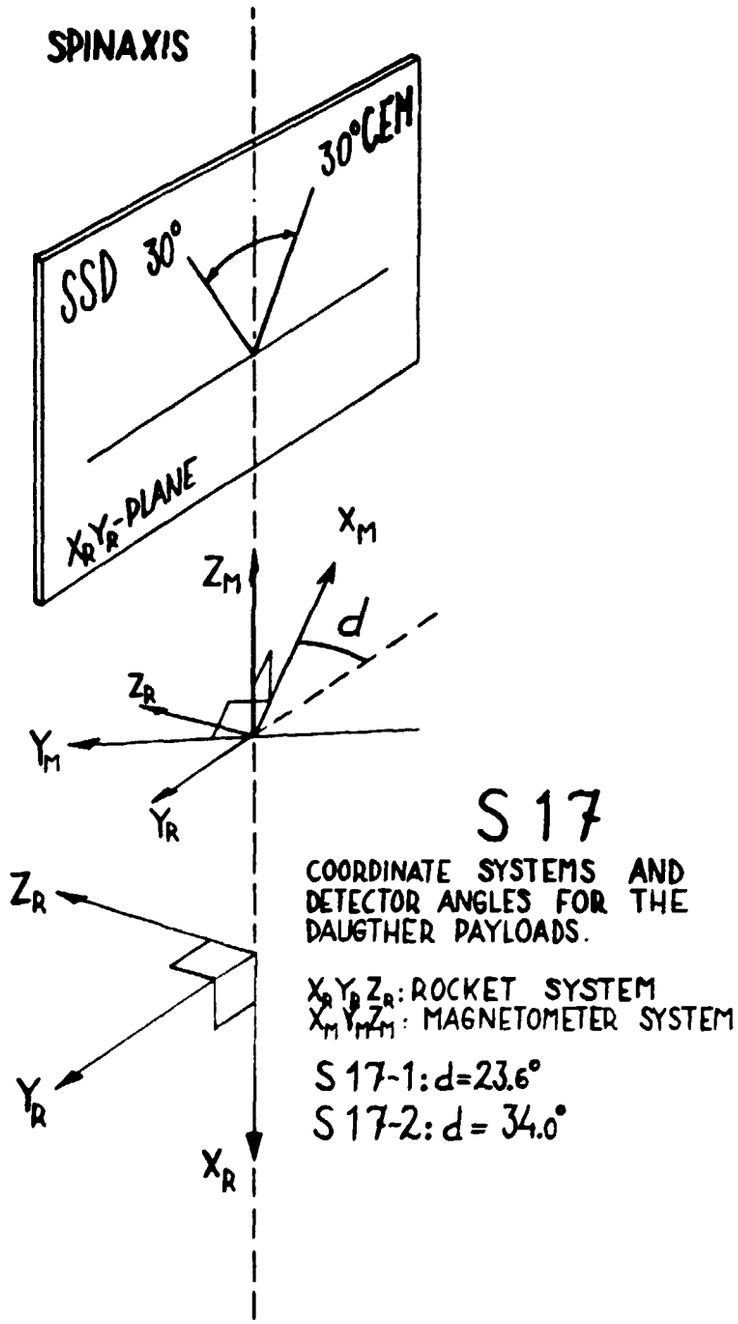

Figure 1.5. The rocket body frame of reference and the mounting of the detectors and the magnetometer. Daughter payload.

The y-axis was defined by being orthogonal both to x and the star sensor optical axis SS. The z-axis complete a right hand orthogonal triad (Figure 1.6). The attitude angles are defined as follows:

RA is the right ascension of the angular momentum vector H,

DE is the declination of the angular momentum vector H,

CRA is the coning rotation angle with respect to the H-direction,

CA is the coning (half-)angle and

BRA is the body rotation angle with respect to the "spin" axis S.

Graphical plots of the estimated attitude angle time histories are included in Figures 1.7 - 1.11. To permit an easy access to attitude in computer programs the attitude angles have been approximated by polynomials in the time variable (t seconds). The attitude angle expressions (in radians unless otherwise stated) were as follows for the S17-1 (mother) payload:

RA = 0.8791 (=50.37 degrees) DE = 1.2556 (=71.94 degrees)

$CRA = -44.841 + 0.209680\ t - 5.251 \cdot 10^{-7} t^2$

$CA = 0.1054 + 1.127 \cdot 10^{-4} t$

$BRA_1 = -337.322 + 20.996569\ (t-200) + 6.320 \cdot 10^{-4}\ (t-200)^2 + 1.121 \cdot 10^{-6}\ (t-200)^3$

$BRA_2 = -377.270 + 20.969698\ (t-200) - 1.501 \cdot 10^{-4}\ (t-200)^2 - 1.47 \cdot 10^{-7}\ (t-200)^3$

Due to the occurence of an instantaneous configurational change at t=202 s, different expressions have to be given for the body rotation angle before (BRA_1) and after (BRA_2) this instant.

a/

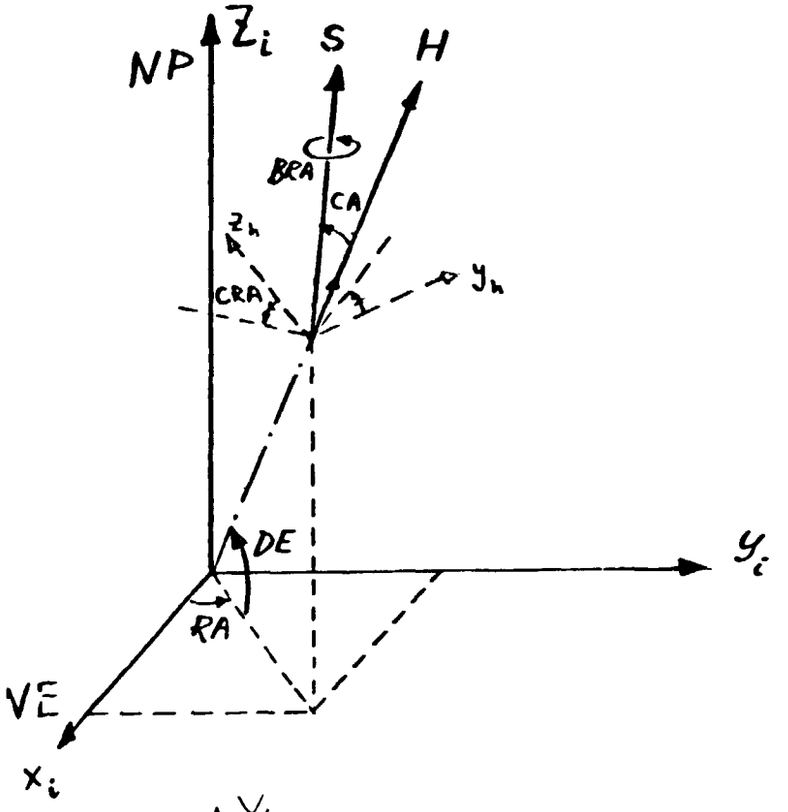

b/

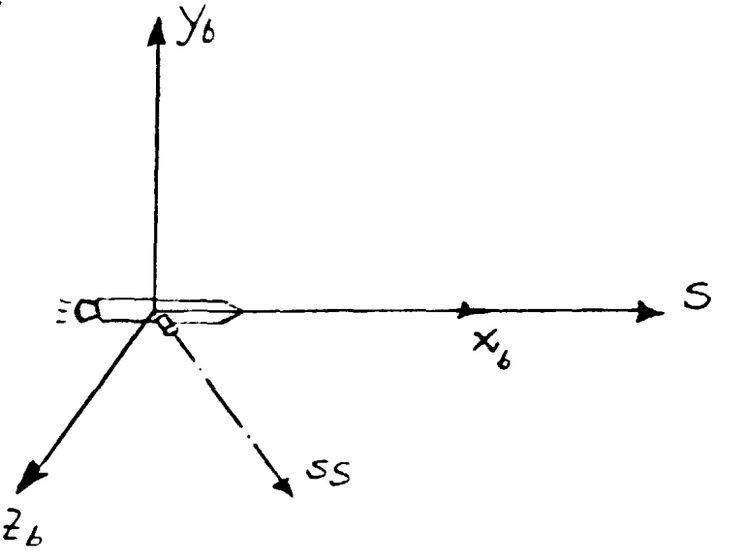

Figure 1.6. a) The coordinate axis for the inertial reference frame

b) The coordinate axis for a body fixed reference frame of the star sensor.

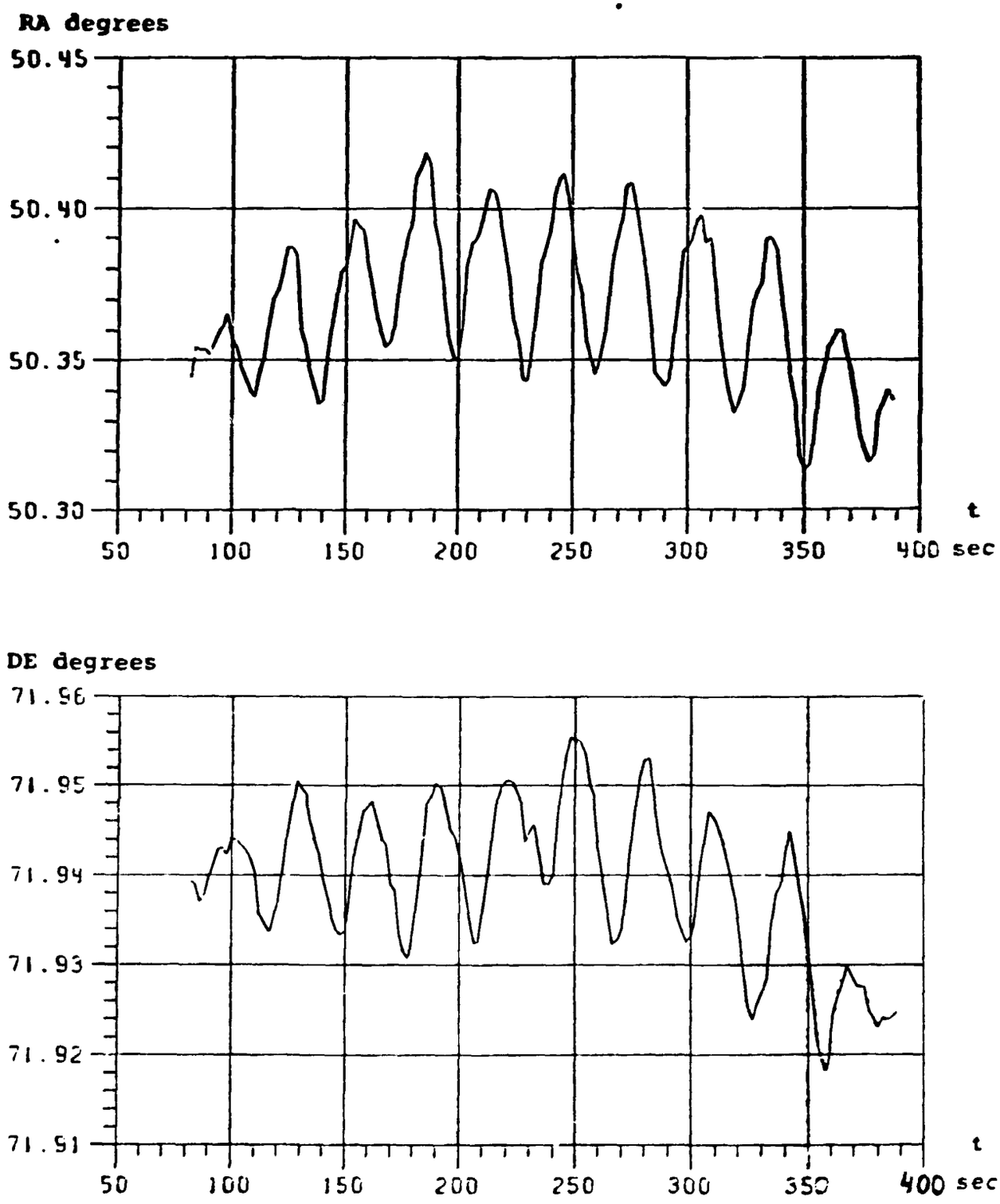

Figure 1.7. Calculated attitude angles for S17-1 (mother payload) based on star sensor data (courtesy of B. Schmidtbauer, 1977).

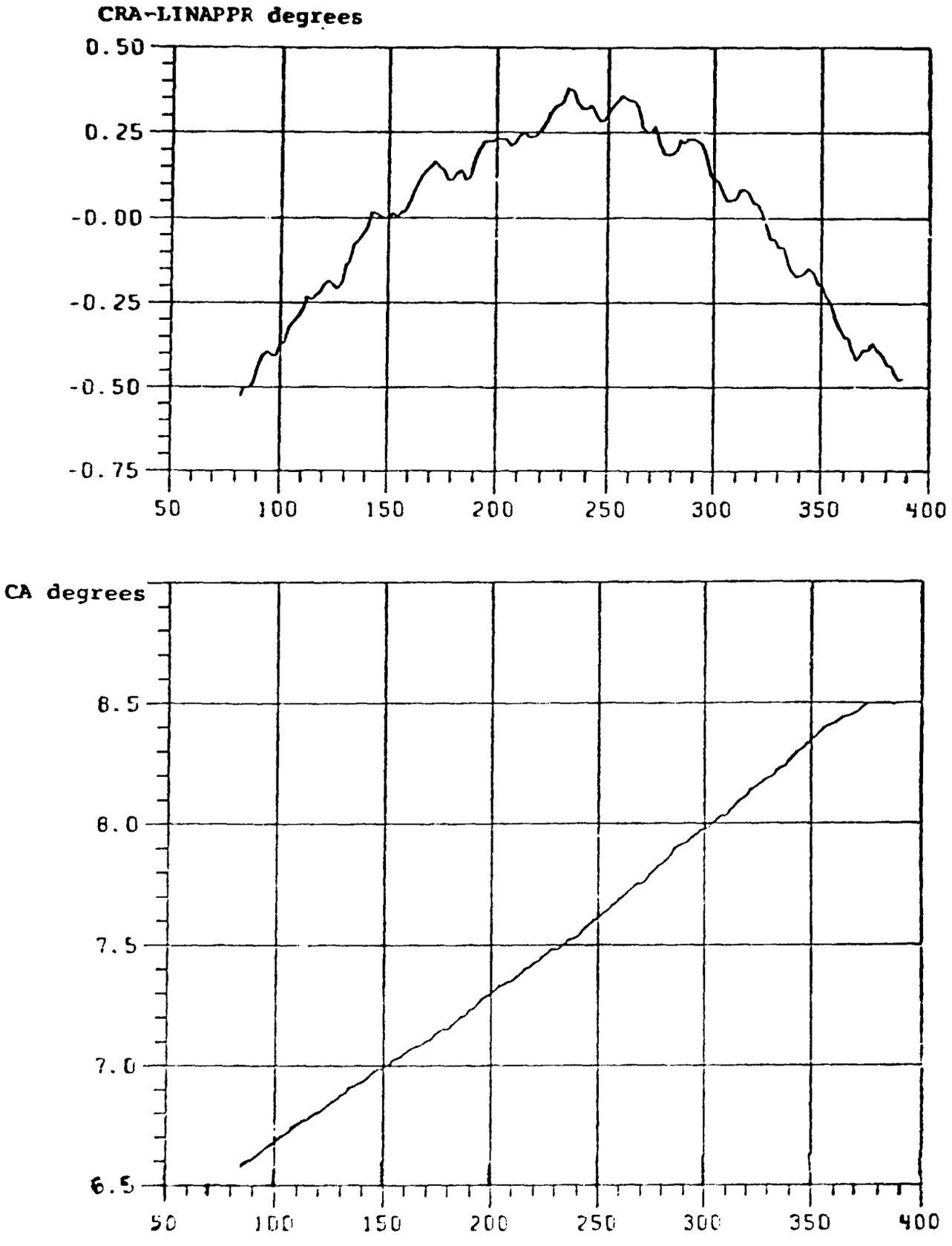

Figure 1.8. Calculated attitude angles for S17-1 (mother payload) based on star sensor data (courtesy of B. Schmidtbauer, 1977).

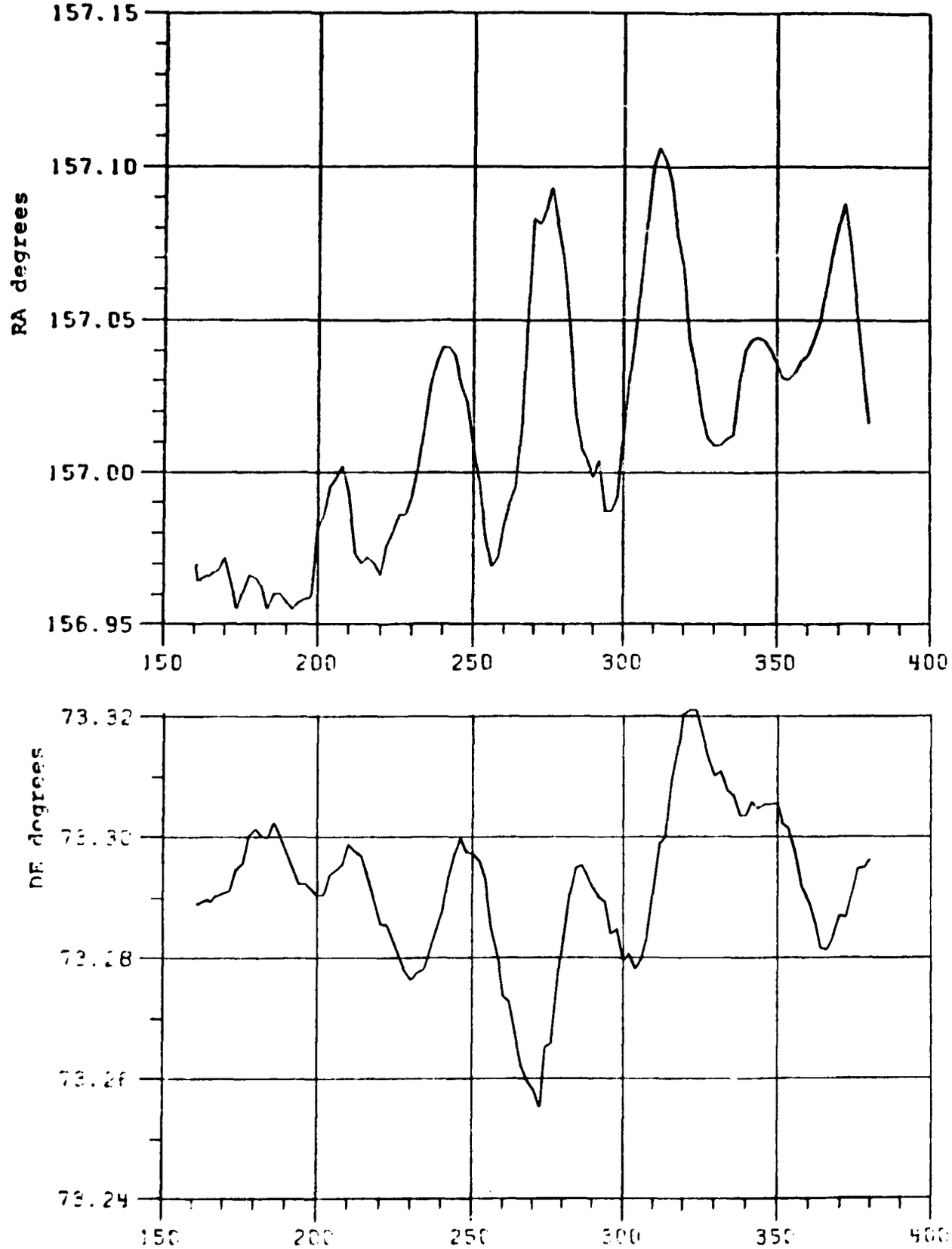

Figure 1.9. Calculated attitude angles for S17-2 (mother payload) based on star sensor data (courtesy B. Schmidtbauer, 1977).

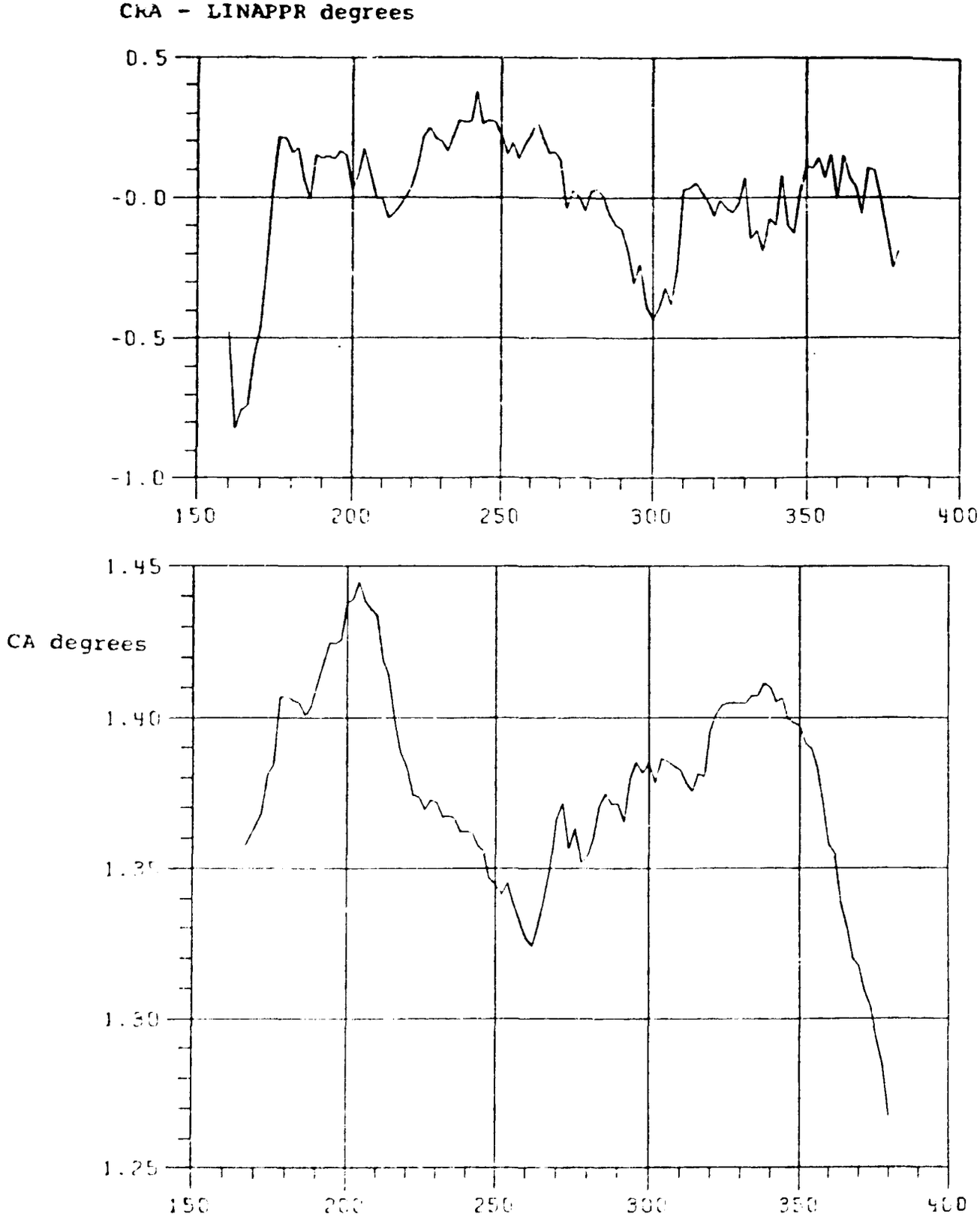

Figure 1.10. Caluclated attitude angles for S17-2 (mother payload) based on star sensor data (courtesy of B. Schmidbauer, 1977).

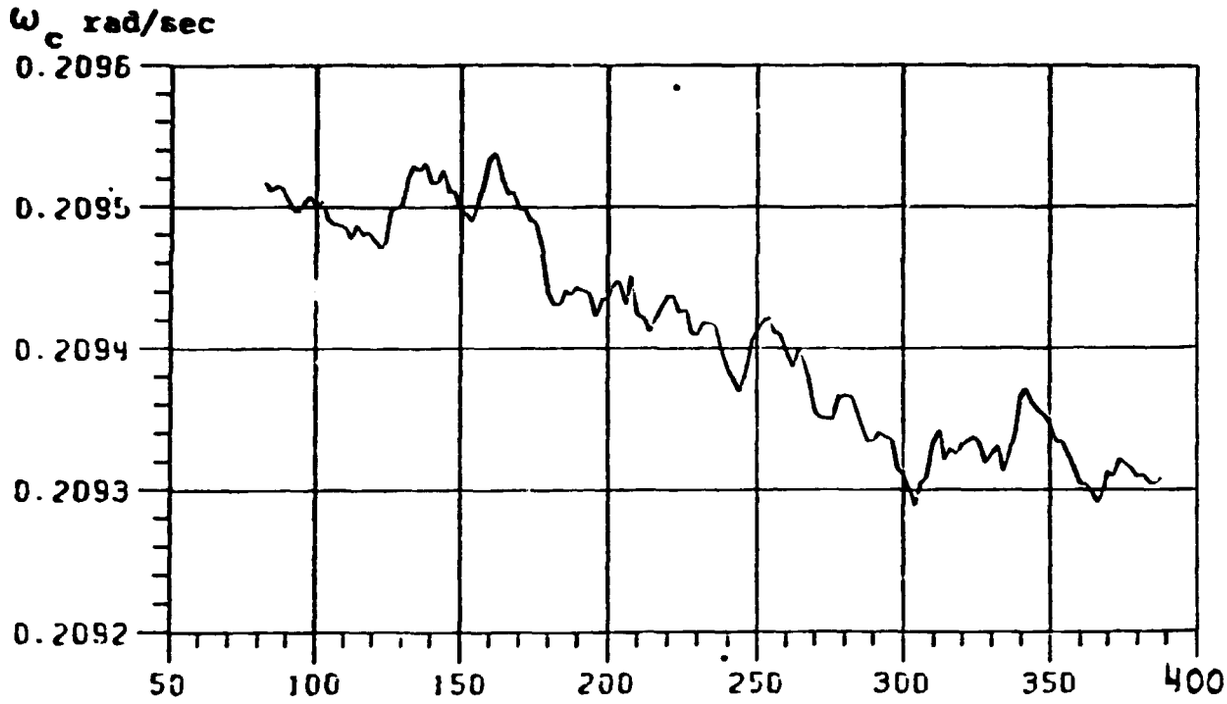

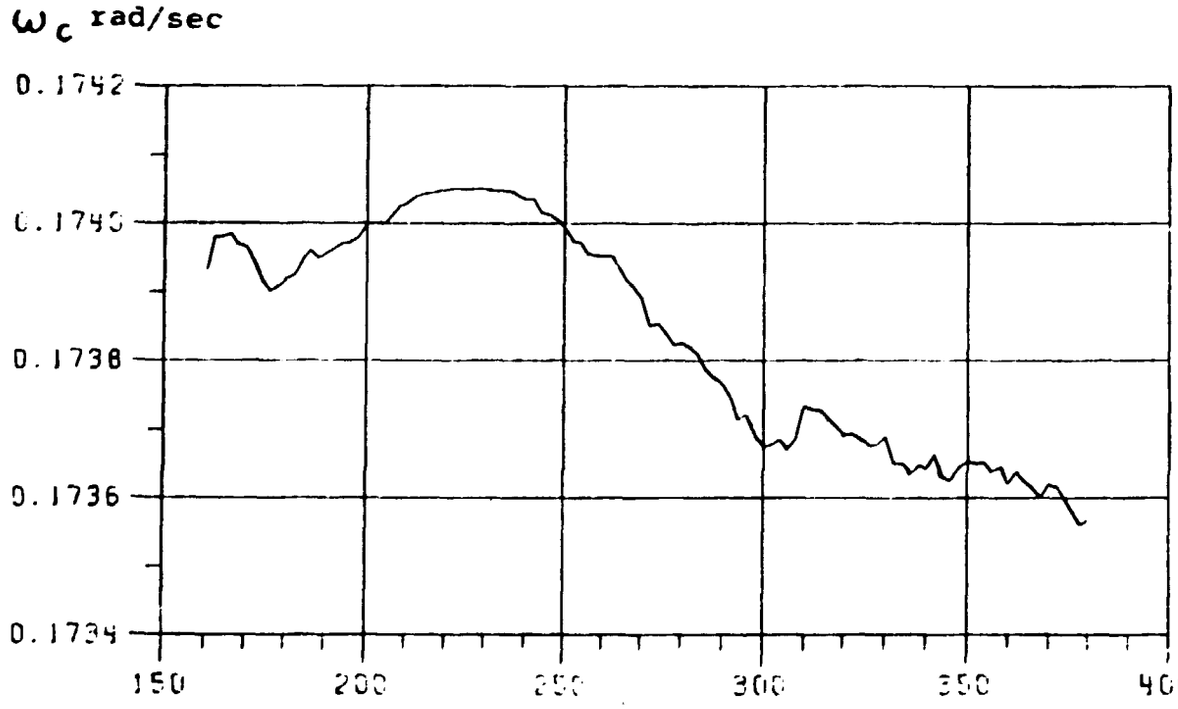

Figure 1.11. The coning rate of S17-1 and S17-2 (mother payloads) and the angular velocities calculated from the star sensor data (courtesy of B. Schmidtbauer, 1977).

S17-2 (mother) payload:

RA = 2.7404 (= 157.01 degrees)

DE = 1.2792 (= 73.29 degrees)

CRA = -3.7595 + 0.173298 (t-300)

CA = 0.0240 (= 1.38 degrees)

BRA = -227.068 + 20.139306 (t-300) - $2.807 \cdot 10^{5}$ $(t-300)^2$ + $3.28 \cdot 10^{-8}$ $(t-300)^3$.

In order to calculate the angle between the rocket spin axis and the earths magnetic field and thus obtain the pitch angle distribution of the detected precipitating particles a magnetometer onboard the S17 payloads measured the components of the magnetic field vector.

If (according to Figure 1.12)

B is the total magnetic field vector
B_x, B_y are the "horizontal, roll" components
B_z is the "vertical", pitch" component and
α is the angle between rocket spin axis and the earths magnetic field

we have

$$|B| = \sqrt{B_z^2 + B_{x\,max}^2}$$

where

$$B_{x\,max} = \sqrt{B_x^2 + B_y^2}$$

$$\cos \alpha = B_z / B.$$

If the viewing direction of the detectors is given in coordinates of the magnetometer frame of reference with the coordinates D_x, D_y, and D_z we will have for the angle v between the detector and the magnetic field vecor (= pitch angle) the following expression:

$$v = \arccos \frac{\underline{D}_x \cdot \underline{B}_x + \underline{D}_y \cdot \underline{B}_y + \underline{D}_y \cdot \underline{B}_y}{|\underline{D}| \cdot |\underline{B}|}$$

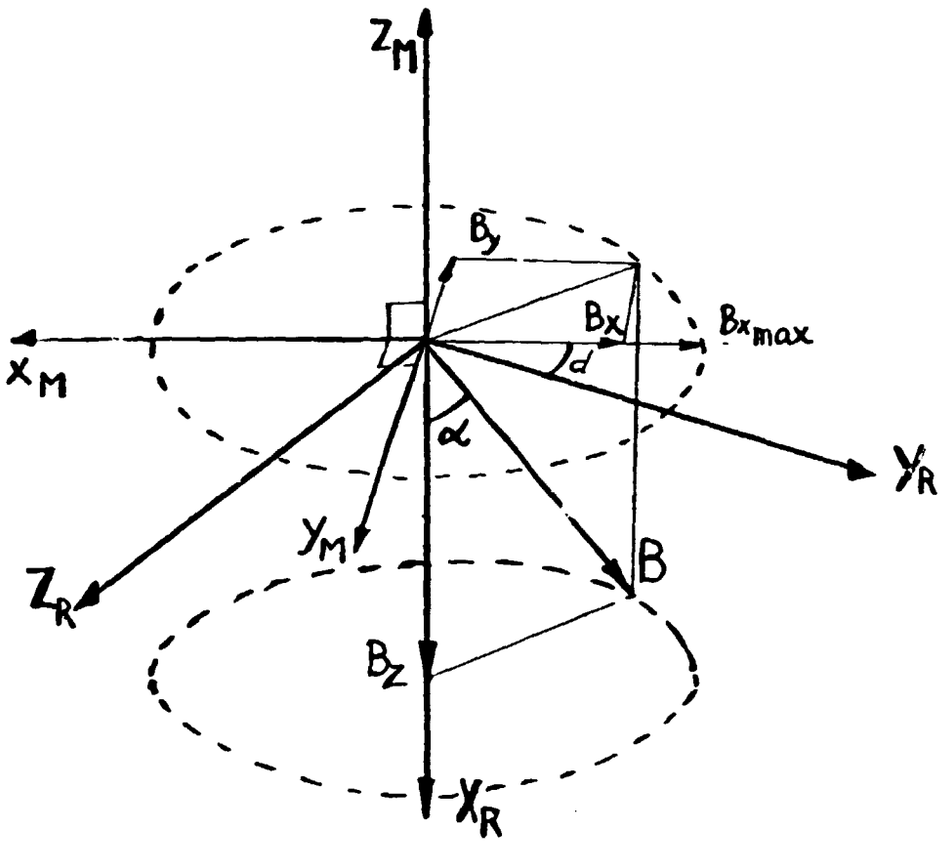

X_K Y_R Z_R coordinate system of the rocket
x_M y_M z_M coordinate system of the magnetometer

Deviation d (degrees) of the two coordinate systems:

S17 1, 2	Mother	0°
S17 1	Daughter	23.6°
S17 2	Daughter	34.0°

Figure 1.12. Magnetic field components in magnetometer frame of reference and S17 rocket body frame of reference.

The magnetic field components B_x and B_y were recorded every 0.010 s (mother payload) respectively every 0.008 s (daughter payload). In Table 1.1 pointing direction and coordinates in the magnetometer frame of reference of all the detectors in S17 payloads are presented.

1.7 Separation of the two payload units

The longitudinal separation mechanism consisted of four springs mounted in the daughter payload. The springs were designed for a nominal longitudinal separation speed of 1.5 m/s.

To get a lateral separation of the daughter payload a small rocket motor was used. In order to have a well defined direction in spite of the spin the burn time of the rocket was very short (≈20 ms). The S17 rockets were designed to give the

Payload	Type of detector	Viewing direction degrees	Coordinates in magnetometer frame of reference		
			X_m	Y_m	Z_m
Mother	CEM	0	0	0	1
	CEM	25	sin 25°	0	cos 25°
	CEM	80	cos 10°	0	cos 80°
	CEM	150	0.5	0	$-\sqrt{3}/2$
	SSD	25	-sin 25°	0	cos 25°
	SSD	80	-cos 10°	0	sin 10°
Daughter	CEM	30	0.5 cos d	-0.5 sin d	$\sqrt{3}/2$
	SSD	30	-0.5 cos d	0.5 sin d	$\sqrt{3}/2$

Table 1.1. Pointing directions (relative the rocket spin axis) of the S17 detectors and their coordinates in the magnetometer frame of reference.

daughter a nominal lateral separation speed of 5 m/s. The lateral separation rocket motor was ignited from a special unit in the daughter at a time after the daughter had separated longitudinally from the mother. Post flight trajectories for all the S17 - payloads, the velocities of the daughter relative to the mother payload and the azimut angles are obtained from calculation based on data from both the star sensor and the doppler radar.

Time for separation	S17 1	S17 2
Longitudinal (s)	51.9	49.6
Lateral (s)	57.2	56.9
Vertical velocity (m/s)	1.2	1.1
Horizontal velocity (m/s)	4.8	4.8

In calculation of the trajectories the following general expressions have been used:

$$x = x_p + \dot{x}(t - t_p)$$

$$y = y_p + \dot{y}(t - t_p)$$

$$z = z_p - 1/2(g_0 - g_1 z_p + g_2 z_p^2)(t-t_p)^2 \cdot (1+1/12(g_1 - 2g_2 z_p)(t-t_p)^2)$$

In these expressions

x = north (m) y = east (m)

z = up (m) t = time (s) given in relative time

lift off for S17 1: 185836 UT for S17 2: 210016 UT

x_p, y_p, z_p, t_p are the coordinate values at the apogee of the rocket

$\dot{x}$ = velocity northward (m/s) $g_0 = 9.82498\ (ms^{-2})$

$\dot{y}$ = velocity eastward (m/s) $g_1 = .3086 \cdot 10^{-5}\ (s^{-2})$

$g_2 = 7.2 \cdot 10^{-13}\ (m^{-1}s^{-2})$.

The following constants for the trajectory were used (for daughter payloads after the lateral separation).

	S17-1		S17-2	
	Mother	Daughter	Mother	Daughter
t_p	230.2	230.34	227.4	227.53
x_p	36800	37480	29000	29590
y_p	-16400	-16860	-8300	-7750
z_p	211100	211323	203400	203606
$\dot{x}$	165.1	169.1	138.4	141.9
$\dot{y}$	-73.5	-76.2	-39.7	-36.4

(A. Söderberg SRB, 1978)

The payloads were equipped with two tone ranging receivers for measuring the distance from the ground to the payload. For measurement of the distance between the daughter and the mother after daughter separation a radar unit was mounted on the top of the mother payload. This unit was started after separation. Figure 1.17 is a graphical representation of the distance between mother and daughter payloads. The lower line represents S17-1 and the upper one S17-2.

The geographic coordinates λ (east longitude) and ϕ (latitude) of different rocket positions along the trajectory and the magnetic field components in these positions were calculated for the S17 payloads.

The rocket trajectories are well described by parabolas and the horizontal distance (S) from the trajectory point to the launch pad and the height (H) above launch pad are given in the radar obtained trajectory coordinates in Tables 1.7 and 1.8.

The geographic coordinates used for the Esrange launch pad are

$\lambda_{Esr} = 21.11^{\circ}$
$\phi_{Esr} = 67.89^{\circ}$
$H_{Esr} = 0.3$ km

and the longitude λ_p and latitude ϕ_p of the rocket position are obtained by MacLaurin expansions:

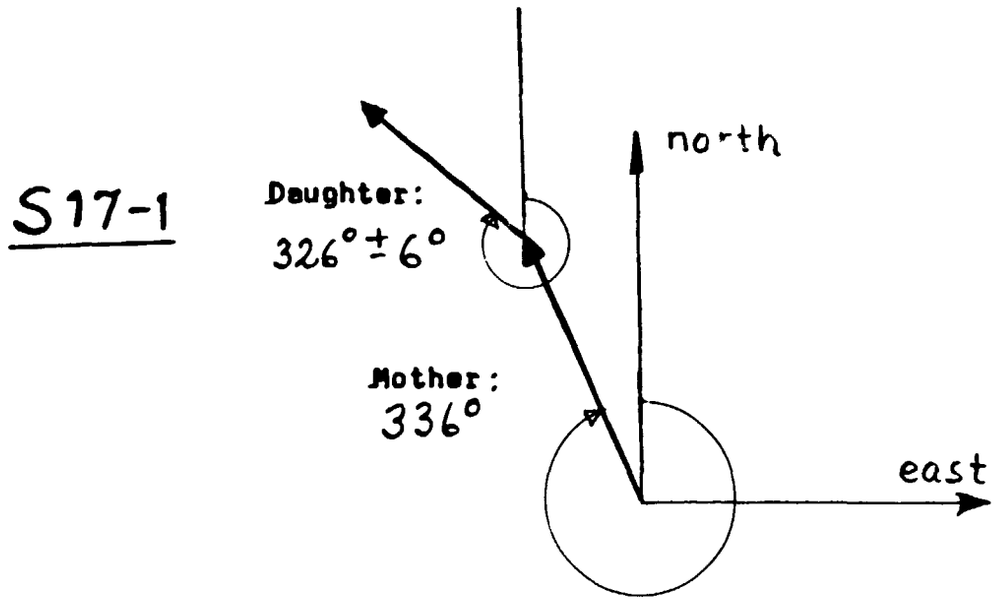

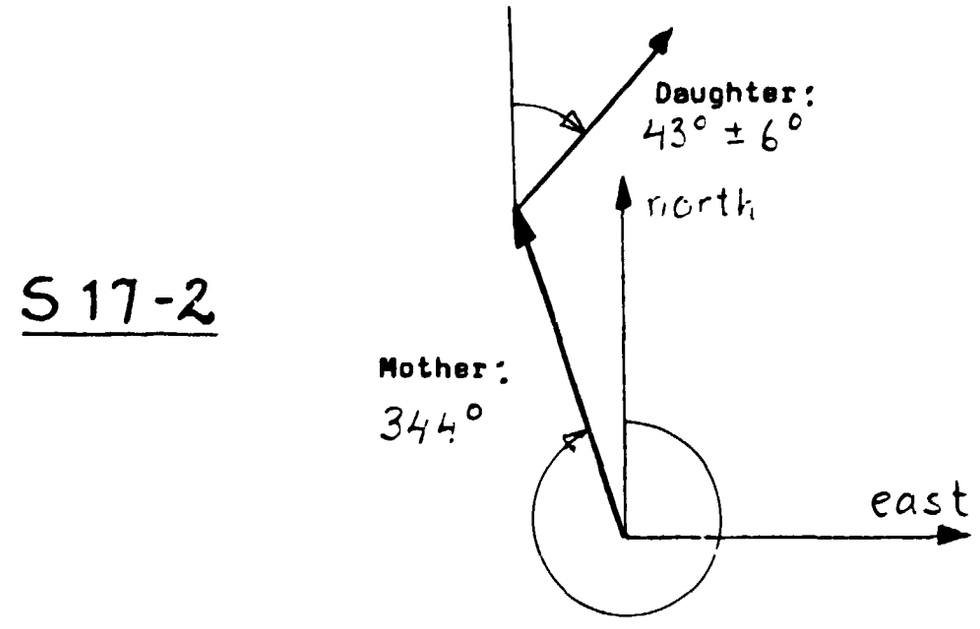

Table 1.2 Azimuth angles for the S17 payloads.

	Mother			Daughter		
T	X	Y	Z	X	Y	Z
40.0	5398	-2420	43192	5398	-2420	43192
50.0	7049	-3155	60512	7049	-3155	60512
60.0	8700	-3890	76870	8676	-3880	76880
70.0	10351	-4625	92271	10367	-4642	92293
80.0	12002	-5360	106717	12058	-5404	106752
90.0	13653	-6095	120215	13749	-6166	120262
100.0	15304	-6830	132766	15440	-6928	132826
110.0	16955	-7565	144376	17131	-7690	144447
120.0	18606	-8300	155046	18822	-8452	155130
130.0	20257	-9035	164780	20513	-9214	164876
140.0	21908	-9770	173581	22204	-9976	173690
150.0	23559	-10505	181450	23895	-10738	181572
160.0	25210	-11240	188391	25586	-11500	188525
170.0	26861	-11975	194405	27277	-12262	194552
180.0	28512	-12710	199494	28968	-13024	199653
190.0	30163	-13445	203659	30659	-13786	203830
200.0	31814	-14180	206901	32350	-14548	207085
210.0	33465	-14915	209222	34041	-15310	209419
220.0	35116	-15650	210621	35732	-16072	210831
230.0	36767	-16385	211100	37423	-16834	211322
240.0	38418	-17120	210658	39114	-17596	210894
250.0	40069	-17855	209295	40805	-18358	209544
260.0	41720	-18590	207012	42496	-19120	207273
270.0	43371	-19325	203806	44187	-19882	204081
280.0	45022	-20060	199678	45878	-20644	199966
290.0	46673	-20795	194627	47569	-21406	194928
300.0	48324	-21530	188650	49260	-22168	188964
310.0	49975	-22265	181746	50951	-22930	182074
320.0	51626	-23000	173913	52642	-23692	174255
330.0	53277	-23735	165150	54333	-24454	165505
340.0	54928	-24470	155453	56024	-25216	155822
350.0	56579	-25205	144821	57715	-25978	145203
360.0	58230	-25940	133249	59406	-26740	133646
370.0	59881	-26675	120735	61097	-27502	121146
380.0	61532	-27410	107276	62788	-28264	107701
390.0	63183	-28145	92867	64479	-29026	93306
400.0	64834	-28880	77505	66170	-29788	77958
410.0	66485	-29615	61185	67861	-30550	61653
420.0	68136	-30350	43904	69552	-31312	44387

Table 1.3 Trajectory coordinates for S17-1 payloads.

	Mother			Daughter		
T	X	Y	Z	X	Y	Z
40.0	3064	-860	40054	3064	-860	40054
50.0	4448	-1257	57145	4448	-1257	57145
60.0	5832	-1654	73273	5817	-1652	73263
70.0	7216	-2051	88442	7236	-2016	88464
80.0	8600	-2448	102656	8655	-2380	102690
90.0	9984	-2845	115919	10074	-2744	115965
100.0	11368	-3242	128236	11493	-3108	128293
110.0	12752	-3639	139609	12912	-3472	139677
120.0	14136	-4036	150041	14331	-3836	150121
130.0	15520	-4433	159536	15750	-4200	159627
140.0	16904	-4830	168096	17169	-4564	168199
150.0	18288	-5227	175723	18588	-4928	175837
160.0	19672	-5624	182420	20007	-5292	182546
170.0	21056	-6021	188186	21426	-5656	188326
180.0	22440	-6418	193029	22845	-6020	193179
190.0	23824	-6815	196945	24264	-6384	197106
200.0	25208	-7212	199936	25683	-6748	200109
210.0	26592	-7609	202003	27102	-7112	202188
220.0	27976	-8006	203147	28521	-7476	203344
230.0	29360	-8403	203369	29940	-7840	203578
240.0	30744	-8800	202668	31359	-8204	202889
250.0	32128	-9197	201043	32778	-8568	201276
260.0	33512	-9594	198496	34197	-8932	198741
270.0	34896	-9991	195024	35616	-9296	195282
280.0	36280	-10388	190627	37035	-9660	190897
290.0	37664	-10785	185304	38454	-10024	185586
300.0	39048	-11182	179053	39873	-10388	179348
310.0	40432	-11579	171873	41292	-10752	172180
320.0	41816	-11976	163761	42711	-11116	164081
330.0	43200	-12373	154715	44130	-11480	155048
340.0	44584	-12770	144733	45549	-11844	145079
350.0	45968	-13167	133812	46968	-12208	134171
360.0	47352	-13564	121949	48387	-12572	122321
370.0	48736	-13961	109141	49806	-12936	109525
380.0	50120	-14358	95383	51225	-13300	95781
390.0	51504	-14755	80673	52644	-13664	81084
400.0	52888	-15152	65006	54063	-14028	65431
410.0	54272	-15549	48378	55482	-14392	48816
420.0	55656	-15946	30784	56901	-14756	31236

Table 1.4 Trajectory coordinates for S17-2 payloads.

S17-1

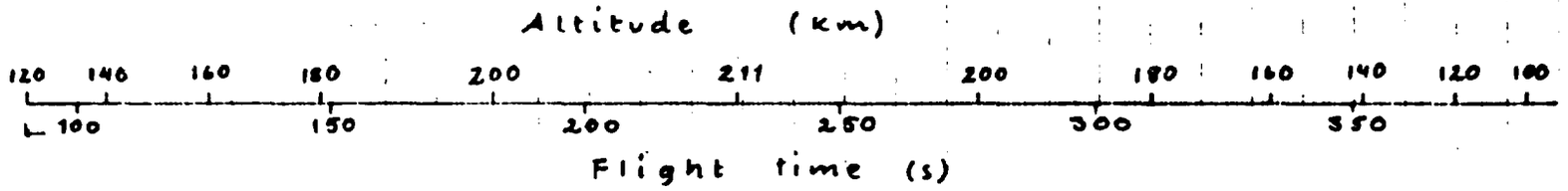

S17-2.

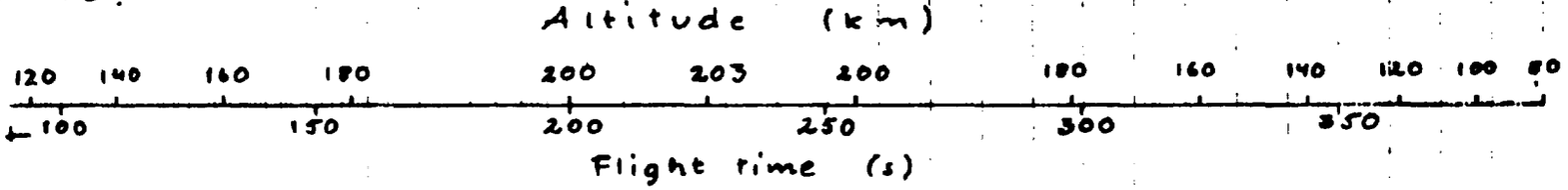

Table 1.5 Altitude versus flight time for S17 payloads.

Payload	Average angle to the earth magnetic field	Half the coning angle	Coning frequency	Coning time	Spinrate	Spintime
	α	CA	f_C	T_C	f_S	T_s
	(degrees)	(degrees)	periods/s	s	rounds/s	s
S 17 1-M	18.5	6.4 - 8.5	0.033	30.3	3.4	0.29
S 17 1-D	15.4	2.4	0.72	1.4	4.1	0.24
S 17 2-M	20.0	1.5	0.027	37.1	3.2	0.31
S 17 2-D	16.0	6.5	0.61	1.7	3.5	0.29

Table 1.6 Angles from the geomagnetic field lines, coning and spin rates for the S17 payloads during the measurement part of the flight.

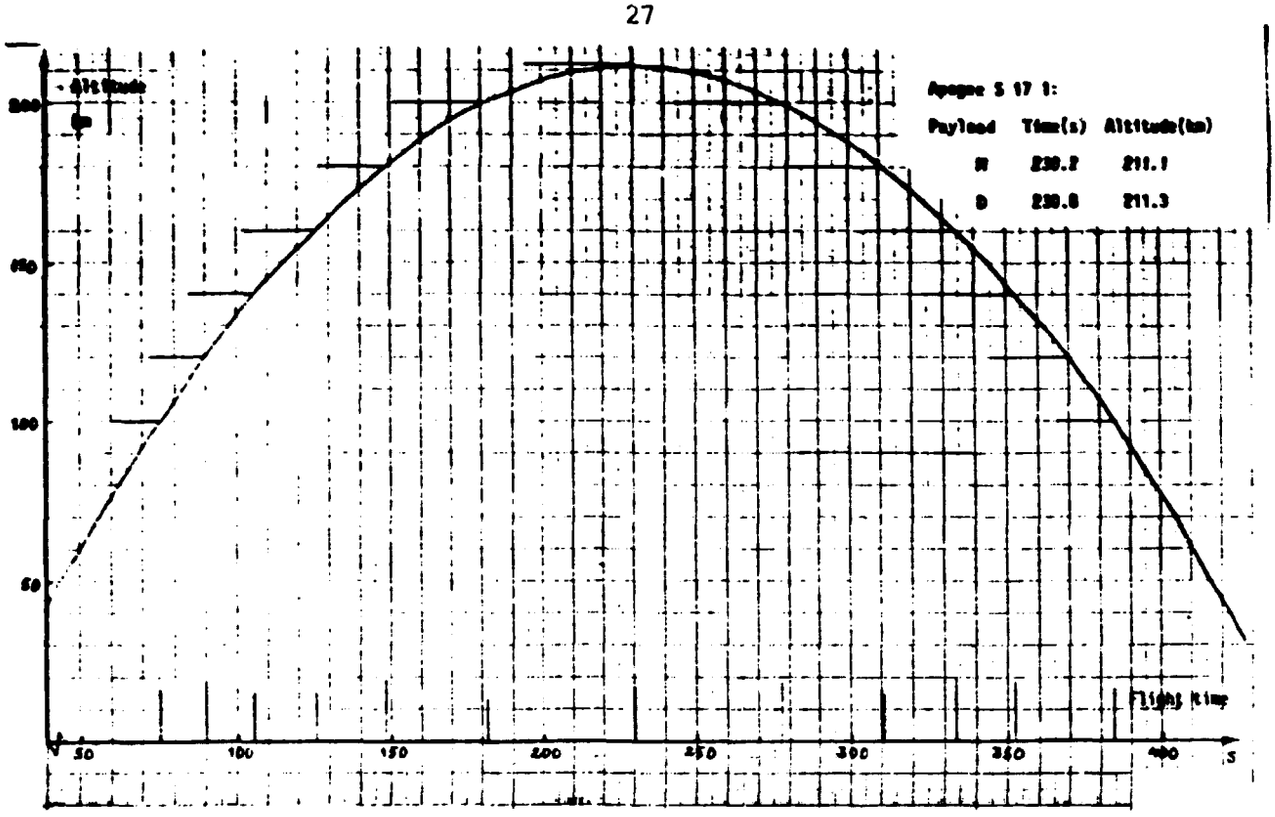

Figure 1.13 Altitude versus flight time for S17-1 payloads.

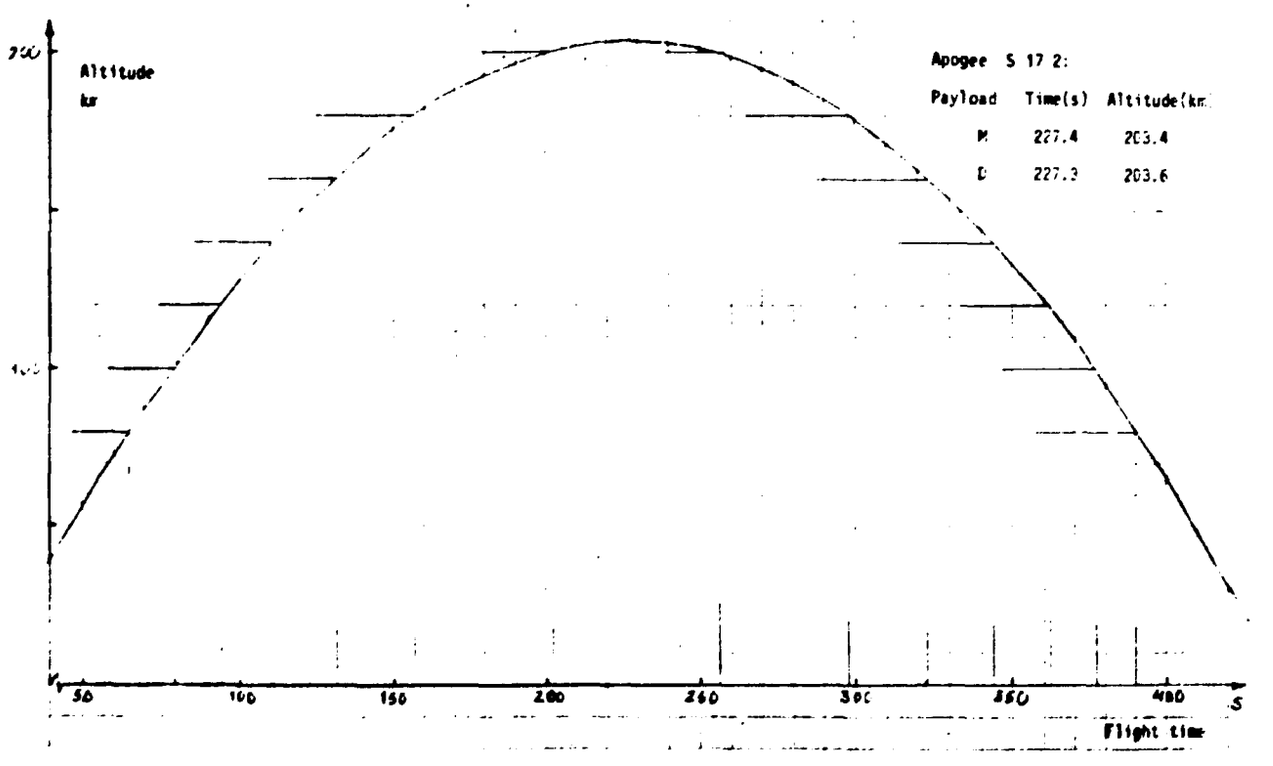

Figure 1.14 Altitude versus flight time for S17-2 payloads.

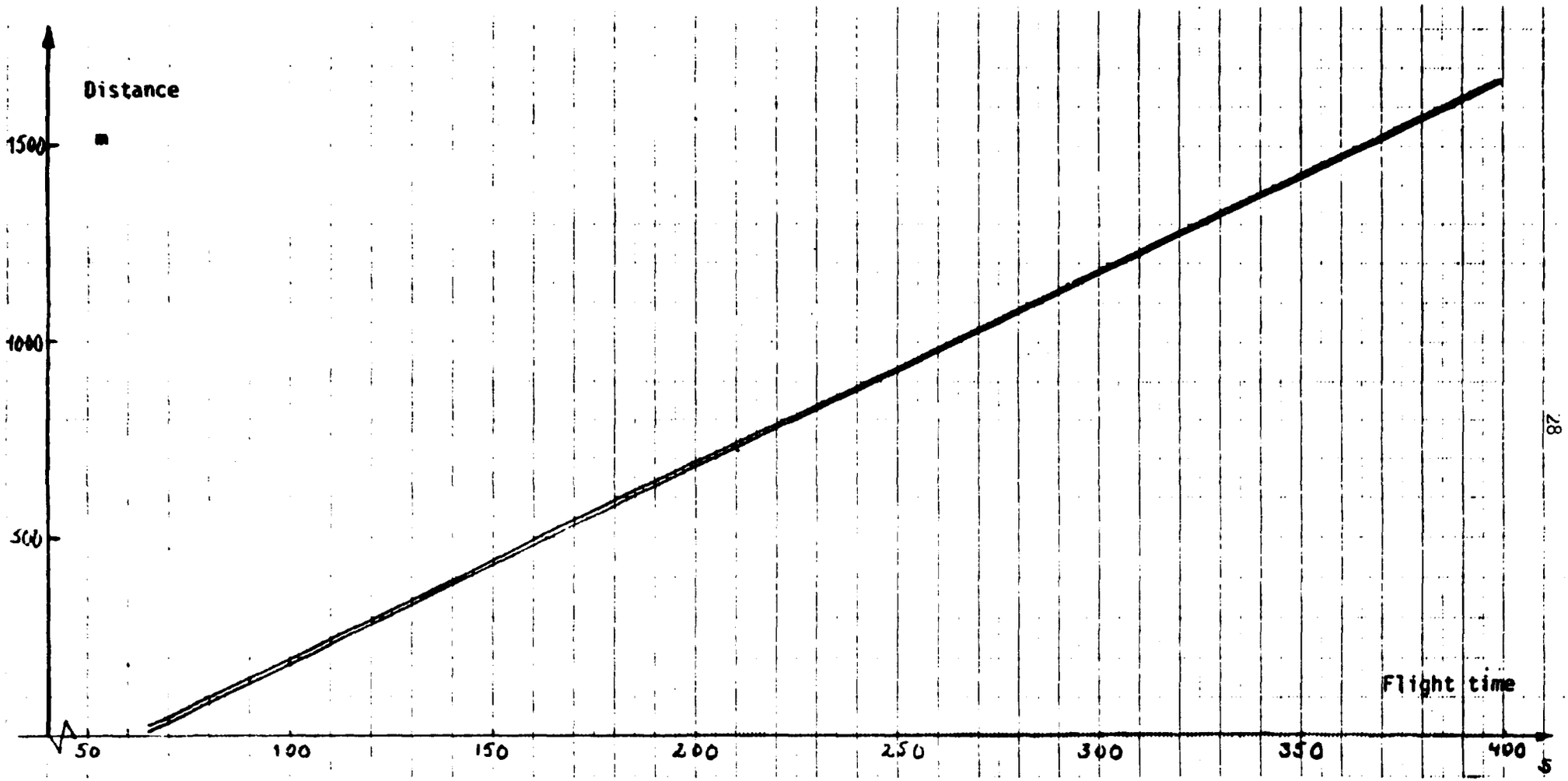

Figure 1.15 The distance between mother and daughter payloads. (Upper line: S17-2, lower line: S17-1).

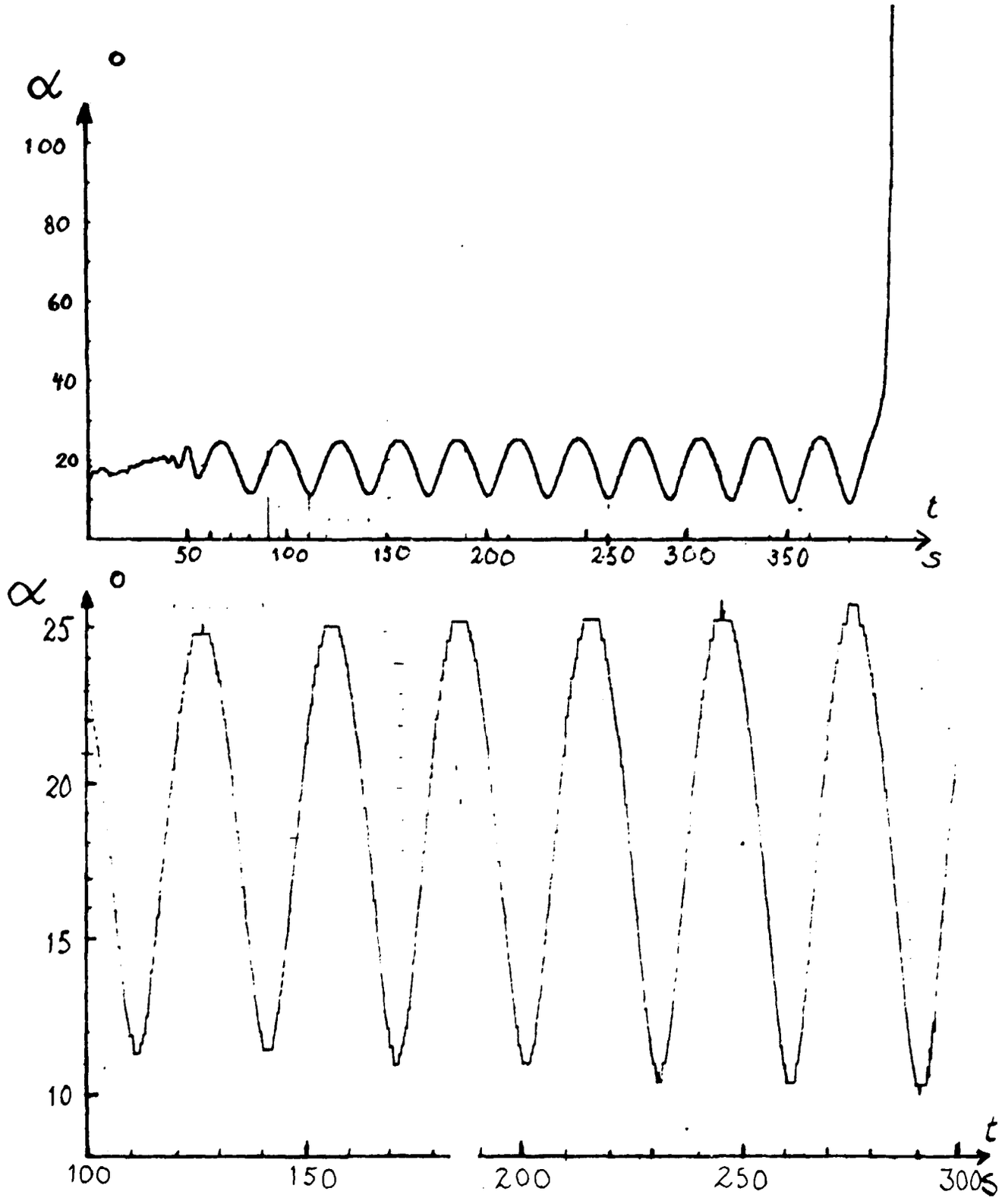

Figure 1.16 Flight-time history of the angle α between the earth's magnetic field and the main axis of the payload S17-1 mother.

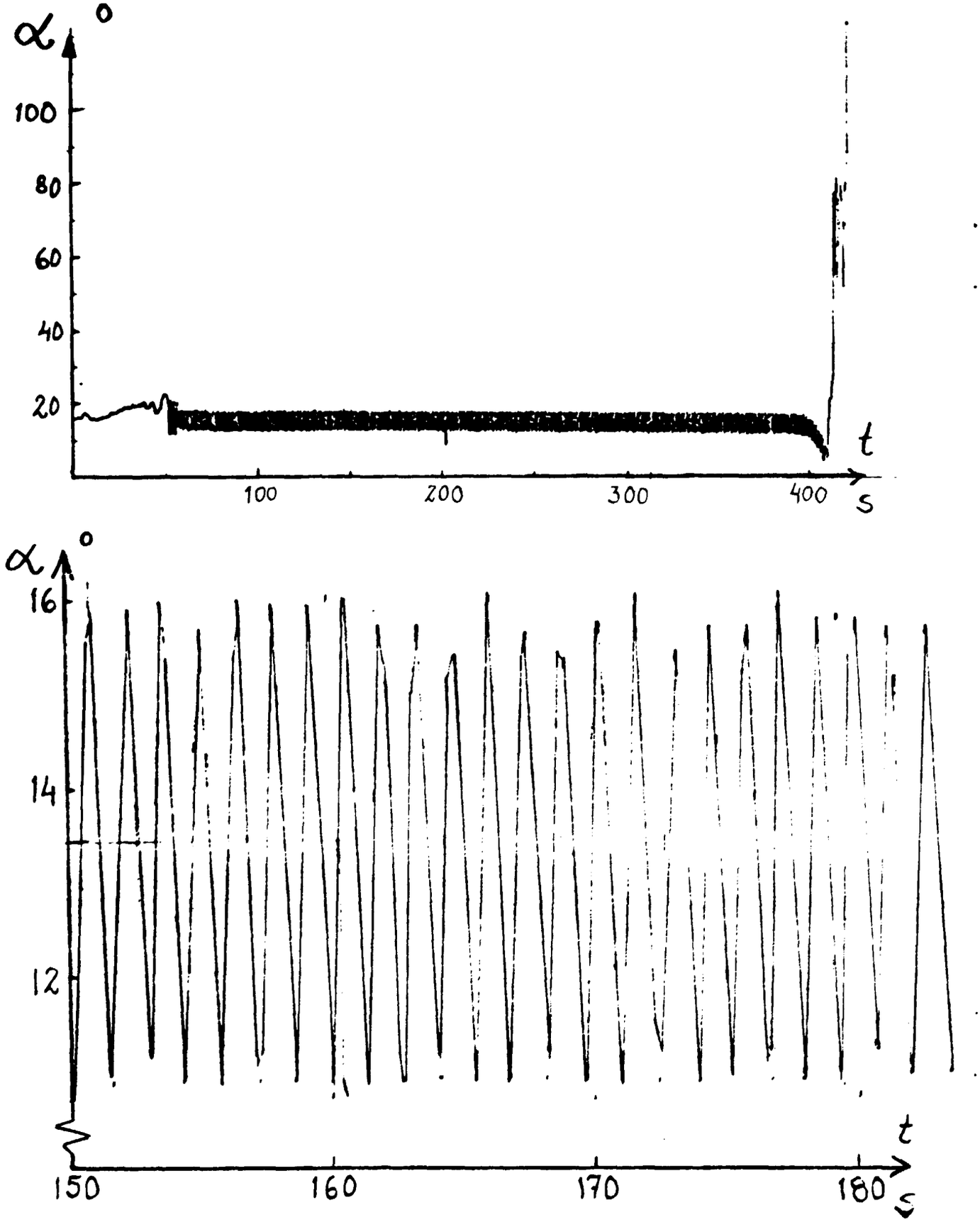

Figure 1.17 Flight-time history of the angle α between the earth's magnetic field and the main axis of the payload S17-1 Daughter.

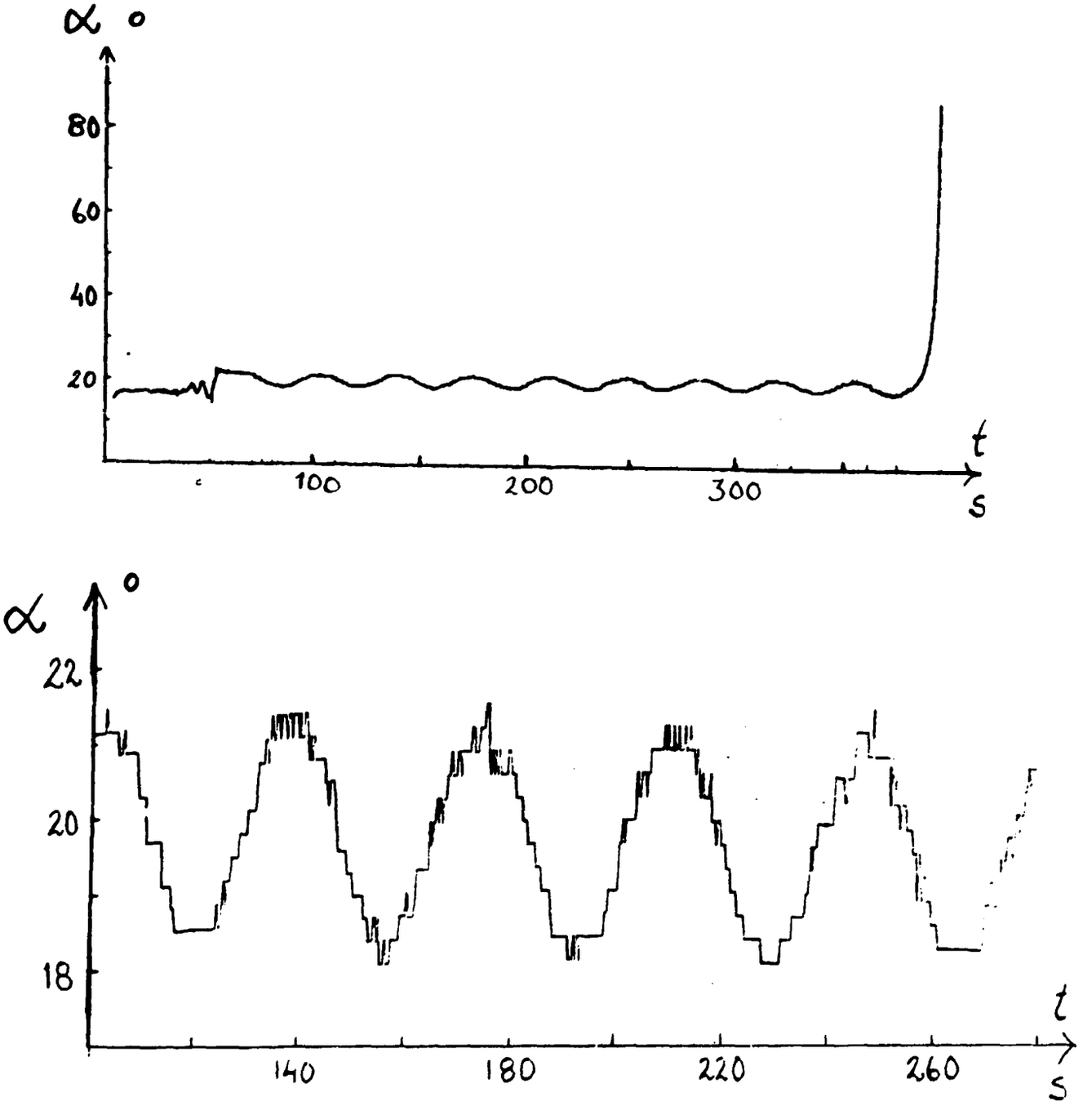

Figure 1.18 Flight-time history of the angle α between the earth's magnetic field and the main axis of the payload S17-2 mother.

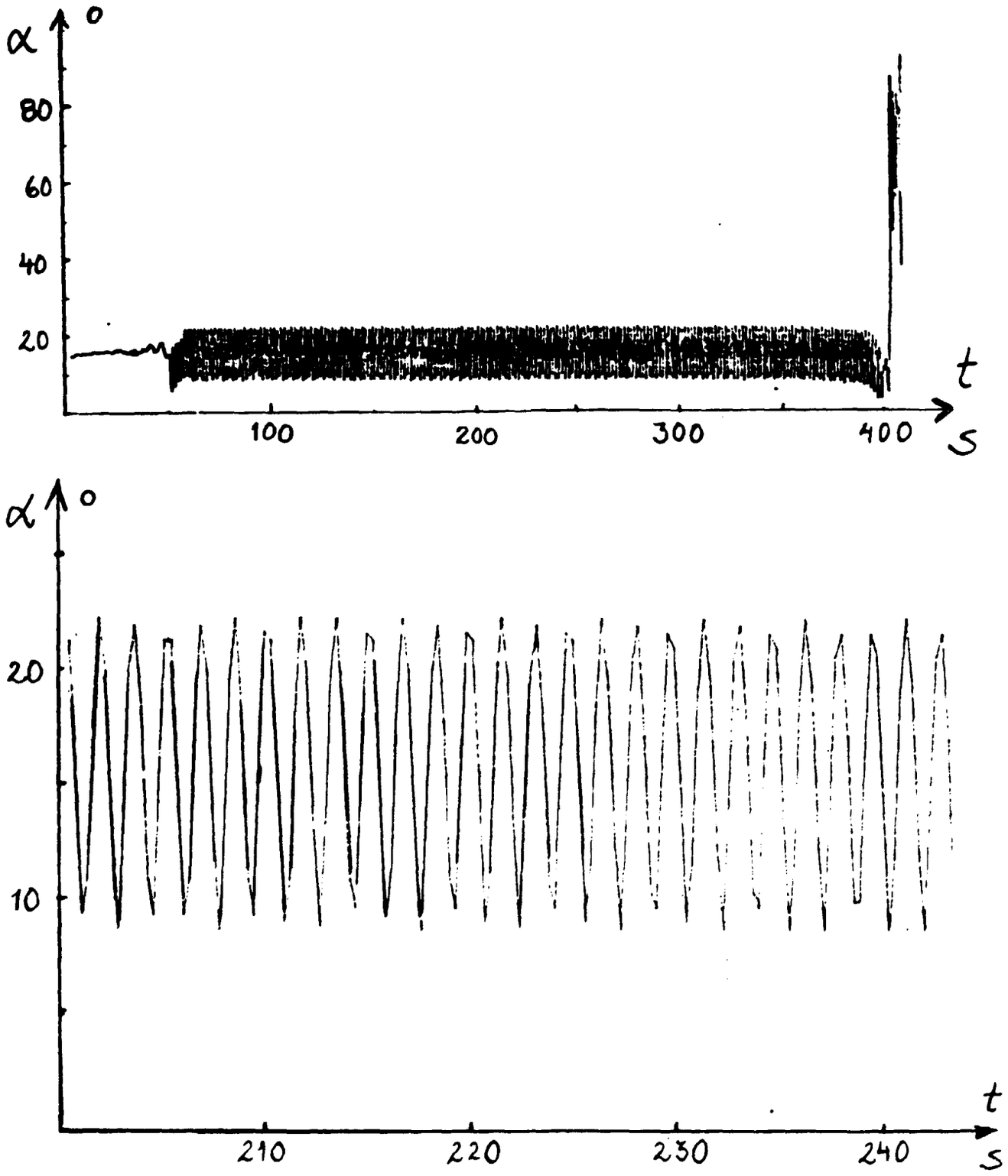

Figure 1.19 Flight-time history of the angle α between the earth's magnetic field and the main axis of the payload S17-2 daughter.

$$\lambda_p = \lambda_{Esr} + C_1 S + C_2 \cdot S^2$$

$$\phi_p = \phi_{Esr} + C_3 S + C_4 \cdot S^2$$

$$H_p = H_{Esr} + H$$

where the constants are

$C_1 = 1.565 \cdot 10^{-4} \cdot \cos \alpha_L \cdot 57.296$ degrees/km

$C_2 = (-1.731 \cdot 10^{-10} \cos^2 \alpha_L - 6.024 \cdot 10^{-8} \sin^2 \alpha_L) \cdot 28.65$ degrees/km^2

$C_3 = 4.155 \cdot 10^{-4} \sin \alpha_L \cdot 57.296$ degrees/km

$C_4 = 1.204 \cdot 10^{-7} \sin \alpha_L \cdot \cos \alpha_L \cdot 28.65$ degrees/km^2

α_L is the azimuth direction for the main axis of the rocket. In Tables 1.7 and 1.8 these calculated trajectory data are presented. The magnetic field model used in the computer program was the International Geophysical Reference Field IGRF 1975.

1.8 Telemetry and data analyzing technique

The recorded information from the experiments in the S17 - payloads was transmitted to the ground based receiver by the rocket borne telemetry-system. This flight data was accumulated and stored on video tapes at Esrange. A conversion was made into computer compatible magnetic tapes. At KGI a further conversion was made of the data and only the data from the S17 experimental actual datachannels was separated out.

From these converted "raw data" tapes the four time words were transformed to rocket flight time, some calculated magnetometer information was added and these final magnetic tapes were used as work copies. (These are marked datfile a, b, c and d respectively). Some format specification are given in Table 1.9.

Timing errors exist in the data from the following periods:

	Flight time (s)
S17-1 M	344.209 - 351.333
S17-2 M	341.281 - 396.473
S17-2 D	325.0

TRAJECTORY DATA FOR ROCKET S 17-1

HEIGHT H KM	RANGE S KM	LATITUDE ϕ_p DEGREES	LONGITUDE λ_p DEGREES	B-NORTH GAMMAS	B-EAST GAMMAS	B-DOWN GAMMAS	B-TOTAL GAMMAS	DIP DEGREES	DECL DEGREES
70.6	10.1	67.97	21.01	11621.	729.	49724.	51069.	76.82	3.59
80.2	11.[illegible]	67.98	21.00	11575.	712.	49530.	50869.	76.82	3.52
90.9	12.4	67.99	20.98	11523.	693.	49315.	50668.	76.83	3.44
101.2	13.6	68.00	20.97	11473.	676.	49109.	50436.	76.83	3.37
111.0	14.8	68.01	20.96	11426.	659.	48914.	50235.	76.83	3.30
120.4	16.0	68.02	20.95	11381.	643.	48728.	50044.	76.83	3.23
130.5	17.4	68.03	20.93	11332.	626.	48530.	49839.	76.84	3.16
141.2	19.0	68.04	20.92	11280.	608.	48321.	49624.	76.84	3.09
151.1	20.6	68.06	20.90	11232.	592.	48129.	49426.	76.85	3.02
161.2	22.3	68.07	20.88	11183.	575.	47934.	49224.	76.85	2.96
170.4	24.0	68.08	20.87	11138.	560.	47757.	49042.	76.86	2.88
180.9	26.3	68.10	20.84	11086.	542.	47558.	48836.	76.86	2.80
190.5	28.7	68.12	20.82	11037.	526.	47377.	48648.	76.87	2.73
200.7	32.0	68.15	20.79	10984.	508.	47187.	48451.	76.88	2.65
205.3	34.0	68.17	20.77	10959.	499.	47102.	48363.	76.89	2.61
210.3	37.7	68.20	20.73	10926.	488.	47013.	48269.	76.90	2.56
211.4	40.3	68.22	20.70	10914.	483.	46997.	48250.	76.91	2.54
210.3	43.1	68.24	20.67	10911.	482.	47023.	48275.	76.93	2.53
205.3	46.8	68.27	20.64	10921.	484.	47126.	48377.	76.94	2.54
200.1	49.1	68.29	20.61	10936.	489.	47230.	48482.	76.95	2.56
190.4	52.4	68.31	20.58	10968.	498.	47422.	48677.	76.97	2.60
180.7	54.9	68.33	20.55	11002.	509.	47615.	48872.	76.98	2.65
170.2	57.3	68.35	20.53	11040.	521.	47823.	49083.	76.99	2.70
160.0	59.3	68.37	20.51	11078.	533.	48026.	49290.	77.00	2.75
150.8	61.0	68.38	20.49	11113.	544.	48209.	49477.	77.00	2.80
140.9	62.7	68.40	20.47	11151.	556.	48408.	49678.	77.01	2.86
130.2	64.6	68.41	20.46	11192.	570.	48623.	49897.	77.02	2.92
110.7	67.2	68.43	20.43	11269.	596.	49017.	50299.	77.04	3.03
100.8	68.6	68.45	20.41	11309.	609.	49218.	50504.	77.04	3.08
90.5	69.9	68.44	20.40	11350.	623.	49429.	50719.	77.05	3.14
81.3	71.1	68.47	20.39	11388.	636.	49618.	50912.	77.05	3.20

Table 1.7 Trajectory data for rocket S17-1.

TRAJECTORY DATA FOR ROCKET S 17-2

HEIGHT H	RANGE S	LATITUDE ϕ_p	LONGITUDE λ_p	B-NORTH	B-EAST	B-DOWN	B-TOTAL	DIP	DECL
KM	KM	DEGREES	DEGREES	GAMMAS	GAMMAS	GAMMAS	GAMMAS	DEGREES	DEGREES
69.3	6.7	67.95	21.07	11636.	738.	49746.	51094.	76.81	3.63
79.3	7.6	67.96	21.06	11588.	721.	49544.	50886.	76.81	3.56
89.2	8.5	67.96	21.05	11540.	704.	49345.	50682.	76.81	3.49
100.6	9.6	67.97	21.05	11486.	686.	49117.	50447.	76.82	3.42
110.1	10.6	67.98	21.04	11440.	670.	48928.	50252.	76.82	3.35
120.6	11.7	67.99	21.03	11391.	653.	48725.	50043.	76.82	3.28
130.1	12.8	68.00	21.03	11344.	637.	48536.	49846.	76.82	3.22
140.3	14.0	68.01	21.02	11296.	621.	48335.	49641.	76.83	3.15
150.7	15.4	68.02	21.01	11246.	604.	48133.	49433.	76.83	3.08
160.1	16.8	68.03	21.00	11200.	590.	47951.	49245.	76.84	3.01
171.0	18.4	68.05	20.99	11147.	572.	47742.	49030.	76.84	2.94
180.4	20.4	68.07	20.98	11101.	557.	47564.	48845.	76.85	2.87
190.2	22.8	68.09	20.96	11051.	542.	47379.	48654.	76.86	2.81
200.3	26.5	68.12	20.93	10996.	525.	47193.	48460.	76.87	2.73
203.7	30.2	68.15	20.91	10970.	517.	47136.	48399.	76.89	2.70
200.3	34.0	68.18	20.88	10972.	519.	47210.	48471.	76.90	2.71
190.3	37.9	68.22	20.86	11003.	530.	47411.	48674.	76.92	2.76
180.5	40.3	68.24	20.84	11037.	542.	47606.	48871.	76.93	2.81
170.4	42.3	68.25	20.83	11074.	555.	47806.	49075.	76.94	2.87
160.3	44.1	68.27	20.82	11112.	568.	48007.	49280.	76.95	2.93
150.8	45.5	68.28	20.81	11148.	581.	48197.	49473.	76.96	2.98
140.4	47.0	68.29	20.80	11189.	595.	48405.	49685.	76.97	3.04
130.3	48.6	68.31	20.79	11228.	609.	48609.	49892.	76.97	3.10
120.6	49.6	68.32	20.78	11267.	622.	48804.	50092.	76.98	3.16
110.3	50.8	68.33	20.77	11308.	637.	49013.	50305.	76.99	3.23
100.8	51.8	68.34	20.77	11347.	651.	49206.	50502.	76.99	3.28
90.9	52.9	68.35	20.76	11388.	666.	49409.	50709.	77.00	3.35
80.5	54.0	68.38	20.75	11430.	681.	49622.	50926.	77.01	3.41
71.2	54.9	68.36	20.75	11469.	695.	49814.	51122.	77.01	3.47
61.5	55.9	68.37	20.74	11509.	710.	50015.	51327.	77.02	3.53

Table 1.8 Trajectory data for rocket S17-2.

These errors were pure timing failures and no data gaps exist. However, the swept 0^{o} electron detector in both the mother payloads was disturbed by internal test pulses during the whole flights. These pulsgenerated spikes were eliminated from the final tape copy. One SSD detector in S17-2 daughter payload produced so strong self oscillations that relevant data could not be obtained from this detector.

Typical record format

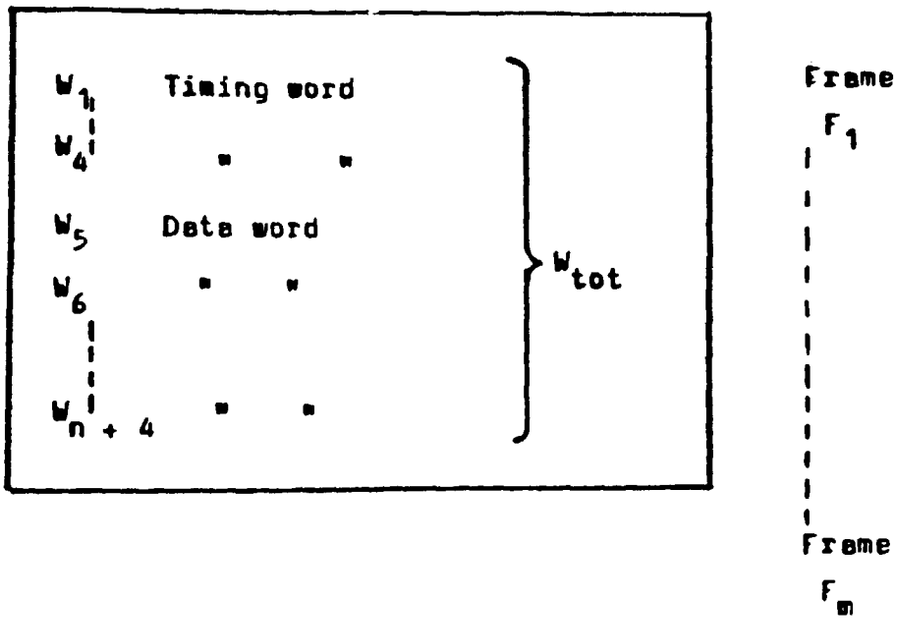

	Mother	Daugther
Wordlength	8 bits	8 bits
Timing words/frame	4	4
Data words/frame (n)	30	30
W_{tot}	34	34
Frames/subframe (m) (format)	32	16
Total number words/subframe (format)	1088	544

Timing word format

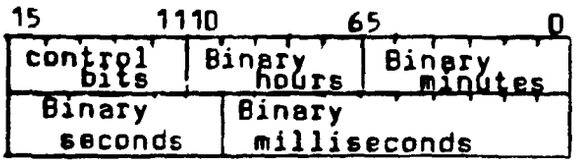

Table 1.9 Some specifications of data formats of the telemetry system for S17 payloads.

2. Description of the instrumentation for the particle experiments in the S17 payloads

2.1 General theory of CEM-detectors

All the particle experiments in the S17 payloads were designed, developed and constructed at Kiruna Geophysical Institute. The instrument set was identical in both the S 17 payloads and included two types of particle detectors. Those for low energy particles had an electrostatic energy analyzer with two cylindrical plates as energy filter and a channel electron multiplier (channeltron, CEM) for measuring the countrate of the particles. The energy range of these detectors was 0.2 - 16 keV for electrons and 0.5 - 8 keV for protons. Particles of higher energies were measured by solid state detectors (SSD-detectors) and were in the S17 experiments used for energies > 40 keV both for electrons and protons.

From $F = m \cdot a = e \cdot U/d$, where F is the force, m the particle mass, U/d the electric field, a the mean acceleration and e the electron charge, follows

$$e \cdot U / d = m \cdot v^2 / r_m \qquad (1)$$

where d is the distance between the parallel plates, U is the potential difference of the plates, v the particles velocity and r_m radius of curvature of the particle trajectory.

The center energy $E_o = m \cdot v^2/2$ for the particle, which is able to pass between the two cylindrical plates of the electrostatic analyzer in Figure 2.1 can thus be written [if $U = V_1 - V_2$ (volts)]:

$$E_o = e \cdot r_m (V_1 - V_2)/2d \quad \text{(in eV)} \qquad (2)$$

Thus, the center energy is determined by the voltage between the analyzer plates, the distance between them and the radius of the particle orbit. Control of the analyzer plate voltage in the S17 instruments was by means of dividing a reference and a monitor voltage in the range of 0 - 5 V. The relation-

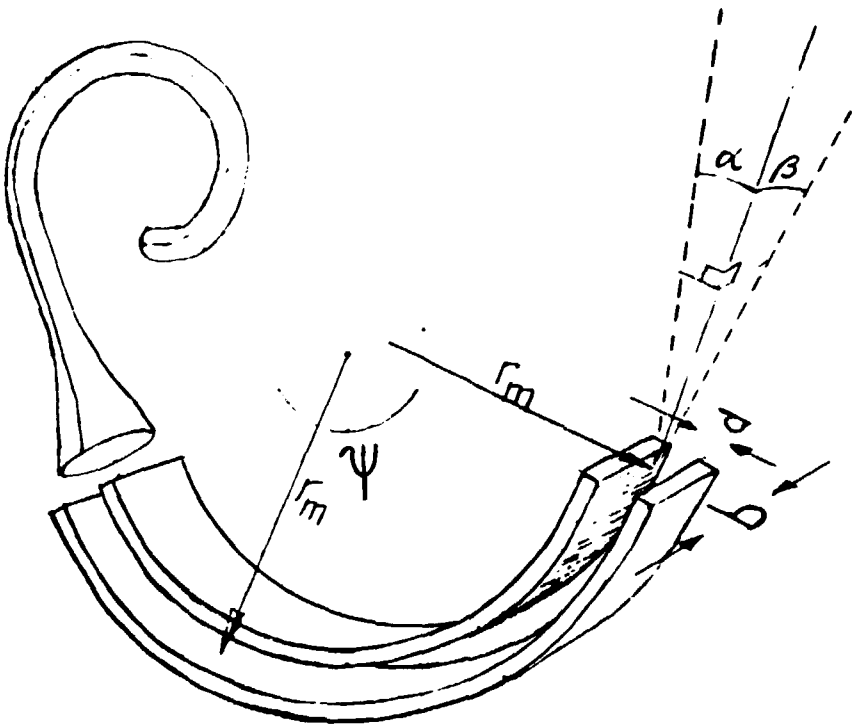

Figure 2.1 Geometry of the detectors with the electrostatic analyzers and the CEM channeltron.

ship between these voltages and the center energy was linear for the actual energies of the S17 - detectors (see Figure 2.2).

The electrostatic analyzer in the S17 experiments contained cylindrical plates with a deflection angle of $\phi = 127.3°$, a mean radius of the particle trajectory of $R_O = 20$ mm and a distance between the plates d = 2-4 mm. This gives a resonably good energy and angular resolution. The energy bandwidth is given by

$\frac{\Delta E}{E_O} = \pm\frac{d}{r_m}$. The maximum acceptance angle is $\alpha_{max} = \pm\sqrt{2}\,\frac{d}{r_m}$

in the plane of the radius of the orbit trajectory between the analyzer plates (see Figure 2.1). Perpendicular to this plane it is

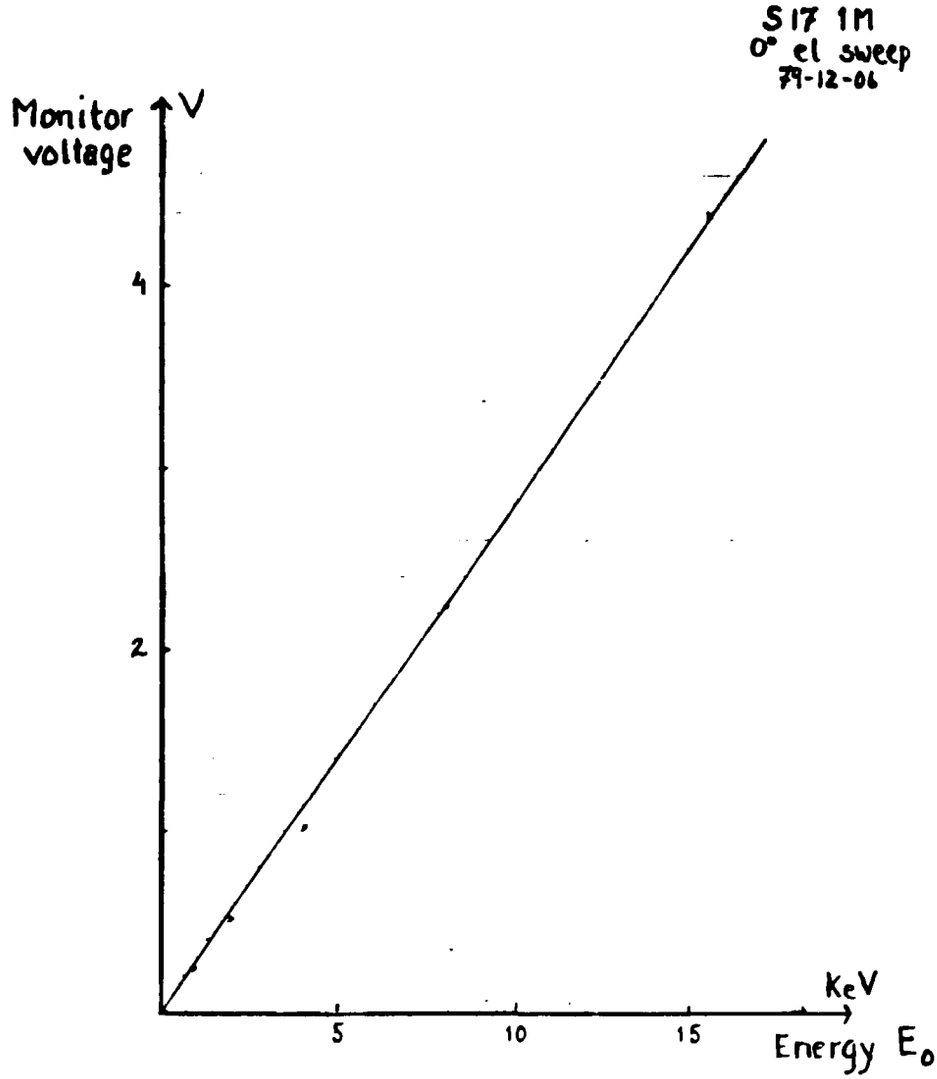

Figure 2.2 S17 calibration. Monitor voltage of the analyzer plates is a linear function of the center energy.

$b_{max} = \pm \frac{\sqrt{2}}{\pi} \cdot \frac{b}{r_m}$, where b is the effective width of the deflection plates (Riedler 1971).

Every particle spectrometer of type electrostatic analyzer has its individual response function of energy for the incoming particles. This energy response of a spectrometer can be represented by a function

$$R(E) = R(E_o) \cdot \exp\left[- \frac{(E-E_o)^2}{(\Delta E)^2} \right] \qquad (3)$$

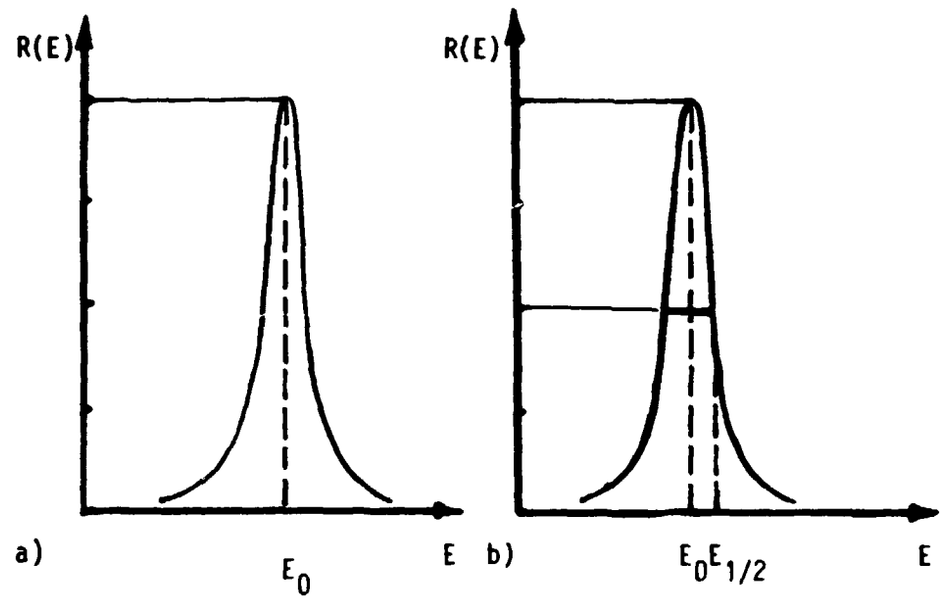

Figure 2.3 a) Energy response for an electrostatic particle detector
b) Full Width Half Maximum (FWHM).

where E_o is the center energy and K (E) is a constant for the detector (Figure 2.3a). The energy deviation ΔE is determined by calibration. Full Width Half Maximum (FWHM) is a parameter commonly referred to the detector response and is given by

$$FWHM = \frac{(E_{1/2} - E_o) \cdot 2}{E_o}$$

For energies $E = E_o$ the energy response is equal to the constant $R(E_o) = K(E_o)$ and for energies $E = E_{1/2}$, $R(E) = K \cdot (E_o) \cdot 1/2$

The relation (3) gives $(\Delta E)^2 = (E_{1/2} - E_o)/\ln 2$ or, with $E_{1/2} - E_o = E_o \cdot (FWHM)/2$ inserted we get a useful relation between the energy scattering ΔE and the energy band width (FWHM):

$$(\Delta E)^2 = (FWHM \cdot E_o/2)^2/\ln 2.$$

A small bandwidth characterizes a good detector, while a large one has the effect of broadening peaks and smearing out gradients in the spectra. For the S17 detectors the energy band width varies between 10 and 20%, which was acceptable for the detectors contructed at the time.

2.2 Calibration of the CEM - detectors

All the detectors in the two S17 particle experiments were calibrated before flight. A block diagram of the used calibration facility at KGI is shown in Figure 2.4 (constructed and described by P. Christophersen, 1971). The electron gun gives a rather stable monoenergetic electron beam of good homogeneity for all energies measured in the S17 experiments. The beam intensity is measured by an electrometer and a Faraday cup at a point in the beam between the electron source and the detector. A correction is then determined to get the intensity at the detector distance. A movable flourescent plate can be brought into the beam in order to check the homogeneity of the beam instantly.

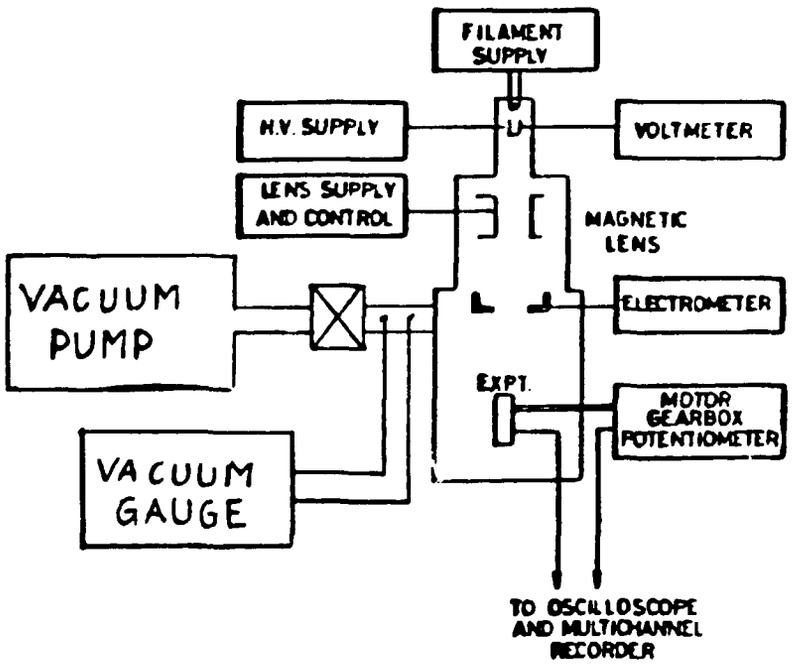

Figure 2.4 Diagrammatic representation of the calibration facility which was used for calibration of the S17 experiments.

The vacuum chamber of the calibration facility can accomodate a whole experiment box. Several detectors may be calibrated without changing the mounting of the box. Both the electron beam and the detector can be moved in order to get the right nominal center angles for the beam ($\alpha = 0$, $\beta = 0$).

The calibration facility provides a parallel monoenergetic electron beam with a flux S (electrons per $cm^2 \cdot s$). For a detector effective area, A, which depends on α, β and E, the geometric factor G for a given energy value E can then be written

$$G(E) = \int_{\alpha}^{\alpha+\alpha_0} \int_{\beta}^{\beta+\beta_0} A(\alpha,\beta) d\alpha \, d\beta.$$

In the calibration procedure the integration in α-direction was obtained by turning the detector in the α-plane around a longitudinal axis. In the β-plane the effective opening angle was assumed to be

$2\beta_{max} \approx b/r_m = \beta_o$. Thus $G(E) = \beta_o \int A(\alpha) d\alpha$. If the angular velocity of the α-scanning is ω(rad/s), $\alpha = \omega t$, and if A=N/S, (where N is the total electron flux over the detector aperture area) the geometric factor may be written

$$G(E) = \beta_o(\omega/S) \int_0^T N \, dt = \beta_o \omega \Sigma / S,$$ where Σ is the total number

of electrons that pass into the detector during the sampling period, T. G can thus be determined for different energies of the beam. The area below the $G(E,E_o)$ curve gives then the conversion factor $C(E_o) = \int G(E,E_o) dE$ for a given value of the deflection voltage (i.e. of E_o). Even the mounting of the analyzers in the detector box influences the value of $C(E_o)$, so the calibration has to be carried out with the detectors in their final positions within the experiment boxes.

The parameters, A, d, r_m, α_{max} and β_{max} of the instrument all have been chosen so that a sufficiently high - but not to high - countrate is obtained in the situation to be studied. For all the particle experiments in the two S 17 rockets the actual energy ranges, the viewing angles relative to the spin axis of the rocket, the apertures, the geometric and the conversion factors etc are presented in Table 2.1. The conversion factor C for the detector is defined by $j(E) \cdot C = N(E)$, where $j(E)$ = incoming particles per (cm^2 s sr keV) and $N(E)$ = countrate (counts per s). Accordingly the particle flux j can be determined by dividing the countrate N(E) with conversion factor C

$$j(E) = \frac{N(E)}{C} \text{ particles per } (cm^2 \text{ s sr keV}).$$

If the efficiency is η and the active surface of the channeltron is A, the conversion factor for this type of analyzer is given by

$$C = (16/9) \cdot (d/r_m)^3 \cdot b^2 \cdot \eta \cdot A \cdot E_0 (cm^2 sr \text{ keV}).$$

(Riedler, 1971).

2.3 Solid state detectors in S17 payloads

For particle energies above 40 keV solid state detectors were used in the S17 particle experiments. These were surface barrier detectors, i.e. large area diodes with a very thin layer of p-type material covering the sensitive face of an n-type wafer (silicon). The configuration is shown in Figure 2.5. The effective diameter D corresponds to the active area of the device; in the detectors of S17 the nominal active area was 25 mm^2 and the conical field of view amounted to $\Delta\alpha = \pm 15^\circ$ (see Figure 2.6)

The detector depletion depth in the SSD-detectors on S17 was 300 µm, which stops particles of energies less than 400 keV. The calibration of the detectors was made with radio-active isotopes Cd 109 and Ce 129 as electron sources. These electron

PAYLOAD	SPECIES	VIEWING DIRECTION (DEG)	APER-TURE (MM)	d/r_m %	ENERGY E_0 (keV)	$\Delta E/E_0$ %	CONVER-SION FACTOR $\cdot 10^4$ (cm^2 srkeV)	GEOMET-RIC FACTOR $\cdot 10^4$ (cm^2 sr)
S 17 1M	ELECTRONS SWEPT	0	3 × 3	10	0.9	14.8	0.6	0.6
					2.0	12.5	1.3	1.5
					4.1	11.1	2.3	3.6
					8.0	10.8	3.6	7.4
					15.6	10.6	5.4	12.8
2M	ELECTRONS SWEPT	0	3 × 3	10	1.2	13.8	1.0	1.0
					2.3	12.9	1.8	2.2
					4.3	11.2	2.7	4.3
					8.2	13.2	4.4	9.0
					15.5	12.3	6.7	15.9
1M	ELEC FIX	25	3 × 3	10	2.0	10.0	0.6	0.7
2M	" "	25	3 × 3	10	2.0	11.6	1.1	1.3
1M	ELEC FIX	25	3 × 3	10	8.5	11.0	4.3	8.8
2M	" "	25	3 × 3	10	8.3	13.9	3.3	6.8
1M	PROT FIX	25	5 × 9	20	1.0	19.0	12.8	12.9
2M	" "	25	5 × 9	20	1.0	21.8	13.4	13.5
1M	PROT FIX	25	5 × 9	20	4.1	18.5	42.6	67.3
2M	" "	25	5 × 9	20	4.4	20.7	31.9	51.7
1M	ELECTRONS STEPPED	150	2 × 6	10	0.8	16.7	1.5	1.5
					2.0	16.5	2.7	3.0
					4.2	14.0	5.0	7.9
					8.6	11.1	9.3	19.3
					16.8	12.8	15.6	36.7
2M	ELECTRONS STEPPED	150	2 × 6	10	1.1	10.2	0.5	0.5
					2.2	10.6	1.5	1.8
					4.4	10.2	2.5	4.0
					8.9	10.1	5.6	11.7
					17.1	10.5	7.8	18.9
1M	PROTONS STEPPED	25	5 × 9	20	0.5	24	9.2	9.3
					1.0	21	14.9	15.1
					2.2	18	34.3	40.4
					4.4	17	50.8	82.9
					8.4	16	80.5	166.0
2M	PROTONS STEPPED	25	5 × 9	20	0.6	15	25.5	25.5
					1.1	19	26.5	26.8
					2.2	20	35.2	41.7
					4.4	18	57.4	93.1
					8.5	20	97.2	200.8
1M	ELECTRONS STEPPED	25	3 × 3	10	1.1	10	0.2	0.2
					2.3	10	0.5	0.6
					4.4	9	0.9	1.4
					9.1	10	1.6	3.4
					17.8	10	2.4	5.8
2M	ELECTRONS STEPPED	25	3 × 3	10	1.0	12	0.4	0.4
					2.2	11	0.9	1.1
					4.4	10	1.5	2.4
					8.7	13	2.4	4.9
					17.6	12	3.0	7.3
1M	ELECTRONS STEPPED	80	3 × 3	10	1.1	9	0.5	0.5
					2.3	11	1.1	1.4
					4.5	11	1.7	2.8
					9.0	11	2.8	5.8
					17.5	10	3.7	9.0
2M	ELECTRONS STEPPED	80	3 × 3	10	1.0	11	0.8	0.8
					2.0	12	1.9	2.1
					4.1	11	3.0	4.6
					8.3	11	5.4	11.1
					16.6	11	8.3	20.0
1M	PROTONS STEPPED	80	5 × 9	20	0.5	16	2.0	3.0
					1.0	20	12.9	13.0
					2.0	18	26.0	30.0
					4.0	17	41.5	64.9
					7.8	20	74.1	149.4
2M	PROTONS STEPPED	80	5 × 9	20	0.5	20	10.0	9.8
					1.0	19	16.6	16.7
					2.2	22	34.3	40.3
					4.2	18	56.0	89.4
					8.4	19	95.4	196.3
S 17 1D	ELEC FIX	30	3 × 3	10	1.9	13	1.0	2.3
2D	" "	30	3 × 3		2.3	12	0.8	0.9
1D	ELEC FIX	30	3 × 3	10	8.1	10	5.6	11.5
2D	" "	30	3 × 3		8.2	12	3.0	6.1
1D	PROT FIX	30	5 × 9	20	1.0	20	17.1	7.8
2D	" "	30	5 × 9		1.2	18	7.7	7.9
1D	PROT FIX	30	5 × 9	20	4.1	19	40.6	63.2
2D	" "	30	5 × 9		4.3	21	26.8	43.0

Table 2.1 Calibration result and some geometric data for the CEM detectors of the S17 payloads.

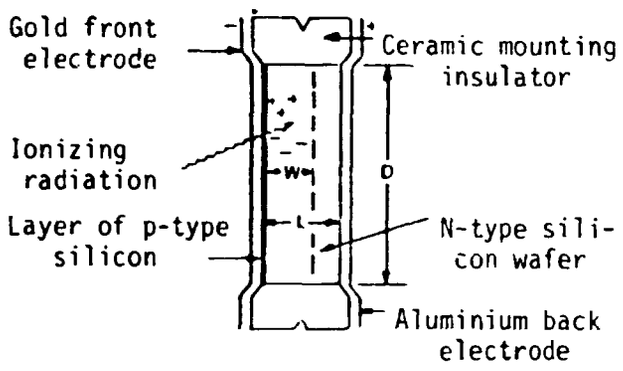

Figure 2.5

Schematic of a Surface Barrier Detector.

sources gave four discrete lines in the energy spectrum and the corresponding pulse magnitudes in mV were obtained.

From that linear calibration curve with the output pulses as a function of the particle energy the discriminating levels were interpolated. These were for the S17 experiments 40, 60, 90, 120 and 150 keV for the mother detectors and 40, 60, 90 and 120 keV for the daughter detectors.

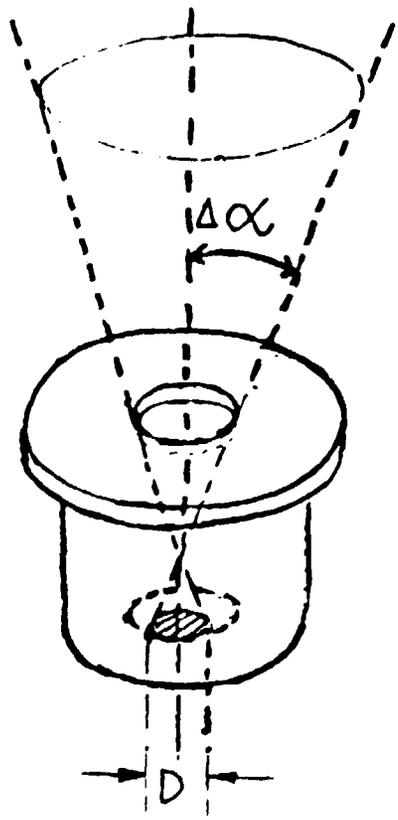

Figure 2.6 The definition of the viewing angle of an SSD - detector.

The SSD-detectors can be used for measurements of either electrons or both electrons and protons. If designed for measuring only electrons, the detector is covered by an absorbing layer of gold or aluminium. This layer (≈200 $\mu g/cm^2$) stops protons of energies less than about 400 keV, but the electrons pass through it with a very low energy loss (≈18 keV).

By comparing an electron measuring detector with a detector, which is measuring both electrons and protons, it is possible to derive the proton flux from the difference in the counting rates of the two detectors (provided they have identical geometrical factors).

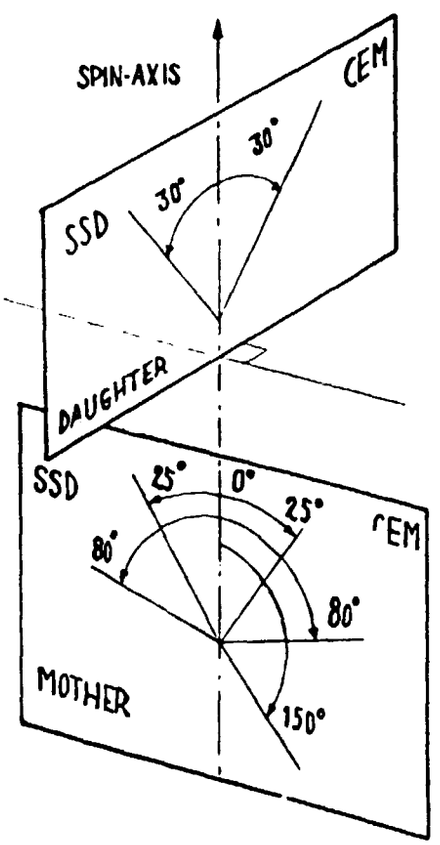

Figure 2.7 Mounting of the detectors in the S17 payloads.

2.4 Mounting of the detectors

The mounting of the detectors in the payloads is shown in Figure 2.7. In both mother and daughter payloads the CEM detectors were mounted at one side and the SSD detectors on the opposite side (180° difference in azimuth). The detectors were looking at 0°, 25°, 80° and 150° from the spin axis in the mother payload and 30° from the spin axis in the daughter payload. In the mother payload a swep detector for the energy range 0.1 - 16 keV was mounted in the direction of the rocket spin axis.

Details of the 14 particle detectors of CEM type are listed in Table 2.1 and the 6 SSD detectors are presented in Table 2.2. The wave forms of the reference voltages applied to the swept and stepped detectors are shown in Figure 2.8.

2.5 The efficiency of channel multipliers

The efficiency of channel multipliers depends on the particles energy and decreases with increasing energy. This decrease has been found to be accurately represented by

$$\eta(E) = 1 - \frac{2}{3 + \frac{6.5}{(E-0.5)} + \frac{30}{(E-0.5)^3}} \qquad (4)$$

(Archuleta and de Forest, 1971).

Figure 2.9 shows for an example from the S17-2 payload how the conversion factor is influenced by the efficiency and Figure 2.10 shows graphically the result of the calibration of the energy response for one of the CEM detectors in the S17-1 payload (80° stepped electrons).

Payload and detector	Energy (keV)	Viewing direction (degrees)	Field of view (degrees) $\Delta\alpha$	Conversion factor (cm^2 erkeV)
S 17 M, 1 & 2 SSD1, SSD3	>40, 60, 90, 120, 150 (electrons)	25	±15 (conical)	$1.40 \cdot 10^{-2}$
S 17 M, 1&2 SSD2, SSD4	>40, 60, 90, 120, 150 (electrons, protons)	25	± 15	$1.40 \cdot 10^{-2}$
S 17 D, 1&2 SSD1	>40, 60, 90, 120 (electrons)	30	± 15	$1.40 \cdot 10^{-2}$
S 17 D, 1&2 SSD2	>40, 60, 90, 120 (electrons, protons)	30	± 15	$1.40 \cdot 10^{-2}$

Table 2.2 The SSD - detectors in the payloads of S17.

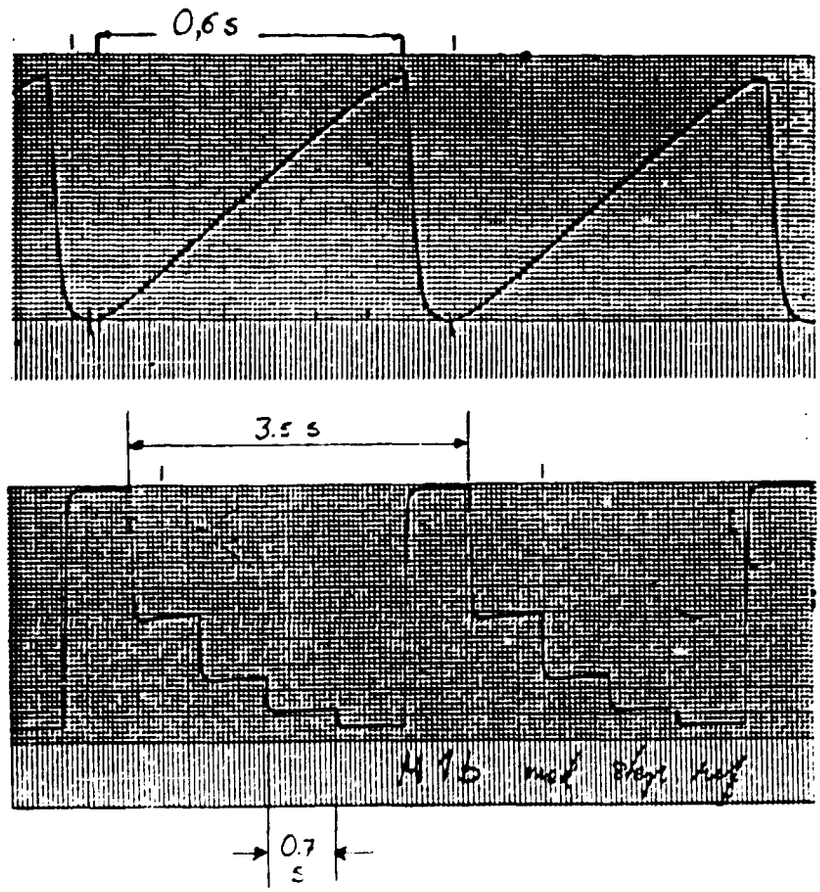

Figure 2.8 The wave form of the reference voltage applied to the swept 0° electron detector and the stepped electron detectors in the mother payloads.

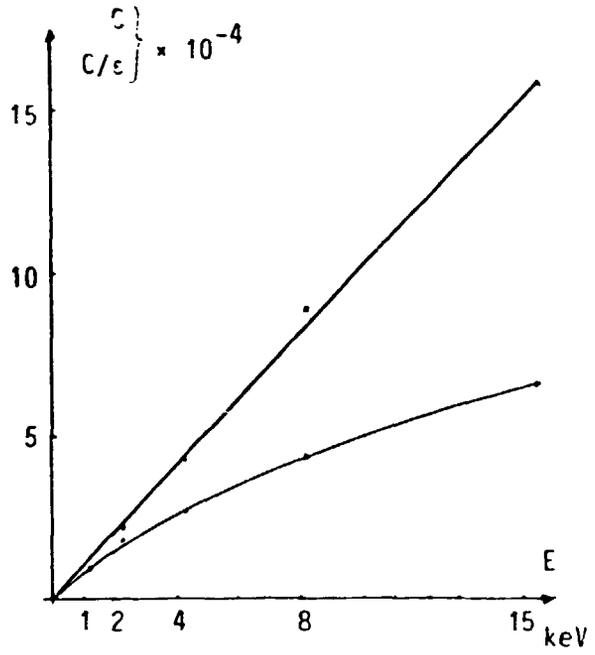

Figure 2.9 The energy dependence of the conversion factor and the efficiency for a CEM - detector.

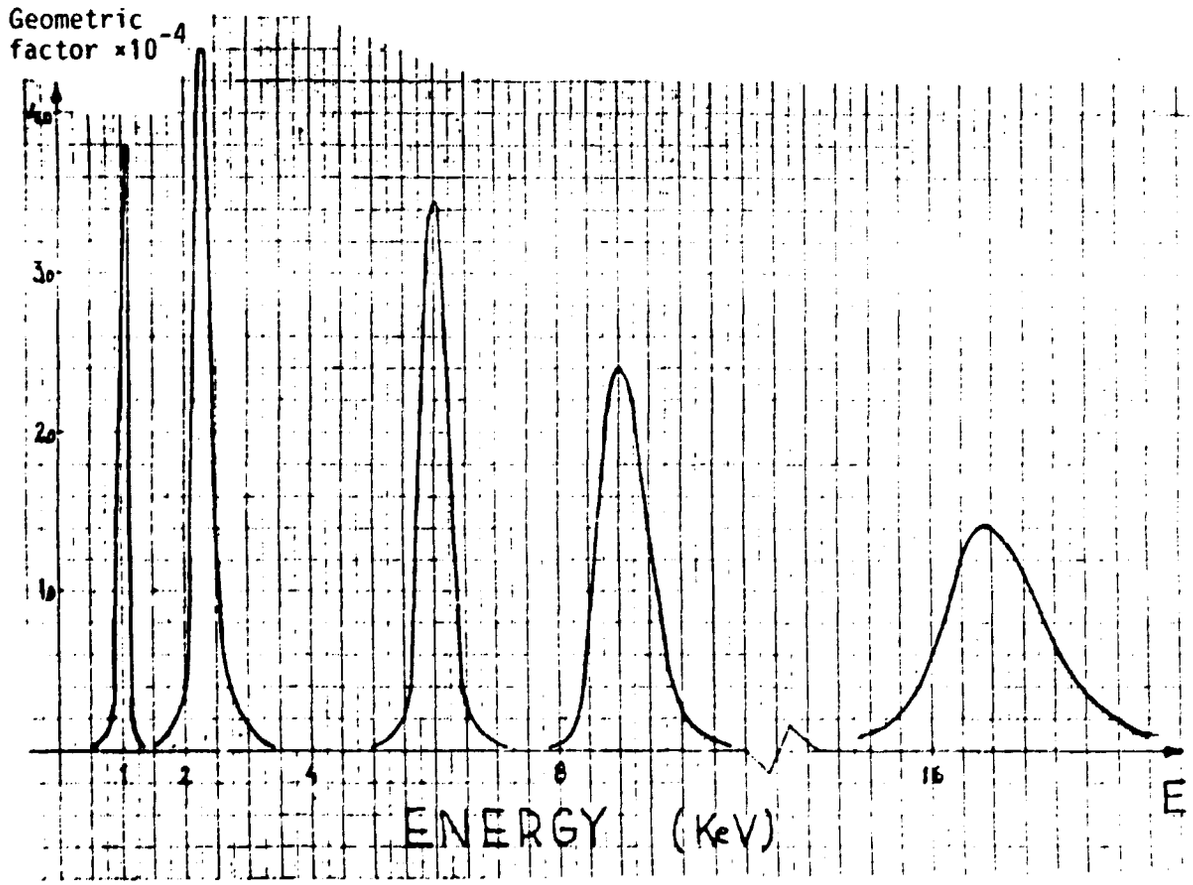

Figure 2.10 Calibrated energy response for a CEM - detector (80° electrons stepped).

3. Review of the geophysical conditions during the S17 flights and presentation of some supporting observations

3.1 The auroral situation during S17 flights

The auroral situation during the S17-1 launch was one of a growing phase of an evening auroral substorm. A faint straight auroral arc had been standing south of and above Esrange for about one hour before the launch. This east - west directed arc showed an intensity enhancement at 18.58 UT and started to move northward, shortly after which the rocket was launched. The rocket did not intersect the most intense arc in the breakup but crossed several other visual aurora structures. S17-1 was launched at the very beginning of the rocket campaign.

The rocket S17-2 was launched on the last night of the campaign. The auroral activity was very high, the launching was between two 900 nT substorms at a depression of the northward geomagnetic component of about 300 nT (see Figure 3.2). The auroral conditions were highly disturbed and very intense auroral occurred on and around the rocket trajectory at launch time. Due to a rapid change of the situation most of the aurora disappeared during the rocket flight. In spite of this, a couple of auroral structures were intersected and some precipitation events of considerable interest were recorded by the detectors.

3.2 Magnetic activity

The experiments on the two S17 sounding rockets were supported by extensive groundbased observations. Standard magnetograms obtained at Kiruna Geophysical Institute are reproduced in Figures 3.1 and 3.2 (upper part). The K-indices giving a measure of the auroral electrojet are presented in Table 3.1 for the time periods when the two launches took place. During the International Magnetospheric Study (IMS) program a magnetometer array, called Scandinavian Magnetometer Array (SMA), was operated and data from these magnetometers was available for comparison with S17 measurements. Such comparisons will be discussed in Chapter 4.

Magnetic K-Indices - Lower limit of K = 9 is 1500 nT

Time in UT

January 1976

Day	00 - 03	03 - 06	06 - 09	09 - 12	12 - 15	15 - 18	18 - 21	21 - 24	K-sum
15	0	0	0	0	1	2	4	4	11
16	3	2	0	1	1	2	6	6	21
17	2	3	3	1	2	2	5	4	22
18	5	2	2	2	2	0	3	3	19
19	2	1	1	1	1	2	4	4	16
20	2	1	1	1	1	3	4	5	18
21	2	3	2	3	3	5	6	2	26
22	2	4	1	1	4	4	* 6	5	27
23	6	4	3	3	5	5	5	3	34
24	4	2	2	3	2	4	5	4	26
25	3	2	1	2	3	3	3	1	18
26	0	1	0	1	1	1	2	1	7
27	0	1	2	1	1	1	0	1	7
28	1	0	0	0	1	1	2	2	7
29	1	1	1	0	1	0	0	1	5
30	0	0	0	0	1	3	5	5	14
31	3	2	2	2	6	6	4	7	32

March 1976

Day	00 - 03	03 - 06	06 - 09	09 - 12	12 - 15	15 - 18	18 - 21	21 - 24	K-sum
1	4	4	2	2	3	2	3	5	25
2	3	5	3	3	5	6	6	6	37
3	7	4	4	3	2	5	7	7	39
4	5	3	2	2	2	2	3	2	21
5	1	2	1	2	3	4	4	6	23
6	5	4	3	2	5	6	6 *	8	38
7	7	4	4	3	3	4	6	7	38
8	7	6	4	4	4	4	5	6	40
9	6	6	3	3	4	5	6	7	40
10	6	5	3	3	4	6	6	8	41

The following scale has been used:

K-indices	Deflection in nT
0	0 - 15
1	15 - 30
2	30 - 60
3	60 - 120
4	120 - 210
5	210 - 360
6	360 - 600
7	600 - 990
8	990 - 1500
9	1500 and more

Table 3.1 The reading of maximum deflection of the two components X and Y made during each 3-hour interval starting from 00 to 03 UT (Kiruna Geophysical Data, 1976). Rocket launches are marked with a cross (*).

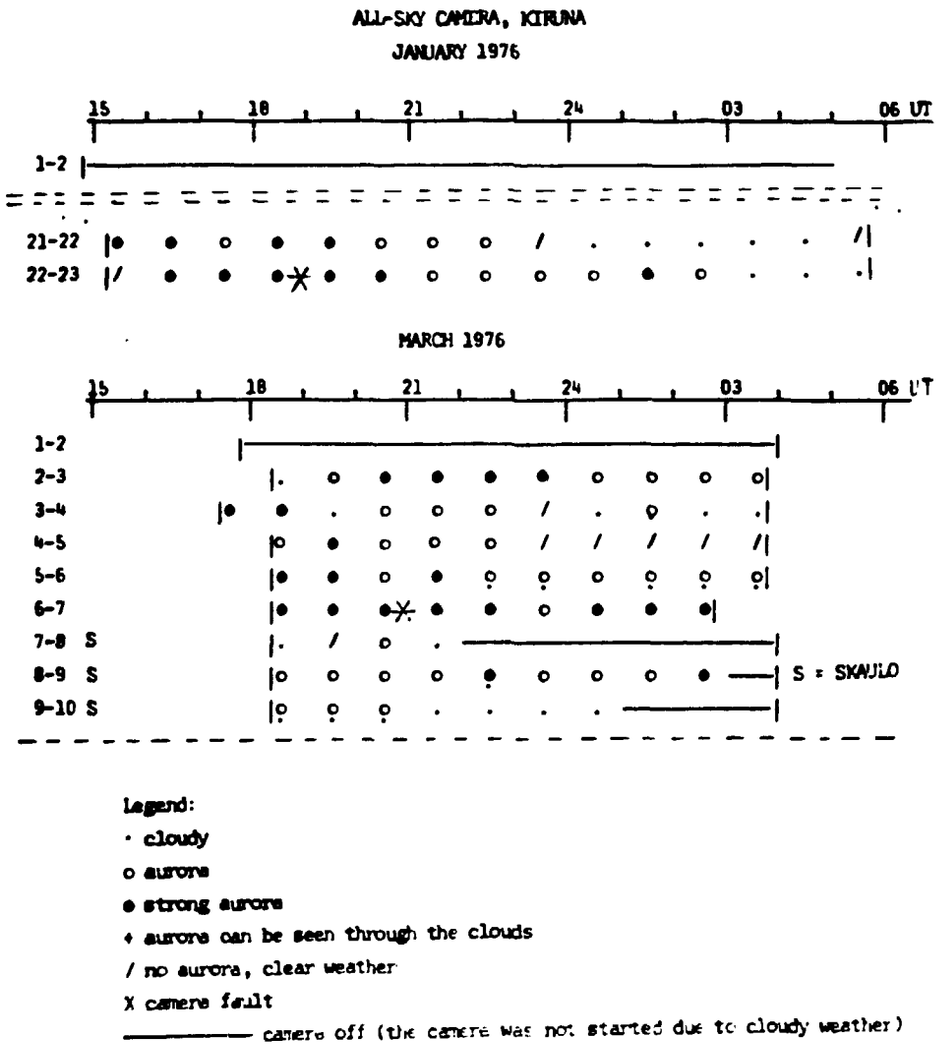

Table 3.2 Available records of all-sky camera films obtained at Kiruna Geophysical Institute (Kiruna Geophysical Data, 1976).
Rocket launches are marked with a cross (*).

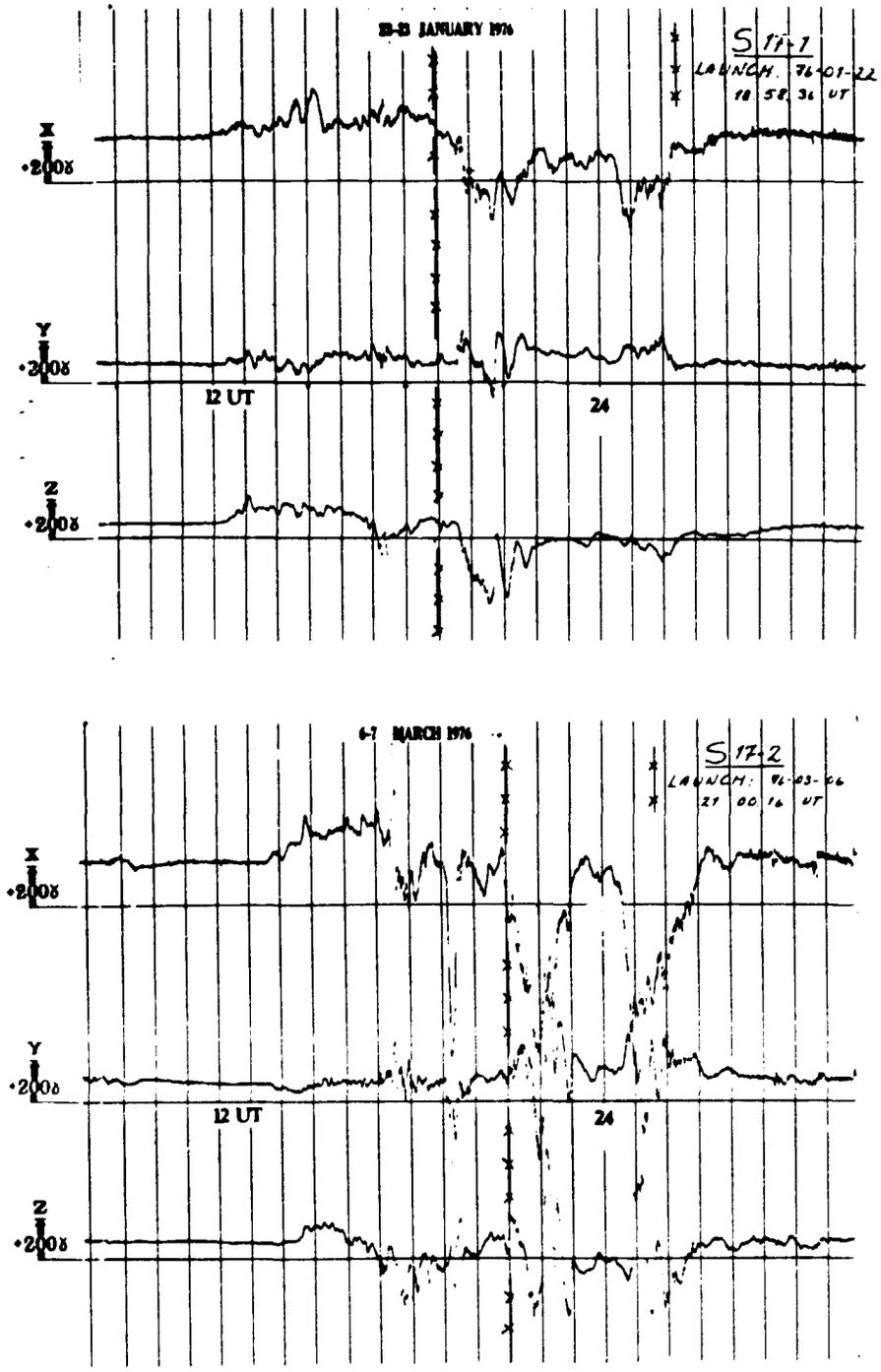

Figure 3.1 Kiruna magnetogram 22 - 23 January and 6 - 7 March, 1976. The times of rocket launching are marked with crosslines (‡).

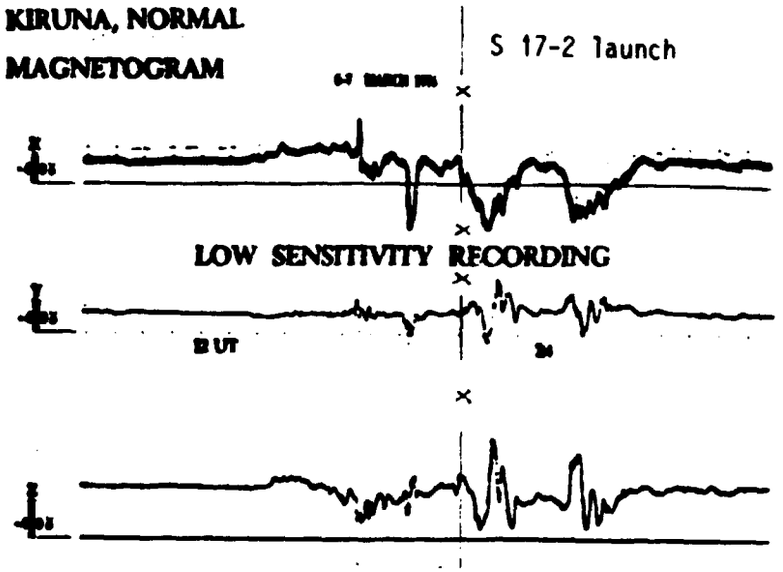

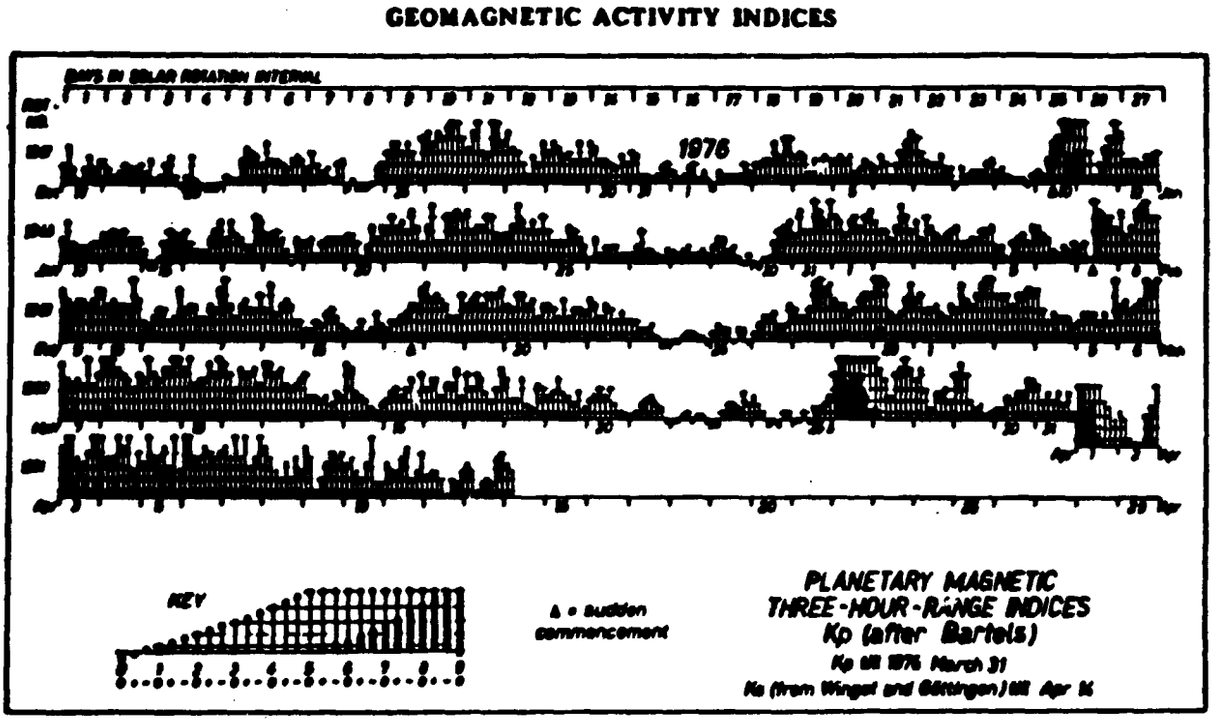

Figure 3.2 A low sensitivity recording of Kiruna magnetogram 6-7 March, 1976 and a longer time history (17 December 1975 - 13 April 1976) of the Kp indices.

3.3 Other supporting observations

All-sky films were obtained from cameras at Esrange, at KGI in Kiruna and at Skaulo. Information about available records of the all-sky camera films obtained at KGI is given in Table 3.2. The all-sky camera at KGI-Kiruna is located approximately 28 km west of Esrange. The all-sky photographs were taken at a rate of one frame per minute on 16 mm black and white film. Information of the camera operation and an average over the hour of auroral intensity and weather situation is included in Table 3.2.

ATS - 6 experimenters have provided data from particle measurements on this satellite. At the time for launching of the S17 rockets the ATS - 6 satellite will be discussed in Chapter 4. During the S17-2 flight also a photometer-TV system was operated at KGI-Kiruna.

3.4 The lowlightlevel-TV-system

A low-light-level-television-system supplied by UJO (courtesy of B. Holback) was operated by KGI staff at Rappsåive. This station is situated close to the nominal impact point of the payloads and that gave a unique possibility to record the aurora as seen along the field lines. In this way a better geometrical resolution was obtained than in previous sounding rocket campaigns. The TV system worked very well during the first S 17 flight, but unfortunately a technical failure prevented the use of the system during the second flight. The TV camera operating at Rappsåive covered 45^{o} horizontal and 39^{o} vertical viewing angles. The camera was directed nominally 0^{o} in azimuth and 80^{o} in elevation. The time for the upper culmination of some very bright stars was used as fix points in adjusting the direction of the camera. At the upper culmination the star is seen at the meridian line in the south and at the time it should be seen exactly on the symmetry line of the camera. The camera had to be mounted daily so this adjustment took place every day.

Figure 3.3a S17-2 rocket was launched on a night with a highly disturbed magnetic situation and a rapidly changing auroral display. All-sky photos from Esrange at 20.12.00, 20.13.00, 21.55.00 and 21.56.00 UT.

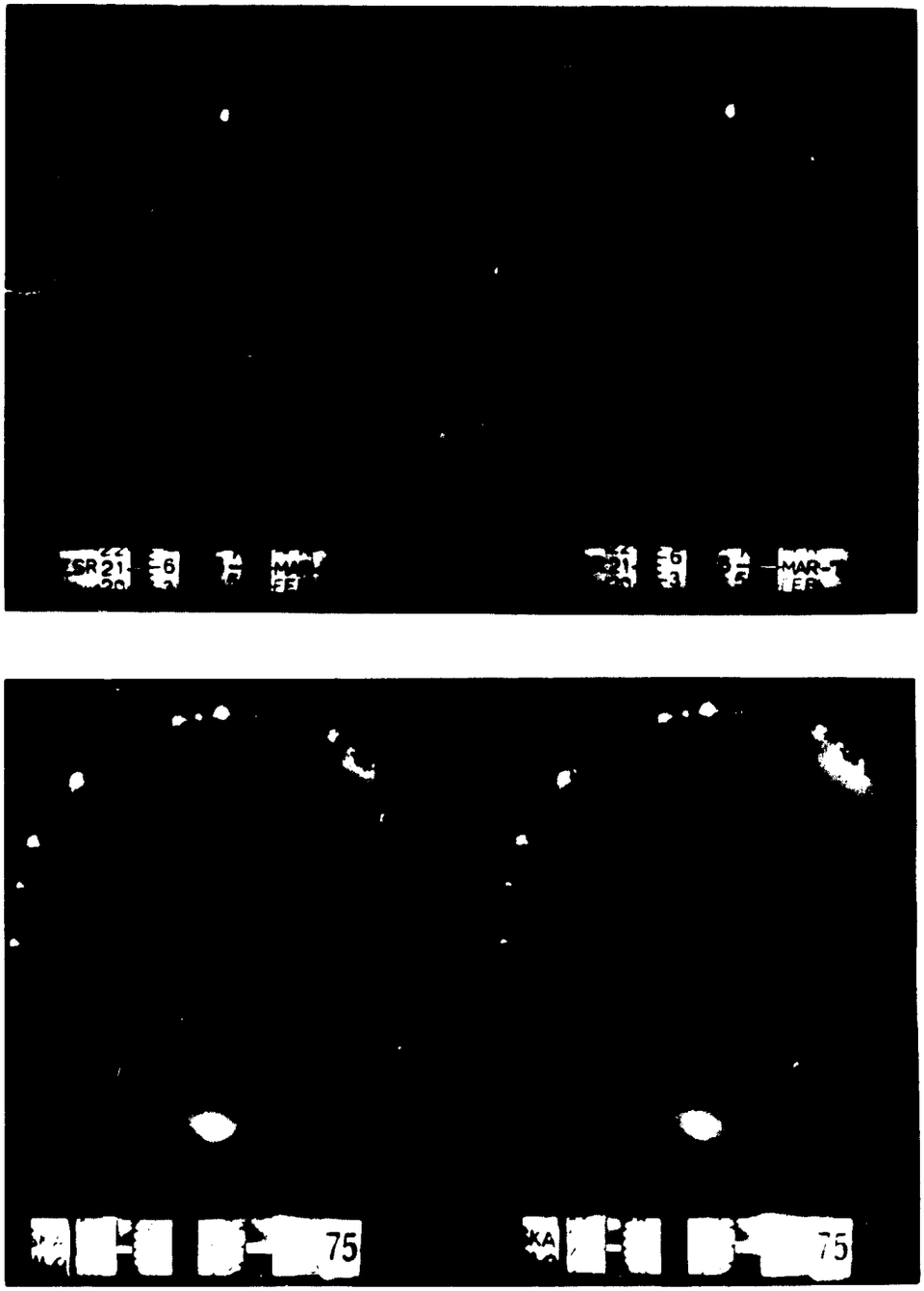

Figure 3.3b All-sky photos from Esrange and Skaulo at the flight time = 230 s of S17-2 showing no aurora during the burst in the particle fluxes (see Figure 4.20).

In order to relate the payload position to the low-light-level TV-recording of the visual aurora, the upper part of the trajectory of the payload was projected along the earth's magnetic field lines onto an auroral standard height. For the S17-1 mother payload an altitude of 110 km was chosen. Figure 3.4 shows this projection which was made with the assumption that the geomagnetic field lines are parallel straight lines between the rocket peak altitude and the projection altitude level 110 km.

According to Figure 3.4 you have

$$\text{tg } i = \frac{z - 100}{D}$$

$$D = (z - 110)/\text{tg } i$$

$$\cos d = \Delta x/D \quad \text{and } \Delta x = D \cos d$$

$$\sin d = \Delta y/D \quad \text{and } \Delta y = D \sin d \text{ and thus}$$

$$\begin{cases} x^1 = x + \Delta x = x + \cos d \cdot (z - 110)/\text{tg } i \\ y^1 = y + \Delta y = y + \sin d \cdot (z - 110)/\text{tg } i \\ z^1 = 110 \end{cases}$$

which are the coordinates in the launcher coordinate system of the projected trajectory point.

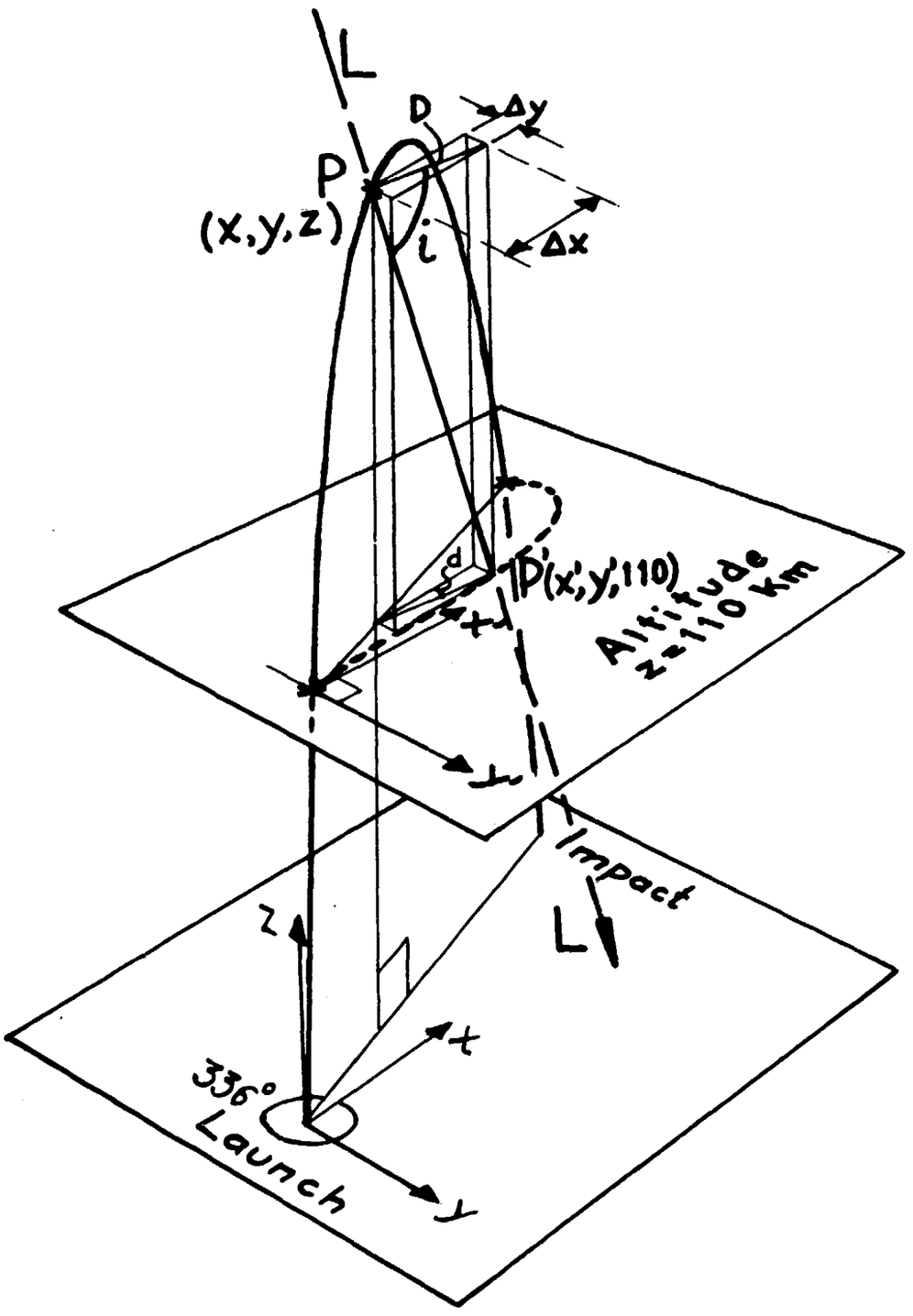

Figure 3.4 Projection of the upper part of the rocket trajectory down to an altitude of 110 km. P is the payload position at the trajectory, P^1 is the projection of this position onto 110 km height. L is an earth magnetic field line.

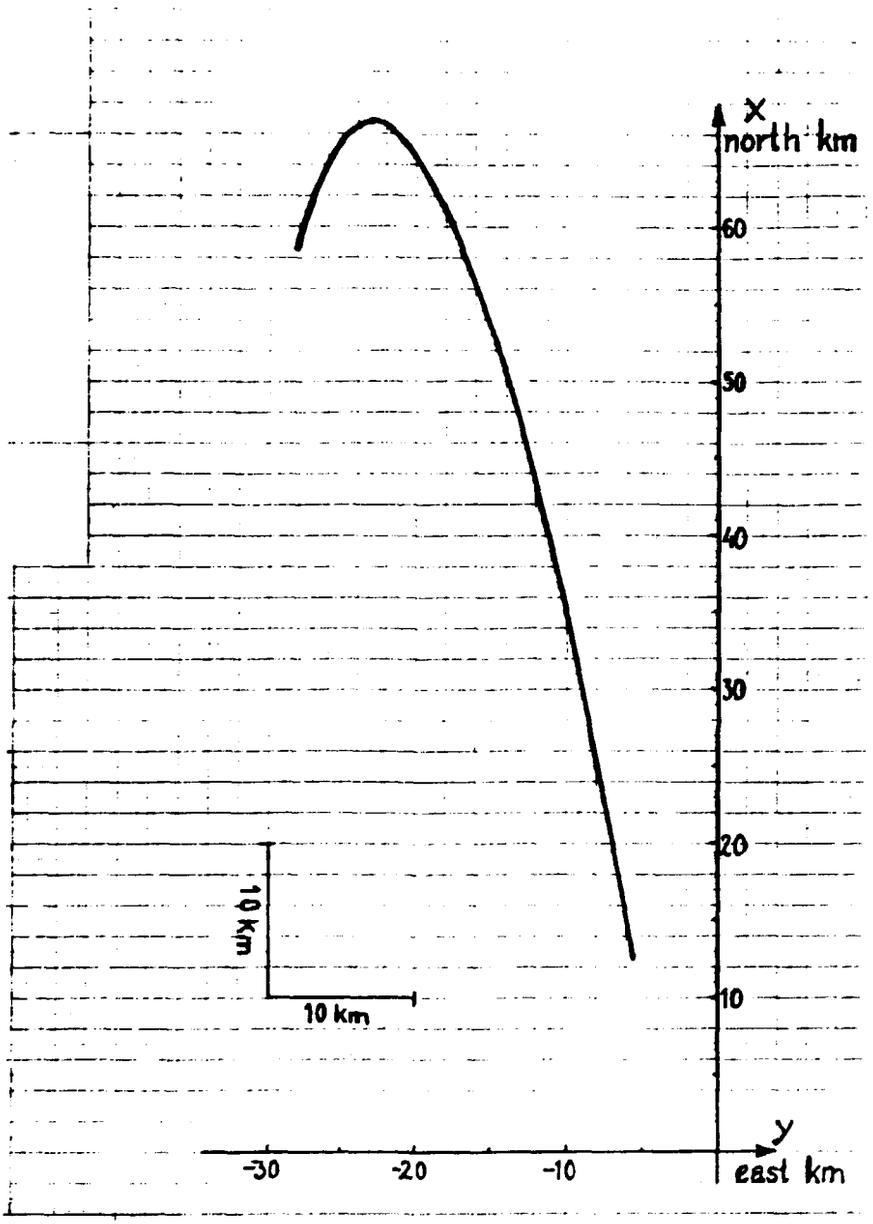

Figure 3.5 Coordinates in the launcher frame of reference of the payload trajectory projection onto 110 km altitude. (Payload: S17-1 mother).

DAY	α - AURIGAE		β - AURIGAE		α - URSA MAJORIS		β - URSA MAJORIS	
	TIME (UT)	HEIGHT	TIME(UT)	HEIGHT	TIME(UT)	HEIGHT	TIME(UT)	HEIGHT
15 FEBR	18.18	68°	19.00	67°	00.05	84°	00.03	79°
16 FEBR	18.14	68°	18.56	67°	00.01	84°	23.59	79°
17 FEBR	18.10	68°	18.52	67°	23.57	84°	23.55	79°
18 FEBR	18.06	68°	18.48	67°	23.53	84°	23.51	79°
19 FEBR	18.01	68°	18.44	67°	23.49	84°	23.47	79°
20 FEBR	17.57	68°	18.40	67°	23.45	84°	23.43	79°
21 FEBR	17.53	68°	18.36	67°	23.41	84°	23.39	79°
22 FEBR	17.49	68°	18.32	67°	23.37	84°	23.35	79°

Figure 3.6 The upper culmination of some easy recognized bright stars which were used as fix points by adjusting the camera direction.

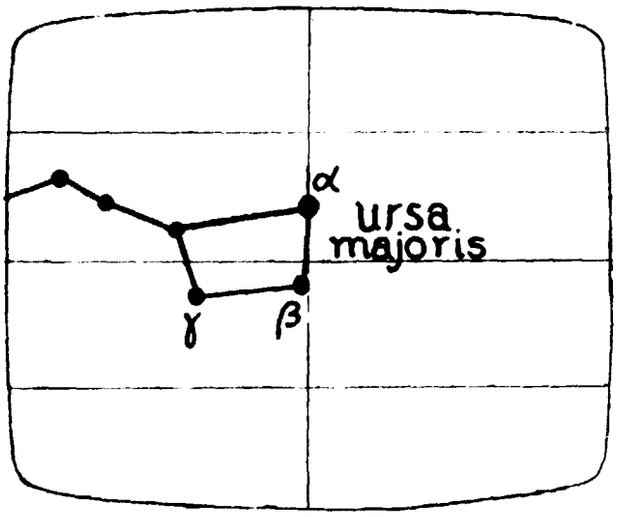

Figure 3.7 Here is shown how the star α - URSA MAJORIS stays on the south meridian and 84° height at the time 1976.02.15. 00.05.00 UT.

18.59.59 UT
18.59.00 UT
18.57.00 UT
19.00.30 UT
18.59.30 UT
18.58.00 UT

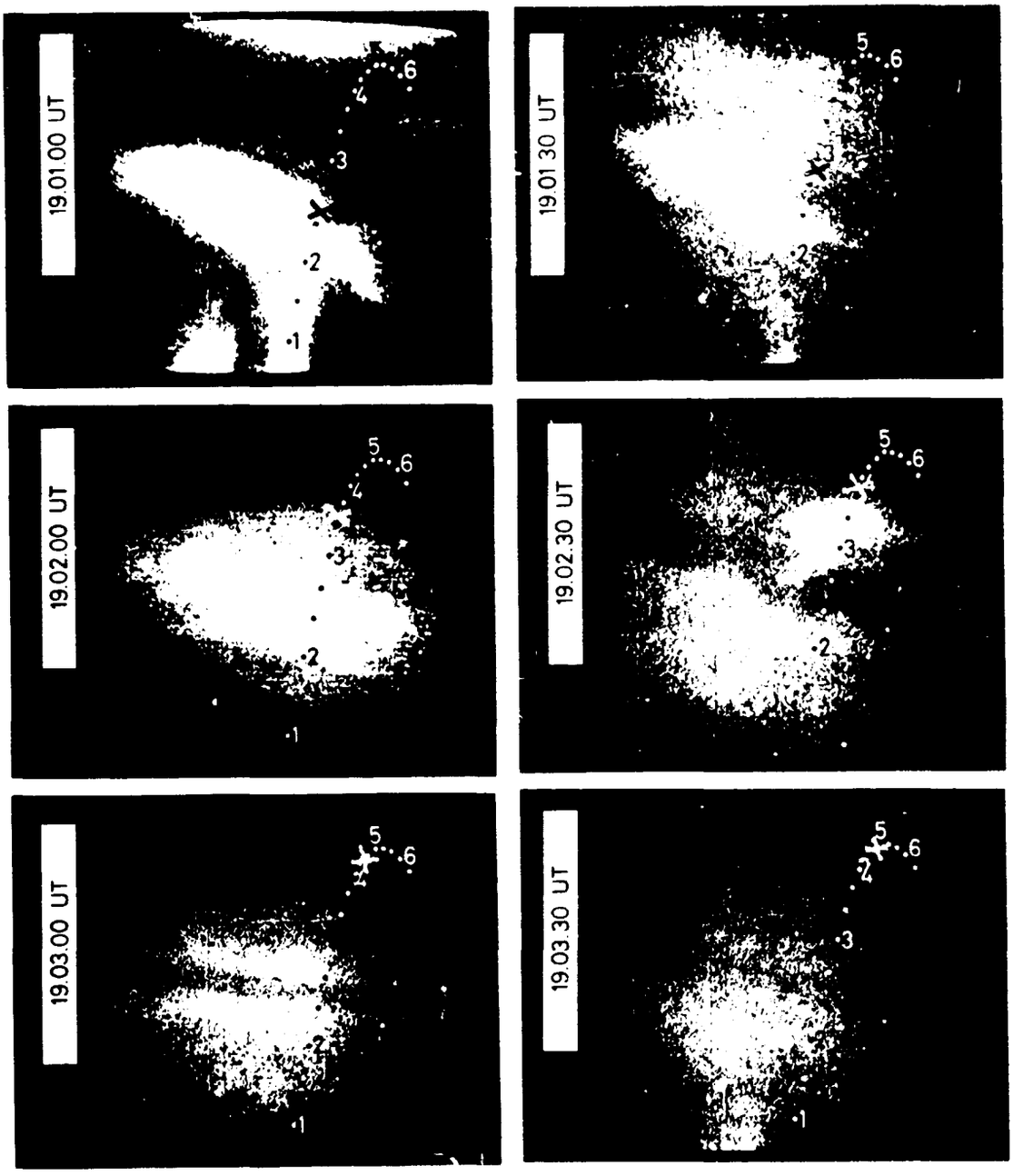

Figure 3.9 Due to the northward movement of the auroral the rocket also reaches the most intense part of the inter [illegible] of the rocket [illegible]

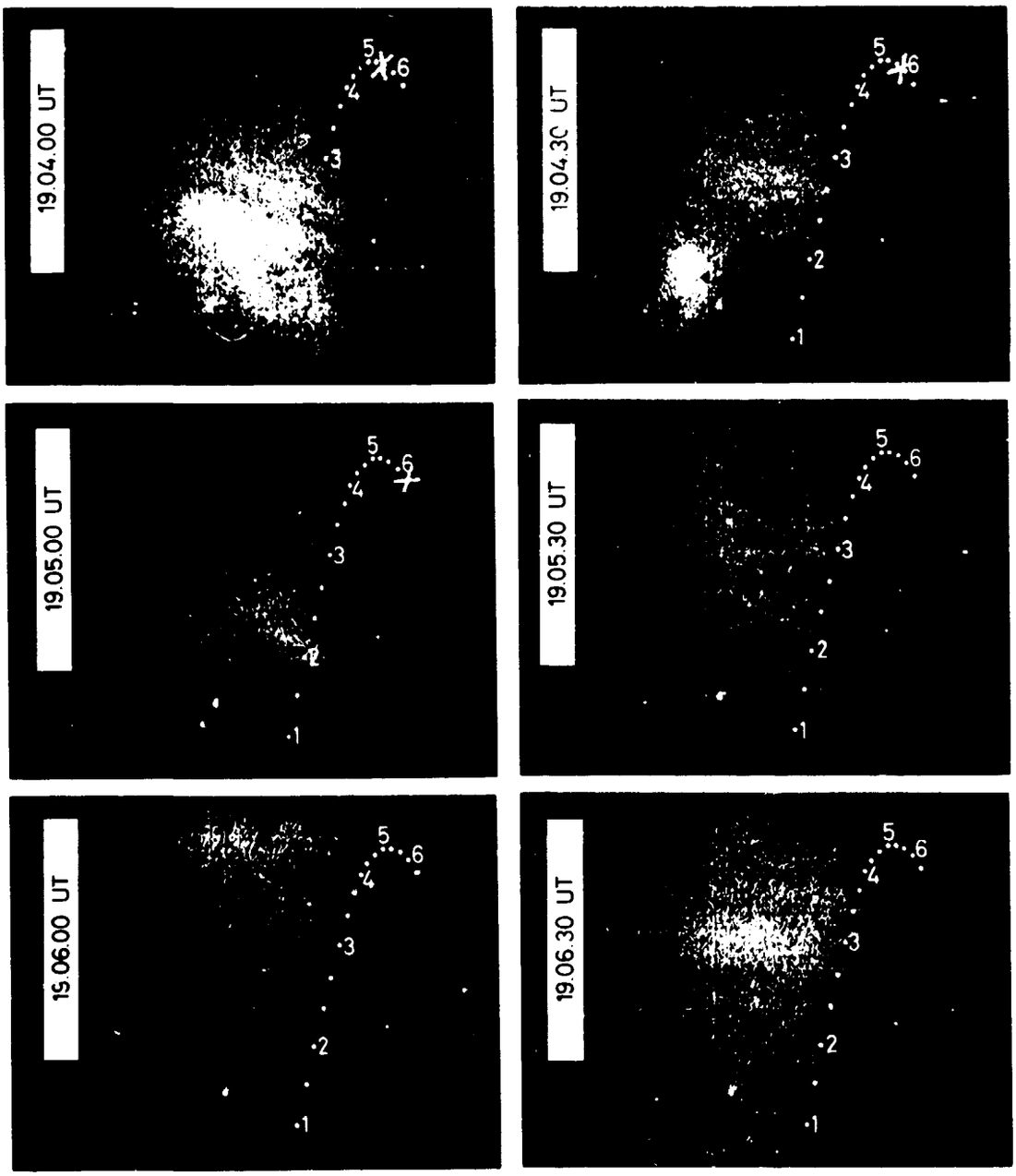

Figure 3.10 TV-film obtained from Kappelrod at the S17-1 launch. At the end of the rocket flight the aurora changed to a more diffuse and uniform structure and the intensity decreased. The rocket position is marked with a cross.

4. Particle fluxes and electric currents coupling the magnetosphere and the ionosphere during a magnetospheric substorm

4.1 Review of some substorm terminology and definitions

Local variations in the magnetic field components at the earth's surface originate from the interaction between the solar wind and the earth's magnetosphere. Such local disturbances are recorded by means of magnetometers. When these magnetic field disturbances are intense enough there is a magnetic substorm.

Simultaneously with the magnetic disturbances there are also a large number of other phenomena in the magnetosphere, like particle precipitation into the upper atmosphere causing auroral display, ionospheric disturbances, increased magnetospheric convection, redistribution of the hot plasma etc. The whole set of the disturbances is called a magnetospheric substorm.

Many types of magnetic disturbances have been classified and their occurence has been suggested to be coupled to existing currents somewhere in the near earth space. The first one who suggested such a relationship was Birkeland (1908, 1913), who

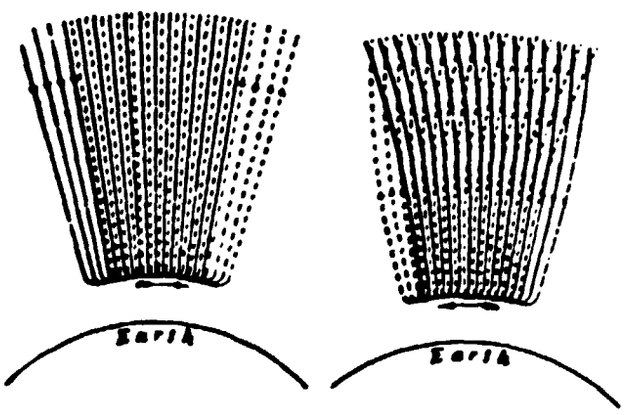

Figure 4.1

The system of field-aligned currents originally suggested by Birkeland (1908).

observed large structured magnetic variations at auroral latitudes. Birkeland proposed that intense auroral displays are coupled with intense currents along the direction of the auroral arc. These horizontal currents could then create a current circuit together with vertical currents along the auroral rays i.e. along the magnetic field lines. In the last decades such field-aligned currents have generally been called Birkeland currents (see Schield et al., 1969). The fact that the magnetic field disturbances are rather local, suggested that the currents are also spatially limited.

During the 1960s (see Akasofu, Meng et al., 1969) and during the 1970s (Kisabeth, Rostocker et al., 1974) a lot of work has been done to investigate the magnetophere-ionosphere current system. The main purpose of these investigations has been and in fact still is, to find an ionospheric current system, which is fully relevant to all the variations that are recorded in the magnetophere during a substorm. Such current systems have been derived for many polar magnetic disturbances. Figure 4.2 is an example, which shows a strong concentration of the flow lines to a westward directed current along the border on the night side of the polar cap. Across the circular cap there exists a roughly constant current flow over the polar cap directed from dawn to dusk (Silsbee and Vestine, 1942). Several other models of a current system in the ionosphere have been introduced. Measurements from satellites (Cummings et al., 1968) and sounding rockets (Cloutier et al., 1970) have confirmed a three dimensional model for the ionospheric currents proposed by Boström (1964) (see Figure 4.3).

The gross changes of the earth's magnetic field are lasting for periods from one or a few hours for substorms to some days for storms, and a chronology is observed in the development of the field variations. During a magnetic storm, besides the great variations in the magnetograms, a strong energy transport from the outer to the inner magnetosphere is observed. The currents in the ionosphere increase and decrease and strong gradients are seen in the particle fluxes.

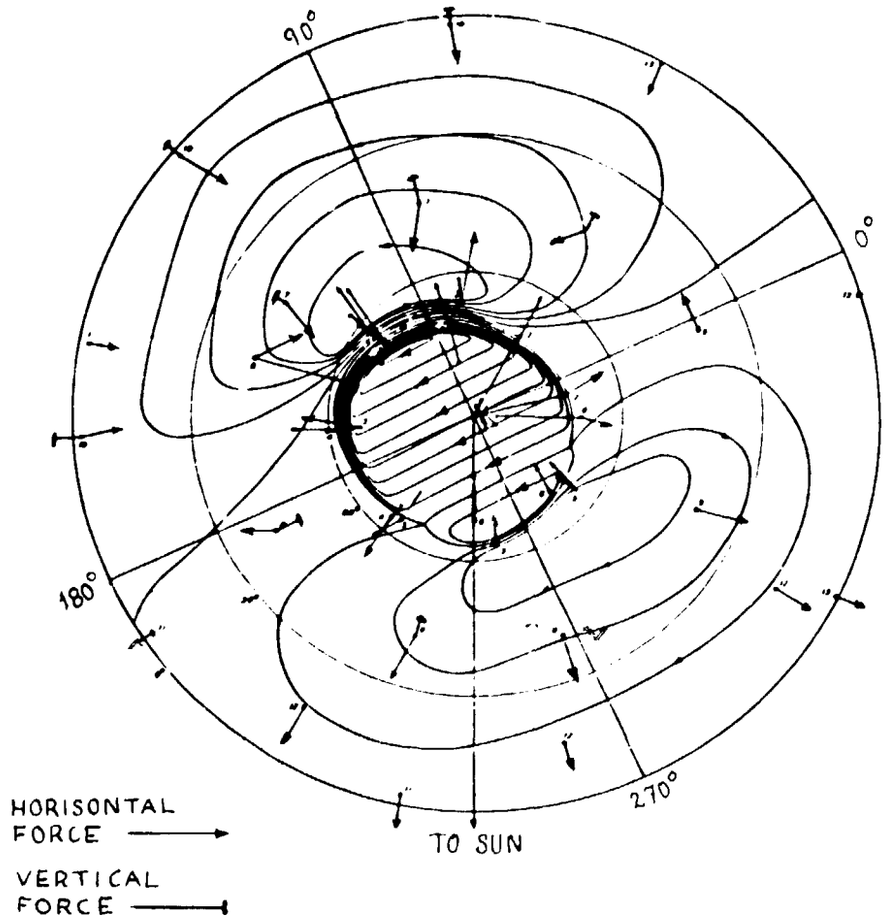

Figure 4.2 The current pattern in the disturbed polar cap according to Silsbee and Vestine.

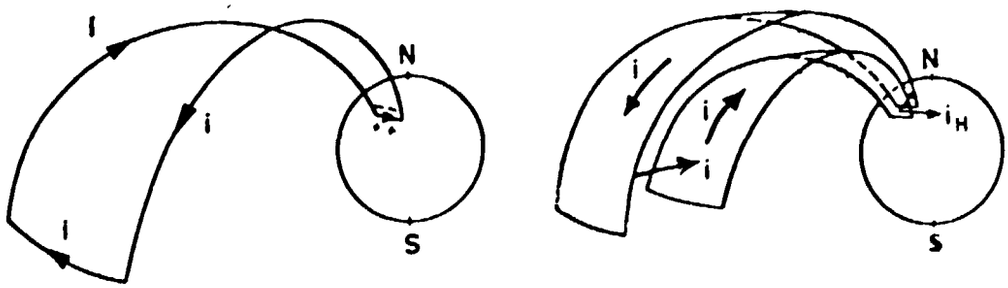

Figure 4.3 Two basic models of a three dimensional current-system in the ionosphere (Boström, 1964).
a) model I b) model II

The forms and the intensity of the visual aurora are changing, which is clearly seen in the cameras and photometer recordings. In the ionograms onsets of ionospheric absorptions are evident during such a violent magnetopheric process. In many studies of magnetospheric substorms one has defined the occurrence and time sequence of substorms. These studies have led to a further development of the chronology. A magnetic substorm is nowadays divided into three phases

1) the growth phase, before the onset of the active phase (McPherron, 1972)
2) the expansive phase, when the particle precipitation, the aurora and the current systems expand and intensify
3) the recovery phase, during wich the disturbances disappear.

The expansive phase of substorms are characterized by

a) the onset of a negative bay in magnetograms which are recorded in the auroral zone around the magnetic midnight
b) the auroral break up, which is the term for the intensity enhancement in the visual aurora, that very often is combined with a northward movement of the auroral structures and increased precipitation of particles into the atmosphere
c) the onset of a positive bay in magnetograms which are recorded in the middle latitudes at the night sector
d) Pi 2 - pulsations in time near the onset of the negative bay (Aubry, 1972).

Unfortunately different scientific groups have used different signatures to define the occurrence and time frame of substorms, and that has resulted in inconsistencies in the terminology of the substorms and the supporting events. In order to remove these problems, a summary of present views about the characteristics of substorms was published in 1980 by a teamwork of magnetospheric investigators, collected for a workshop at Victoria. In this by the Victoria workshop team suggested terminology (Rostoker et al., 1980) the term magnetospheric

substorm defines a transient process, which is initiated on the nightside of the earth and in which a significant amount of energy originating from the solar wind - magnetosphere interaction is deposited in the auroral ionosphere and in the magnetosphere. At the onset of this process, the auroral luminosity increases explosively in the midnight sector. The time scale for a magnetospheric substorm is considered to encompass the whole interval during which the auroral electrojet current increases from and returns to the background level. During this interval a sequence of intensifications of the westward electrojet may occur. Each of these is associated with a Pi 2 micropulsation burst and a westward travelling surge. As the substorm develops, a westward and poleward expansion of the region of discrete auroras in the midnight sector occurs. The start of Pi 2 bursts gives the most accurate starting time of the substorm. The whole substorm in this terminology is reduced to two phases, the expansive phase and the recovery phase. The expansive phase is an interval of time between the first Pi 2 burst and the time when the aurora reaches its maximum latitude, and the recovery phase is the time interval during which the aurora in the midnight sector returns to lower latitudes.

The term ground state for the magnetosphere is defined as a situation when the magnetosphere exhibits the lowest activity. A signature for such a low activity period is the northward direction of the interplanetary magnetic field (IMF) for a time interval, which exceeds the time constants for several substorms. Other signatures are the facts that the magnetospheric convection and the particle precipitation continue at low levels and the probability of occurrence of a substorm approaches zero.

The magnetic signature for auroral oval stations gives the relative location of the polar electro jet (PEJ) and the observing magnetometer station (see Figure 4.4). A positive (negative) Z-component indicates the observatory location to

the north (south) of the center of the westward PEJ. A positive spike in the D-component indicates the presence of auroral surges close to the observatory. Observations of significant negative H- and negative D-components without any positive spike indicate the location of the substorm onset just to the west of the observatory.

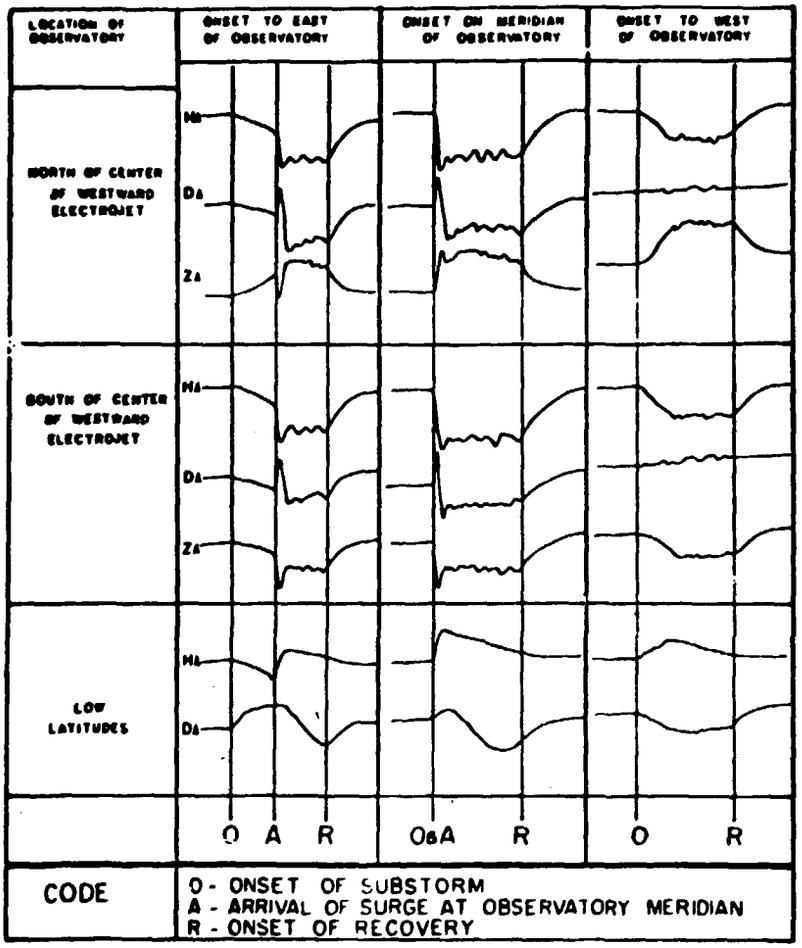

Figure 4.4 Schematic representation of magnetograms from various sites placed at different positions with respect to the high-latitude substorm current system. These synthetic records can be compared with real data to establish the position and time sequence of events for an interval of substorm activity. Typical deflections at high-latitude observatories range from around 100 to 1000 nT, while typical deflections at low-latitude stations range from a few nanoteslas to a few tens of nanoteslas (Rostoker et al., 1980).

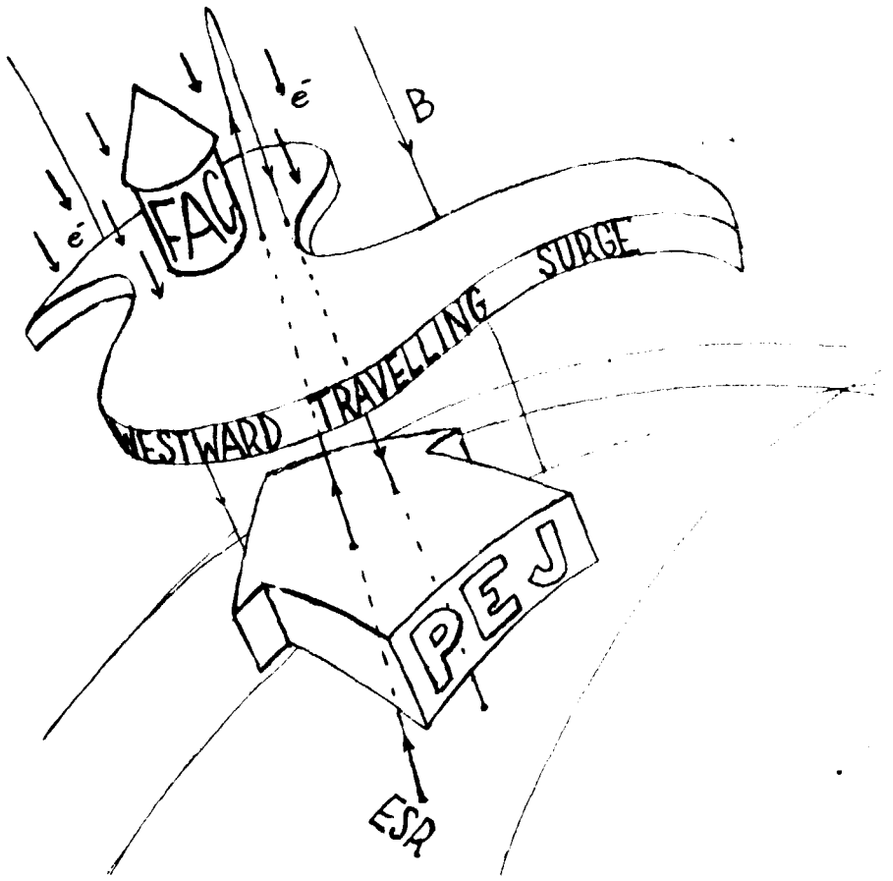

Figure 4.5 In the front of a westward travelling surge (WTS) an intense upward field-aligned current (FAC) is created by the impinging electrons.

One way to describe big variations in the magnetograms near an expanding substorm region is to establish theoretical models for a two-dimensional current system equivalent to the registrations on the magnetograms from different measuring stations on the ground. An early model for such a striking phenomenon as the auroral west-ward travelling surge (WTS) and the east- or westward directed polar electrojets (PEJ) was established by Akasofu in 1965. The very sharp transitions from a positive to a negative value around the average magnetic field H-component (Harang 1946, Heppner 1954) postulates that the region

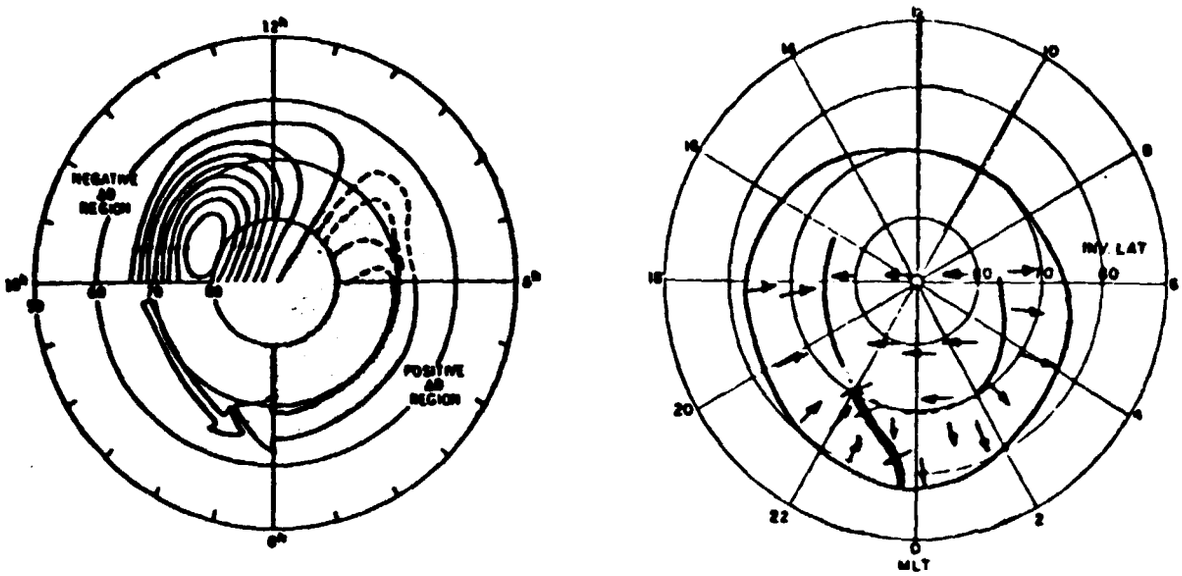

Figure 4.6 a) Current system in the ionosphere (Langel, 1974)
b) Directions of the electric field in the ionosphere (Maynard, 1974)

which is covered by WTS - aurora is to be regarded as a locally limited area of increasing auroral electron precipitation (see Figure 4.5).

Measurements of the electric field direction and intensity in the ionosphere have provided important information about the equivalent current system. Figure 4.6 b) shows the electric field directions measured by Maynard (1974). Before magnetic midnight the direction of the field is northward and eastward, after magnetic midnight it is southward and westward. This reorientation of the electric field occurs in the region of the Harang discontinuity, which is also the area where the ionospheric currents are changing from eastward to westward (Heppner, 1972) (see Figure 4.6 a)).

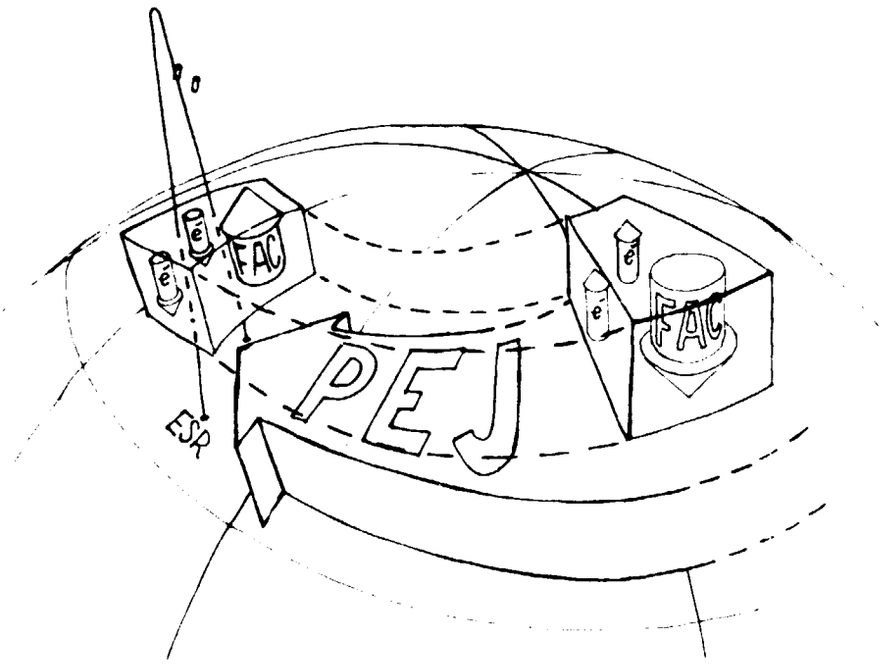

Figure 4.7 Schematic diagram of the large scale ionospheric currents, the westward directed polar electrojet (PEJ) and the field aligned currents (FAC)

Electrons impinging into the upper atmosphere are carrying an upward directed field-aligned current (FAC). This region also forms the edge and the western front of a westward directed polar electrojet (PEJ). The eastern side of this PEJ is then assumed to be a more expanded region, where the FAC is directed downward. Most likely the downward FAC is carried by an upward flow of ionospheric electrons. As a coupling mechanism between processes in the magnetosphere and the ionosphere the FAC currents are dominating. The equivalent current model limited to two dimensions are now expanded to three dimensions when, according to Figure 4.7, the two FAC are linked together from each side to the PEJ.

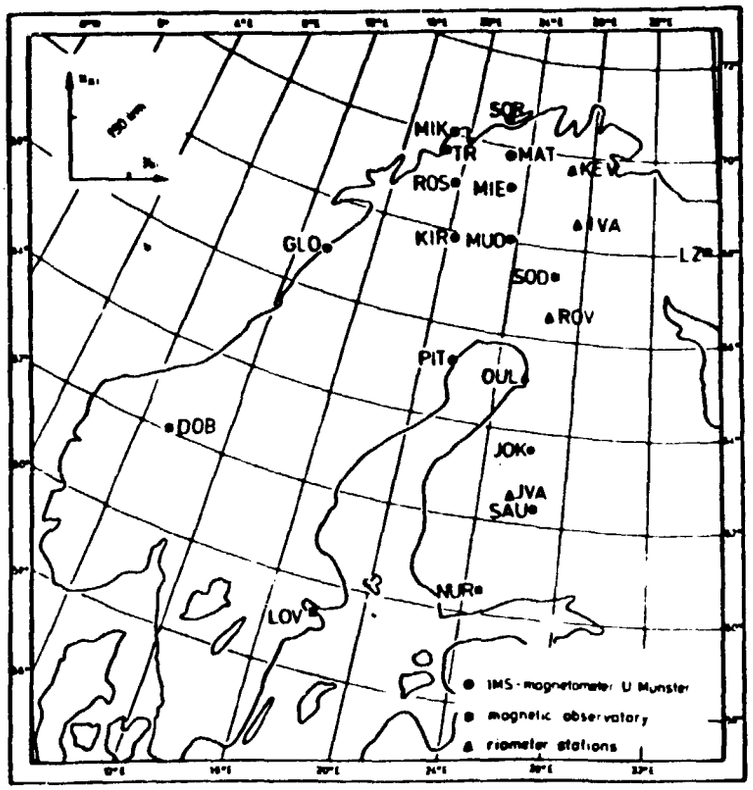

Figure 4.8 Map over magnetometer stations in the Scandinavian Magnetometer Array (SMA).

4.2 Reference and comparisons of S17-2 measurements with the results of the IMS-study

In the research work of the International Magnetospheric Study (IMS) a two-dimensional magnetometer array, called Scandinavian Magnetometer Array (SMA), was operated in Scandinavia in the period 1974--1980 (Küppers et al., 1979). One purpose of the array measurements was to interpret the local behavior of the PEJ by means of a meridian chain of magnetometers connected to other observations like recordings with all-sky cameras, photometers and riometers. The area of this magnetometer array was large enough (around 1000 x 1000 km^2) to cover a good portion of the entire substorm onset phenomena.

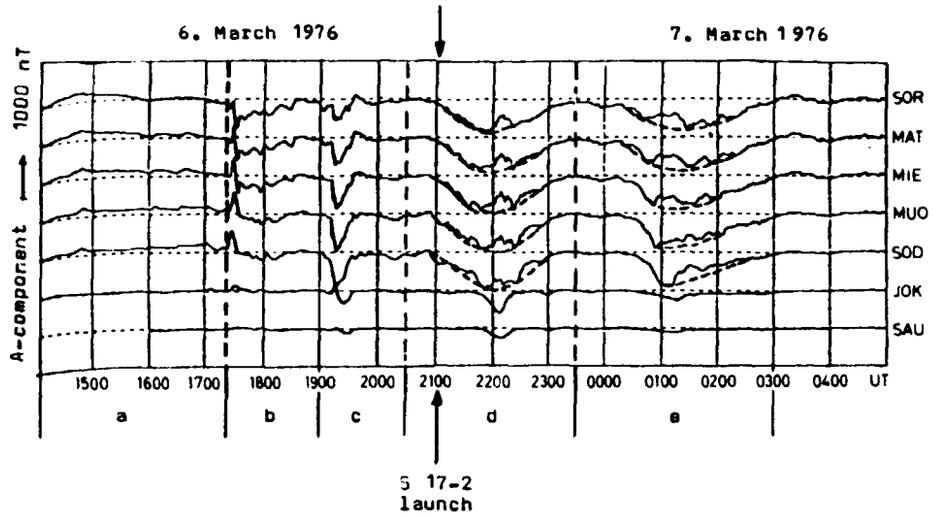

Figure 4.9 Variations of the A(H)-component in the magnetograms from the profile 4 of the Scandinavian Magnetometer Array (König, priv.com., 1979). (Profile 4 included the magnetometer stations SOR, MAT, MIE, MUO, SOD, JOK and SAU according to Figure 4.8).

At the time of launching of the S17-2 payload a part of the SMA-magnetometer net-work was ready for registrations. A group from the university of Münster (FRG) has used data from two north-south profiles of 14 magnetometer stations (see Figure 4.8) in the study of a substorm event around the S17-2 launch time. The purpose was to establish a picture of the current system during this magnetospheric substorm corresponding to the ionospheric situation. In the technique used the first step is an analysis of the magnetograms to get the local development of the magnetospheric disturbances in a specific substorm (see Figure 4.9). The magnetic as well as the auroral data presented were transformed to a special cartesian coordinatesystem, X_{KI}, Y_{KI}, centered at a point in a tangent plane at this point (Kiruna). The horizontal components H and D are rotated to A and B respectively, the Z-component is unchanged. Besides providing a more physical picture, this

transformation reduces the geometrical effects and gives the possibility to direct comparison of data from different magnetometer stations (Opgenoorth et al., 1980).

In order to separate quiet time current systems from substorm connected ones and to classify the changes in the existing currents, a special method called differential equivalent current vectors (DEC) was used. In this method, a stable magnetic situation is assumed at the observation time t_1 and the situation at the time t_2 is given by the superposition of the change of the magnetic field. In most cases other data (e.g. optical observations) give restrictions or complements to the various possible causes to a specific current pattern. This analysis together with that of other data e.g. Kp- and AE-index (see Figure 4.10) for this period gave the picture of a relatively strong disturbance period from around 17.25 UT on 6 March to around 03.00 UT on 7 March. The A(H)-component shows a disturbance of 1000 nT, the B(D)-component 500 nT and the Z-component is turning between +400 nT and -400 nT.

The gross-scale disturbance is separated in five periods marked in Figure 4.9 by dashed vertical lines. The analysis for the period a) between 14.00 - 17.25 UT points to an eastward directed PEJ over northern Scandinavia. At the end of this period a turning of this eastward PEJ is started around 17.00 UT, caused by the onset of a magnetospheric substorm situated east from the Münster magnetometer array. The next period labelled b) in Figure 4.9 is characterized by the sharp positive spike in the H-component followed by a broad negative bay implying that the westward PEJ is now dominating over a wide region; the sharp spike marks the location of the Harang discontinuity. 17.30 UT seems to be rather early for the occurrence of the Harang discontinuity, but in very disturbed conditions the Harang discontinuity region is displaced towards dusk. Later it goes towards the midnight sector and is even displaced in southward direction. Figure 4.11 shows the typical equivalent current situation for this period.

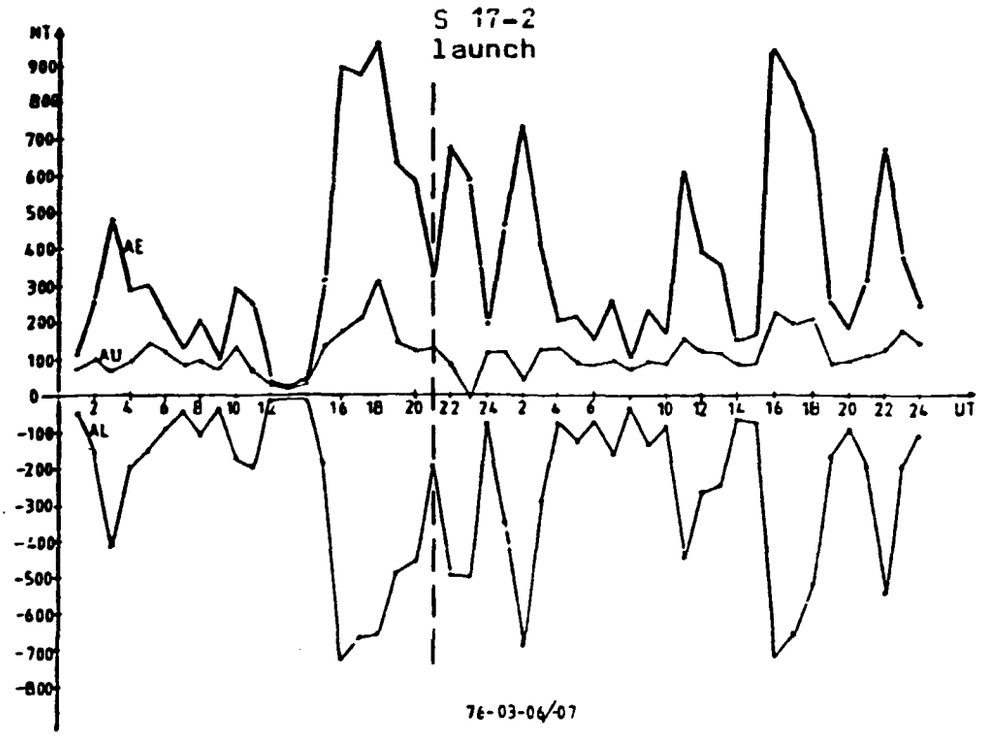

Figure 4.10 AE-, AU- and AL-indices for the period 6 March - 7 March in 1976.

The next period, labelled c) in Figure 4.9, is characterized by the sharp negative bay in the H-component (and its recovery in a relatively short time; <1h) is characteristic for a substorm bay (Kostoker, 1969).

In the period d) a new substorm onset is recorded in both the magnetometer array profiles around 21.00 UT with recordings of the substorm related phenomena like riometer absorptions, WTS and westward PEJ. Typical for the expansive phase is an intensification of the PEJ, an "afterglow" of the aurora e.g.

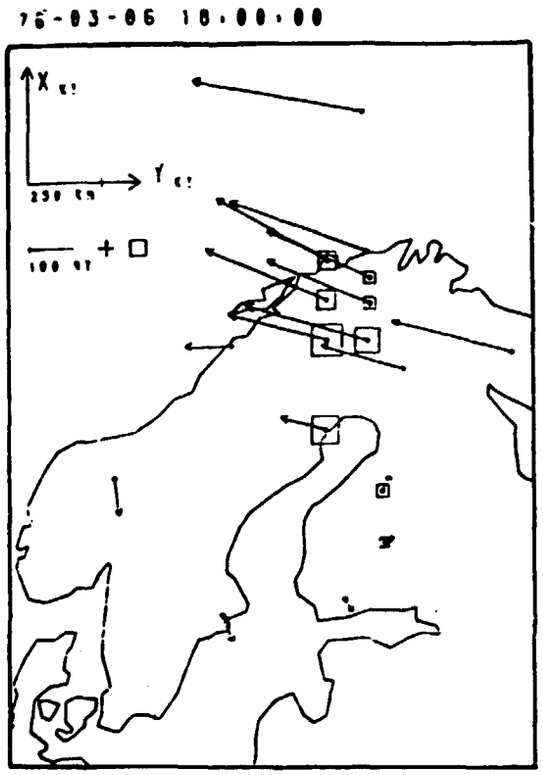

Figure 4.11 The equivalent current situation for the period labelled d) in Figure 4.9. The vertical components are indicated by the size of the station symbol, □ = negative, + = positive (Baumjohann, priv. com., 1978).

a decrease of the auroral brightness, often combined with a slow southward drift of these diffuse auroral forms. The latter part of this period is interpreted as the recovery phase of a substorm. However, during this recovery a short period with a positive H-disturbance indicates that a second substorm may have been superimposed on the first one. This means that two substorms can overlap.

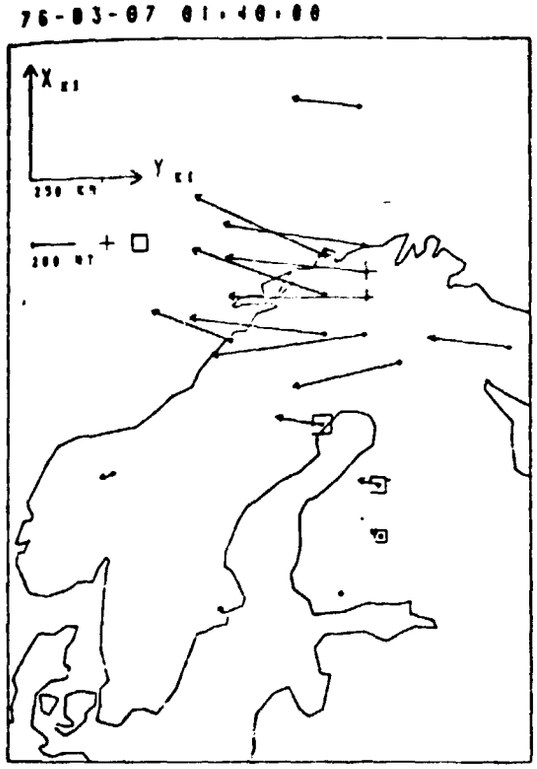

Figure 4.12 The equivalent current situation for the period labelled e) in Figure 4.9 (Baumjohann, priv. com., 1978).

The westward PEJ still dominates the next period (see Figure 4.12) but later it decreases in intensity poleward and increases equatorward. Morning aurora, e.g. pulsating, diffuse auroral spots are observed in this period (period e) in Figure 4.9) and around 04.00 UT the magnetic stations in the array show only weak magnetic disturbances.

Above we have described a two-dimensional, equivalent current system of Chapman and Vestine type, based on recordings from ground based magnetometers. A method to expand the current system to three dimensions is shown in Figure 4.13 (Fukushima, 1976). The method is based on the fact that a counterclockwise current curl indicates an upward directed field-aligned current, while a clockwise current curl indicates a downgoing FAC.

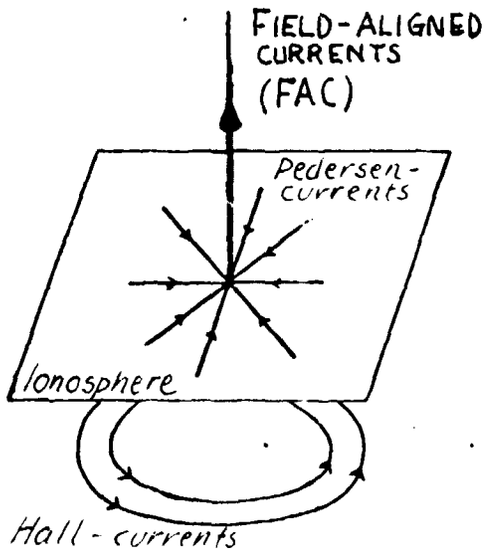

Figure 4.13

Current directions associated with field-aligned currents (Fukushima, 1976).

Figure 4.14 shows the calculated equivalent current vectors for a time interval of 5 minutes during the period b). These current vectors are determined from the original magnetograms of the two profiles in the SMA-array.

In the magnetograms a shortperiodic disturbance is supposed to be superimposed upon a disturbance of a longer period. The rate of the former disturbance is calculated and represented in the diagrams of the equivalent current vectors in the Figure 4.15. A development of a curved current structure is evident during these five minutes through the succesive reorientation of the vector directions as seen in Figure 4.15. Figure 4.16 shows the determination of the center of these current curls. The average positions of the centra for all the equivalent current vectors in this time interval give the location of the upward field-aligned current, that has caused the magnetic field disturbances (Fukushima, 1976). In such a way an extension of the horizontal current pattern with a vertically directed current can be made through analysis of only ground based magnetometers (see Figure 4.17) when the horizontal cross section of the field-aligned current region is small.

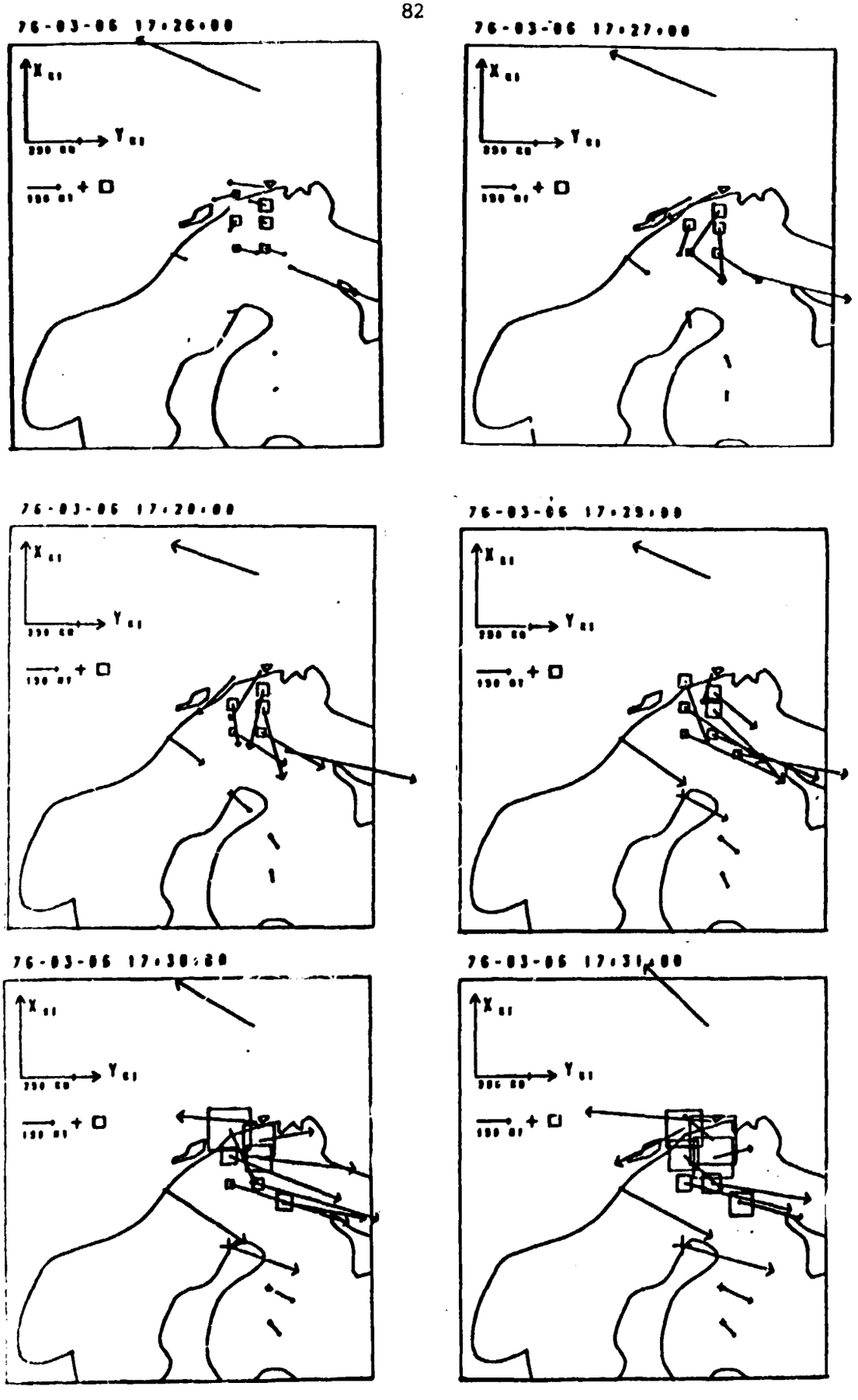

Figure 4.14 Equivalent current vectors for the time interval 76.03.06, 17.26 - 17.31 UT (König, priv. com., 1979).

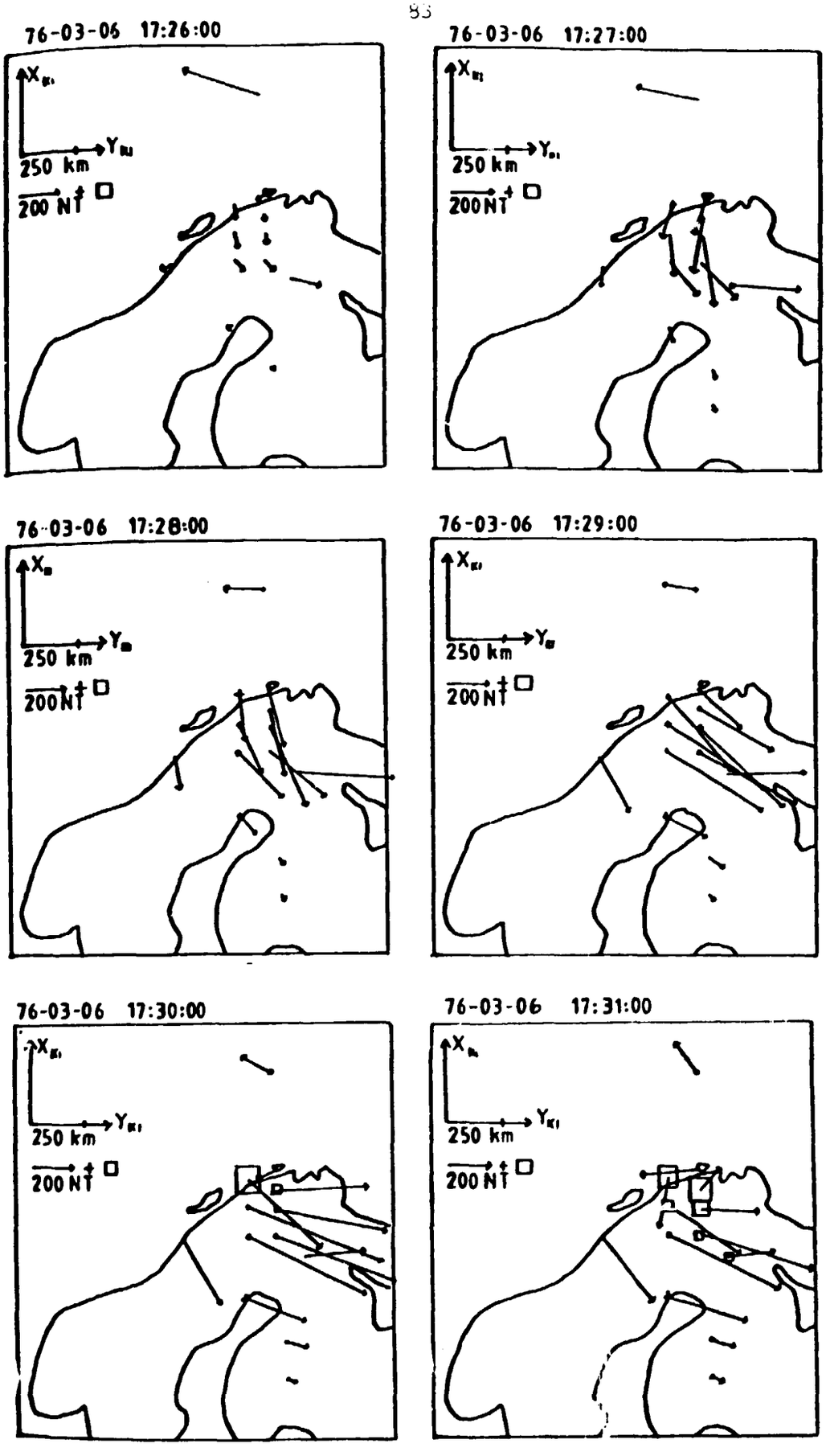

Figure 4.15 Equivalent current vectors for a superimposed magnetic disturbance for the time interval referred into Figure 4.14 (König, priv. com., 1979).

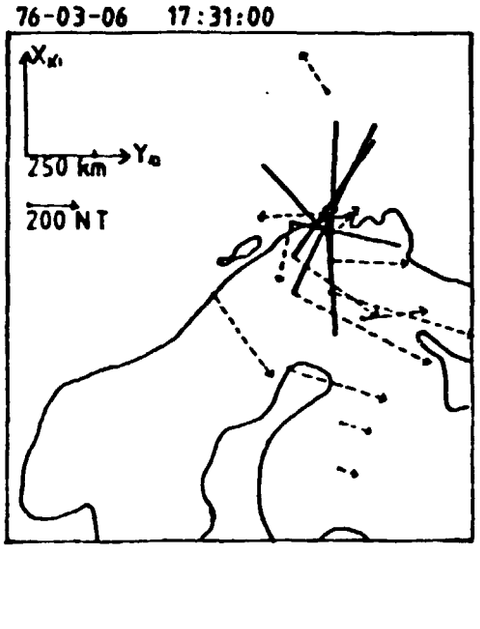

Figure 4.16

Determination of the center of the equivalent current curl structure. The dashed lines are the equivalent current vectors and the solid lines are their perpendiculars (König, priv. com., 1979).

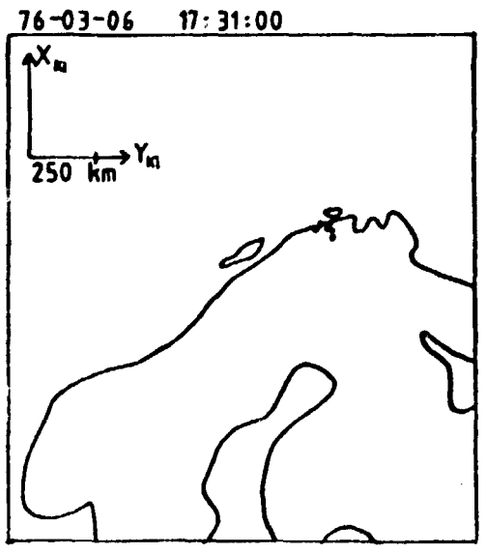

Figure 4.17

The crossing points between the lines perpendicular to the current vectors give the location of the field-aligned current (Fukushima, 1976; König, priv. com., 1979).

As we have mentioned previously in Chapter 1.2 electric fields were measured during the S17-2 rocket flight. This was made by the Royal Institute of Technology (RIT) onboard the mother payload by means of four spherical electric probes mounted on two pairs of deployable booms of 1.5 m length (see Figure 1.1). Every 10 s these probes work as Langmuir-probes to probe the surrounding plasma. Fahlesson describes measurements with

such types of probes and points out effects that can occur in the measurements (Fahlesson. 1969). Due to a boom deployment failure only two of the four probes provided useful data, but in spite of that the electric field could be calculated in two perpendicular directions. Figure 4.18 shows the electric field data during the whole flight and in Figure 4.19 the calculated number density of electrons versus flight time of the rocket is presented.

The electric field is given in an Earth-fixed frame of reference with the z-axis directed upwards along the magnetic field. The x-axis is chosen so that the tangent to the great-circle through the magnetic (dipole) pole lies in the

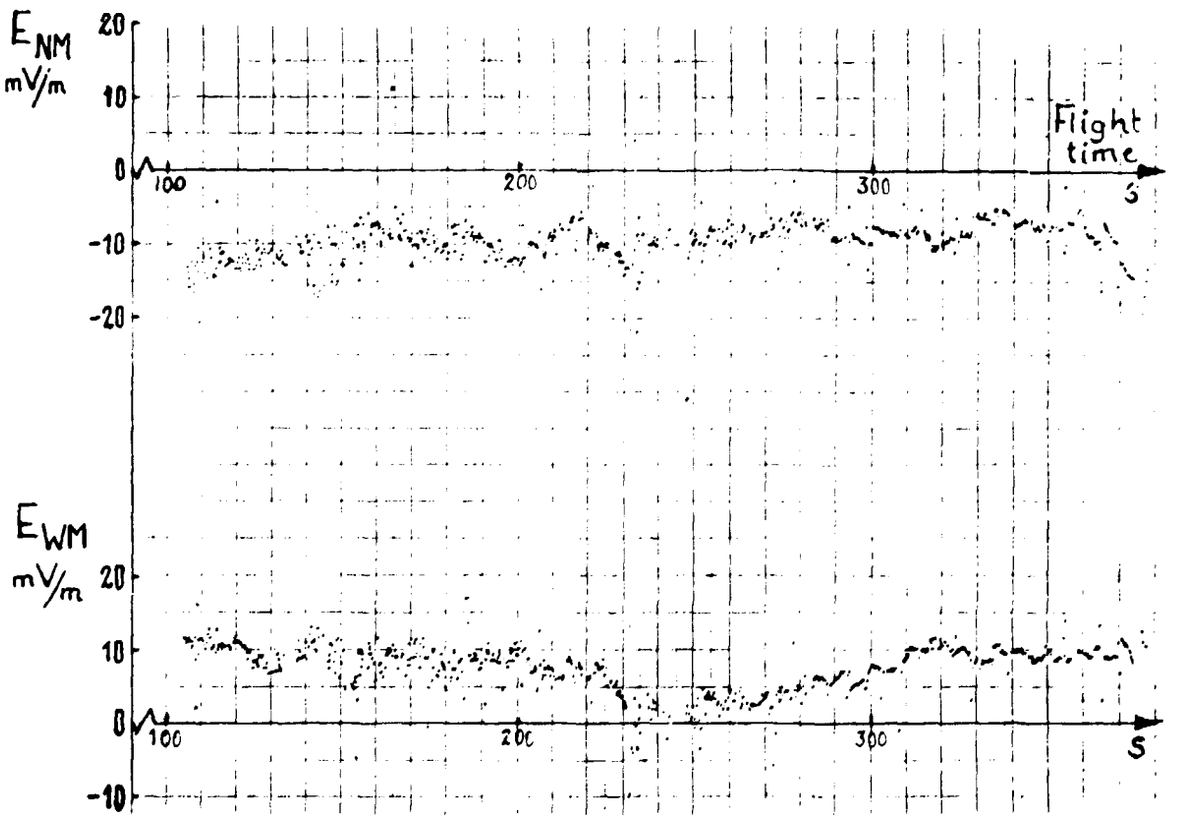

Figure 4.18 The two electric field components E_{NM} and E_{WM} measured during the S17-2 flight (Fahlesson, priv. com., 1978).

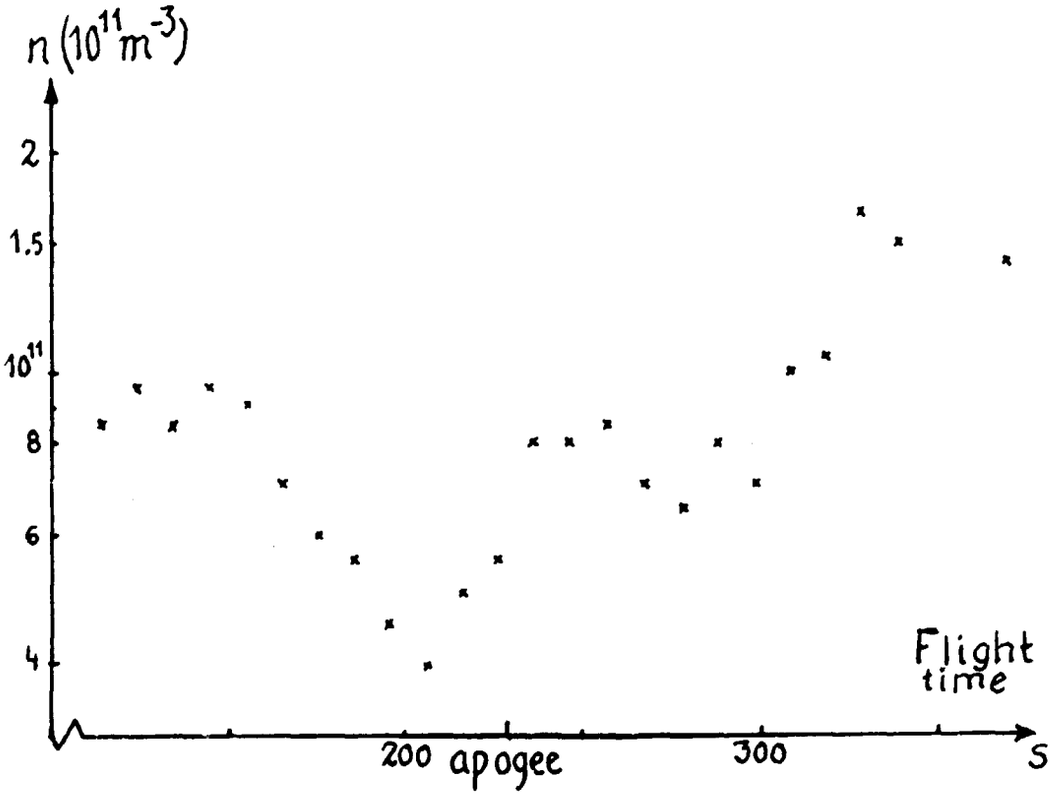

Figure 4.19 The calculated electron number density versus the flight time of S17-2 (Fahlesson, priv. com., 1978).

xz-plane. This direction (index NM) points about 27 degrees west of geographic north and the y-component (index WM) points about 27 degrees south of geographic west (Fahlesson, priv. com., 1978).

These registrations of the electric field show an abrupt change of the E_{WM} component fr around 10 mV/m to a slightly negative value at a flight time of 230 s. After this sudden decrease to negative values the field component E_{WM} increases rather slowly and after about 10 s it returns to the value it had previously. The "x-component", marked E_{NM}, stays relatively stable at a value around 10 mV/m during the whole measuring period.

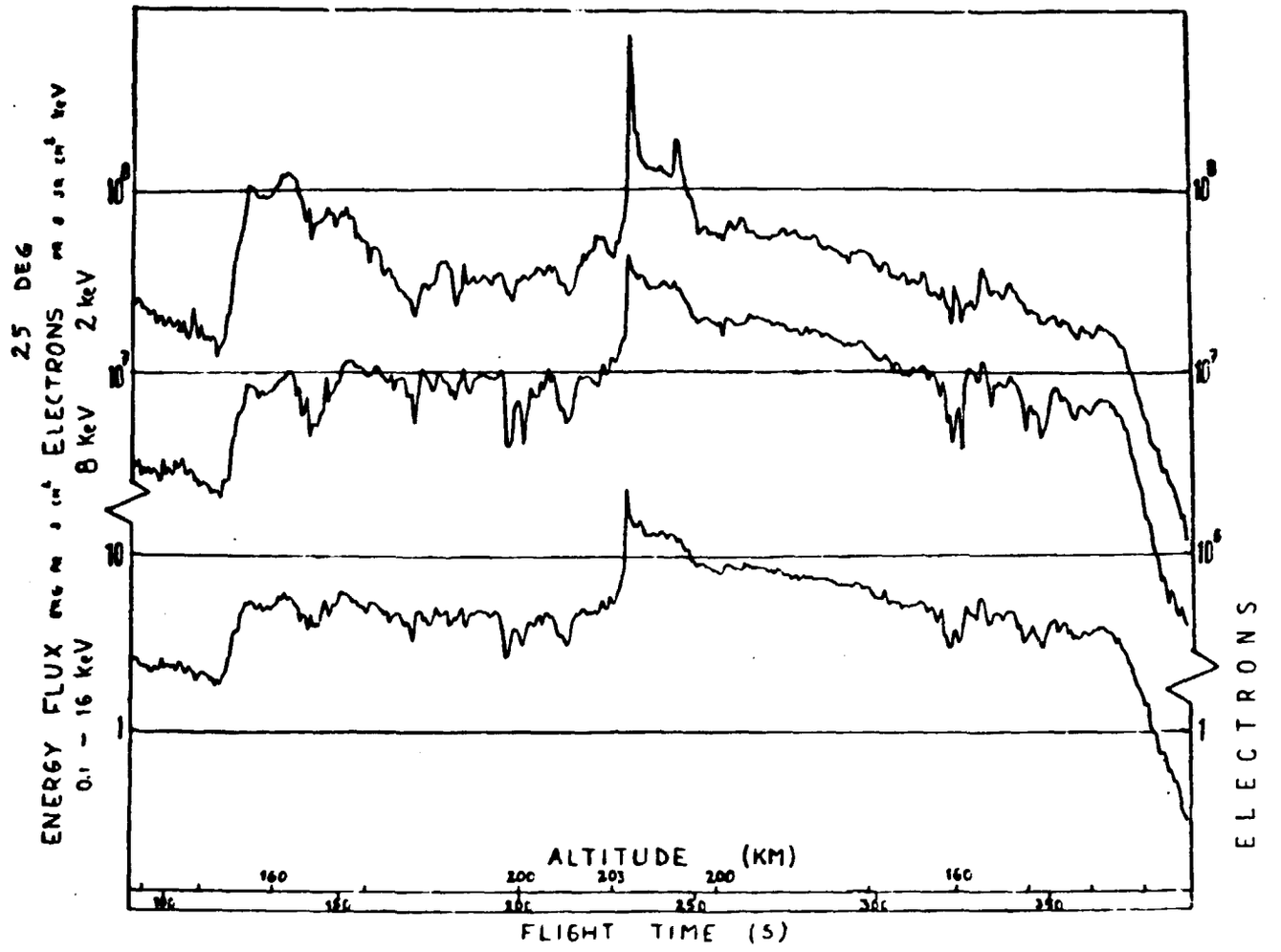

Figure 4.20 The electron fluxes at 8 keV and 2 keV and the total electron energy flux in the range 0.1-16 keV as a function of the altitude and flight time of S17-2.

Figure 4.20 depicts the energy flux of electrons over the energy range 0.1-16 keV and the differential electron flux at 8 and 2 keV versus flight time. The fluxes are averaged over 0.6 s. From this diagram and from Figure 4.18 we find a good anticorrelation between particle fluxes and the E_{WM} component of the electric field. Around 21.04 UT, about 250 s after launch a very sharp flux increase occurred. The 2 keV electron flux increased with a factor of 10 and the 8 keV electron channel and the integrated total energy increased fivefold.

The very rapid flux increase (within a few seconds) is followed by a fairly sharp decrease after a few seconds to about half of the peak flux. After that it decays relatively slowly to its "background" flux value (within about 40 s). An ionospheric situation that agrees with the ground based magnetic observations for the time 21.02 - 21.06 UT, is that of a very stable westward electrojet with disturbance of the X-component down to approximately -300 nT (see Figure 4.21). Consequently the electric field should be stable during the period. However, the electric field and the particle precipitation do really show a transcient event. The south-ward directed component of the size 10-15 mV/m remains stable, but the westward electric field component drops to zero (from an average size of about 5 mV/m) and the electron number density increases due to a local burst of precipitating electrons.

Around 21.00 UT the start of the negative bay occurs in the X-component implying that the S17-2 rocket was launched in the expansive phase of the substorm. All-sky pictures from Esrange show a break up at 20.57 UT, but after 21.00 UT the situation is changed to a more faint and diffuse aurora. Earlier measurements (De La Beaujardiere et al., 1977) have shown that a change in the direction of the east-west electric field component is associated with discrete auroral forms. All-sky pictures from Esrange for the period 21.03-21.06 UT do not show any discrete aurora at the position of the rocket, but around 50 km further north a very broad but weak east-west directed diffuse aurora was seen. Visible aurora is frequently associated with a peaked differential energy spectrum (see e.g. Lundin, 1976 and Lui et al., 1977). As seen in Figure 4.22 the energy spectra in the S17-2 data are not peaked. At the time of enhanced fluxes the predominant enhancements occurred at lower energies.

The sudden changes in the electric field and the electron number density data can be understood as due to the observed enhanced precipitation of electrons into the ionosphere.

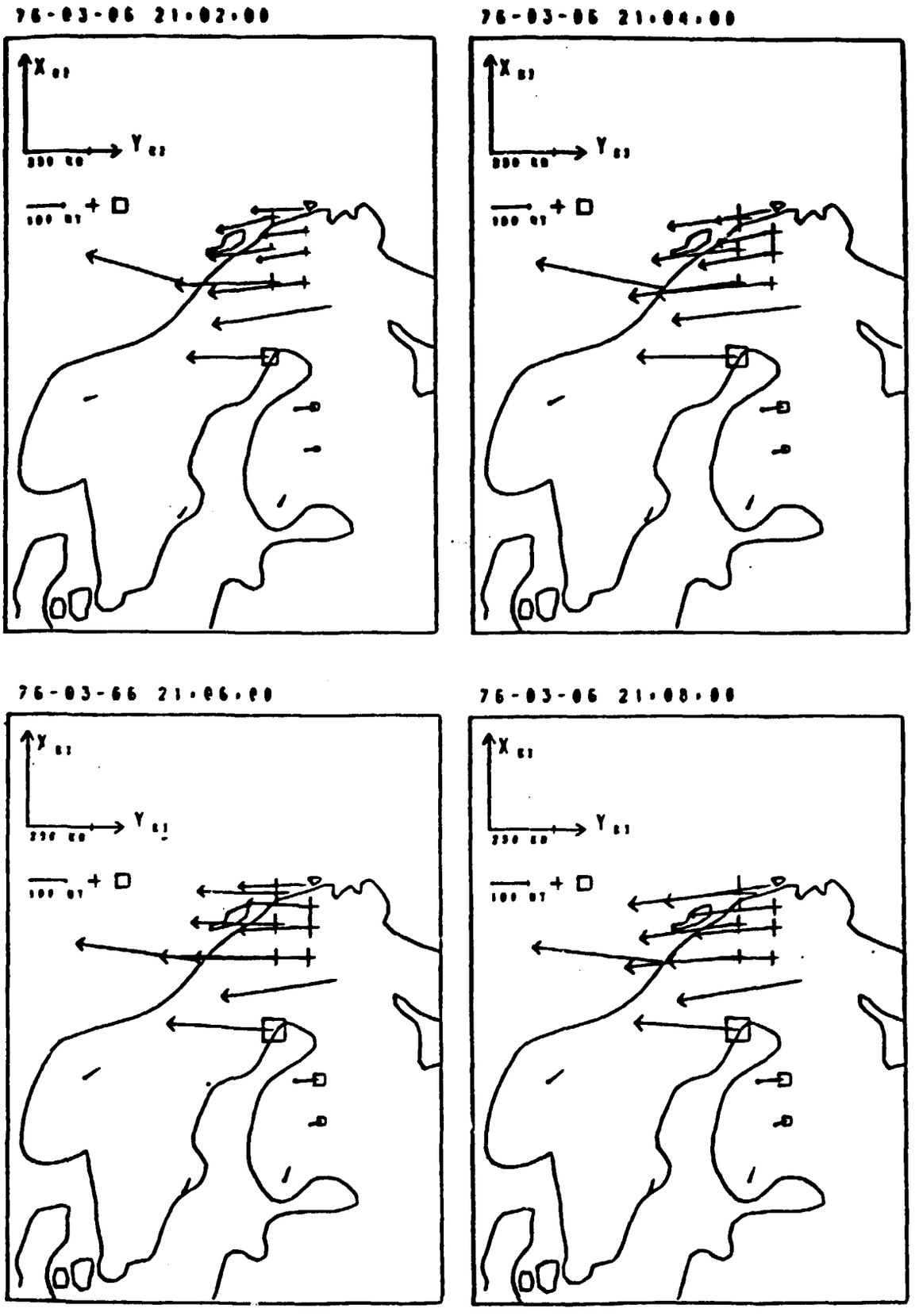

Figure 4.21 The equivalent current vectors show for this period a very stable westward directed current pattern over the whole range of the Scandinavian Magnetometer Array (König, priv. com., 1979).

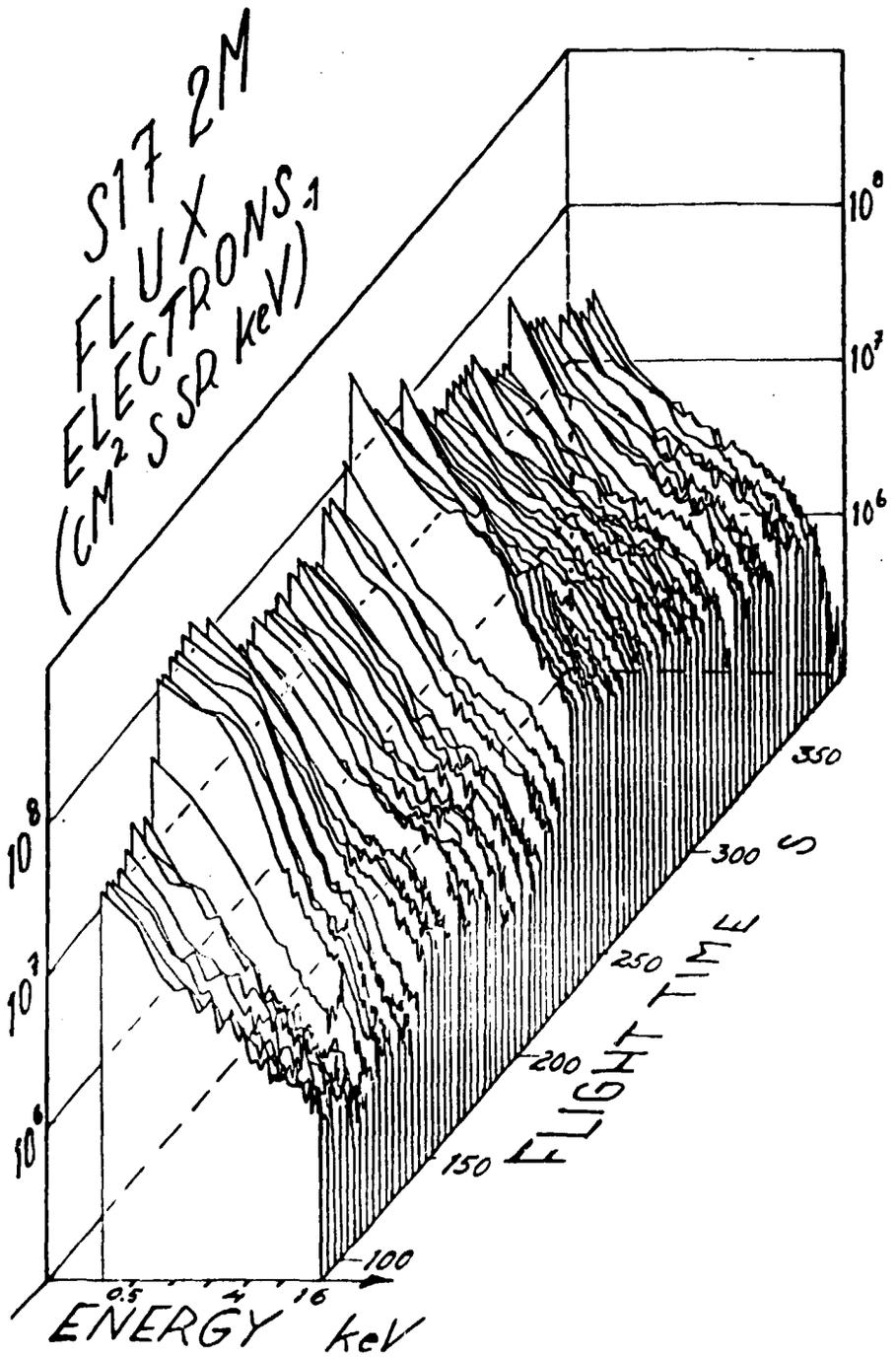

Figure 4.22 Energy spectrum as a function of the rocket S17-2 flight time measured with the swept CEM-detector pointing along the rocket spin axis (see Figure 1.4 and Table 2.1).

The partial lack of agreement with other parameters may be understood as a consequence of the geometrically very strong limitation of the precipitation region. The rocket S17-2 intersected a region of a horizontal width of 6 km during the time when the enhancement of the precipitating electrons was recorded and the temporal intensity variations were limited to a local region of the same order of size, which the ground based magnetometer array was not capable of resolving.

4.3 Comparison of simultaneous particle observations at low ionospheric altitude (S17-1) and at the magnetic equatorial region (ATS-6)

On the nightside the auroral electrons are supposed to originate in the plasma sheet. Simultaneous conjugate observations at low ionospheric altitudes and in the equatorial plane are needed to demonstrate relations between aurora and plasma sheet phenomena. Observations of that kind have been made earlier by e.g. Choy et al., (1971), who compared data from a rocket flight and a satellite, Eather et al. (1976), who conducted a study of the energy flux observed by ground photometers (keograms) and by particle detectors onboard a satellite in geostationary orbit, and by Meng, (1979) and Zanetti et al., (1980), who compared particle spectra from two satellites. The Application Technology Satellite 6 (ATS-6) was launched into a geosynchronous orbit at an altitude of 6.63 R_E and this satellite was operating at the time of the S17-1 launch. Thus, this flight offered an opportunity to compare rocket observations of precipitating electron fluxes with the fluxes of electrons measured near the geomagnetic equatorial plane in the geostationary orbit. For this study particle data in the plasma sheet have been obtained from the University of California, San Diego (UCSD) auroral particle experiment consisting of electrostatic analyzers (courtesy of R. Lundin). Only those of trapped fluxes from a north-south sweeping particle detector is, however, used in this report.

The detector provided fluxes of both ions and electrons over an energy range of 1 eV to 80 keV with an energy resolution of about 20%. The whole energy scan consisted of 64 steps and was covered in 16 s. The particle information received from UCSD was tabulated data of the distribution functions f(E) of trapped plasma sheet electrons and ions in units of $s^3\ km^{-6}$.

$$f(E) = j(E)/E \cdot k \quad [s^3\ km^{-6}]$$

from which we derived

$$j(E) = f(E)\ E \cdot k \quad [\text{part. } cm^{-2}s^{-1}sr^{-1}eV^{-1}]$$

where $k_{electrons} = 6.187$

$$k_{ions} = 1.836 \cdot 10^{-6}$$

An uncertainty in these comparative measurements is the determination of the position of the vehicles. A simple explanation to a lack of correspondence between the particle fluxes from the low altitude rocket measurements and those from the equatorial plane could be that the two measurements were made on different flux tubes in a region with strong horizontal gradients. By using existing global magnetic field models the foot point of a magnetic field line through the satellite position at the equatorial plane can be derived at the rocket altitude. A widely used such field model is the International Geomagnetic Reference Field (IGRF).

This model has been recommended by the International Association of Geomagnetism and Aeronomy (IAGA) to be used in the period 1975--1980. In this report the IGFR coefficients of the year 1975 were used in a computer program (courtesy of G. Gustavsson) which integrated the magnetic field line from the ATS-6 position and calculated the longitude and latitude of the foot point.

A diurnal variation of the field line foot point is due to the solar wind compression of the magnetosphere at the dayside and

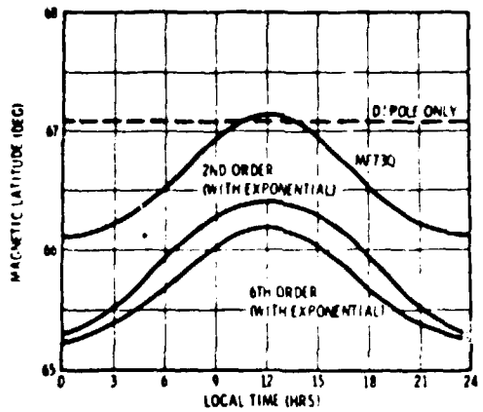

Figure 4.23

Diurnal variations of the foot point of the geomagnetic field line at the geosynchronous orbit for different field models. Reproduced from Olson and Pfitzer (1974).

the nightside inflation of the geomagnetic field. This approximately one degree diurnal variation is not taken into account in our discussion (see Figure 4.23 after Olson and Pfitzer, 1974). An equal shift of the same order of magnitude of the ATS-6 field line foot print is attributed to the effect of geomagnetic activity. When the geomagnetic conditions are disturbed the foot point moves further south. For the disturbance level at the time of the S17-1 flight the ATS-6 field line was expected to have its foot point south of the S17-1 rocket position.

Observations have shown that with increasing Kp the foot point of a magnetic field line moves equatorward but the poleward edge of the auroral region moves poleward. The reason for this poleward expansion of the auroral region during disturbed magnetic conditions is not yet well understood; some investigators (e.g. Eather et al., 1976; Akasofu, 1978) argue that a poleward expansion of the aurora is coupled to an outward equatorial plasma drift. Even opposite ideas have been presented (Vasyliunas, 1970). Through a streching of the magnetic field lines an inward equatorial plasma motion should be coupled to a depression in latitude of the field line foot print and to the pole-ward expansion of the aurora.

Figure 4.24 and Figure 4.25 show energy-time spectrograms obtained from the north-south scanning detector onboard the ATS-6. The first appearence of the soft plasma sheet particle occurs at approximately 16.00 UT (Figure 4.24). Later very

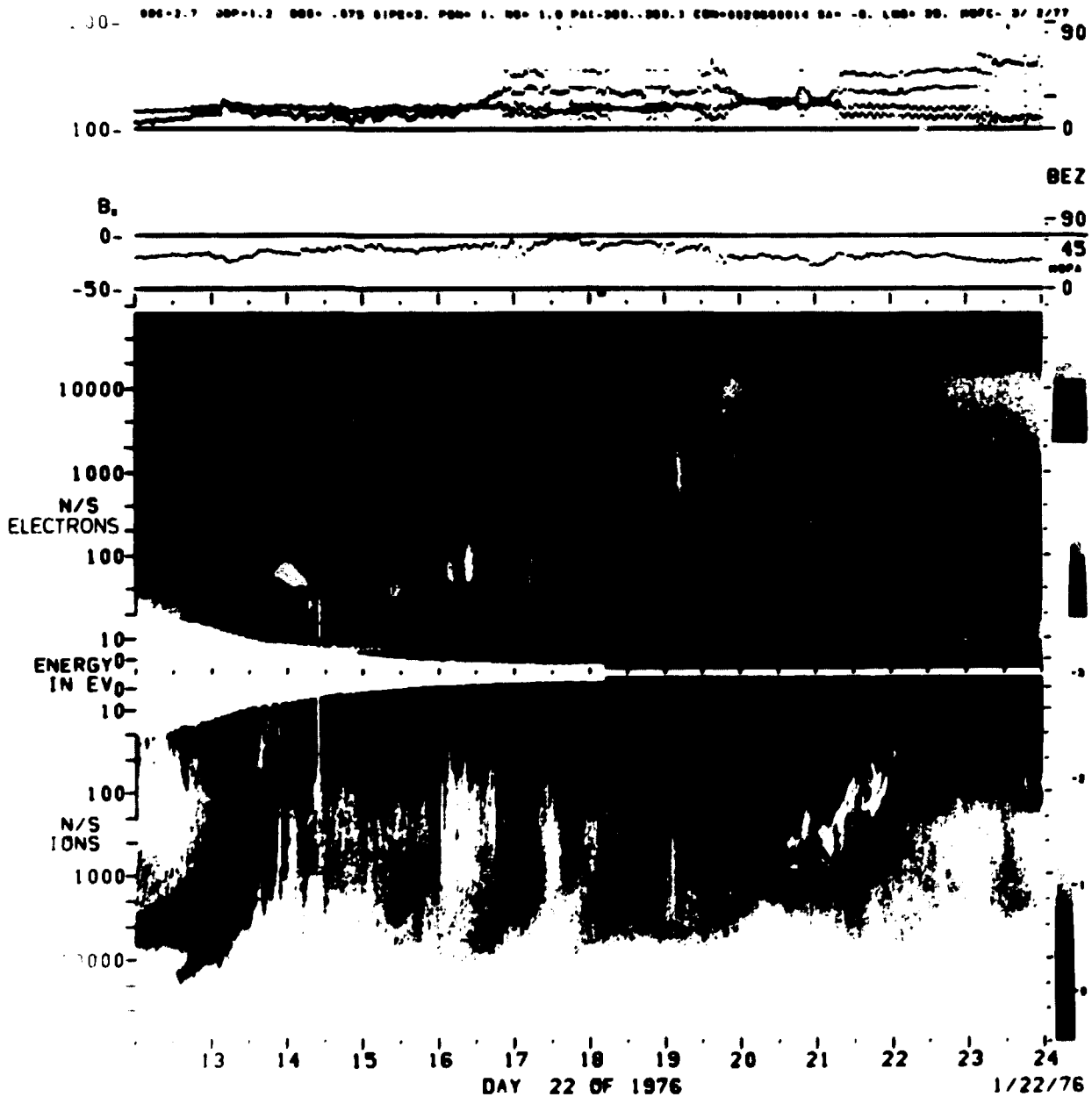

Figure 4.24 The ATS-6 "E-t"-spectrogram representing the general trapped plasma particle characteristics at the geosynchronous altitude.

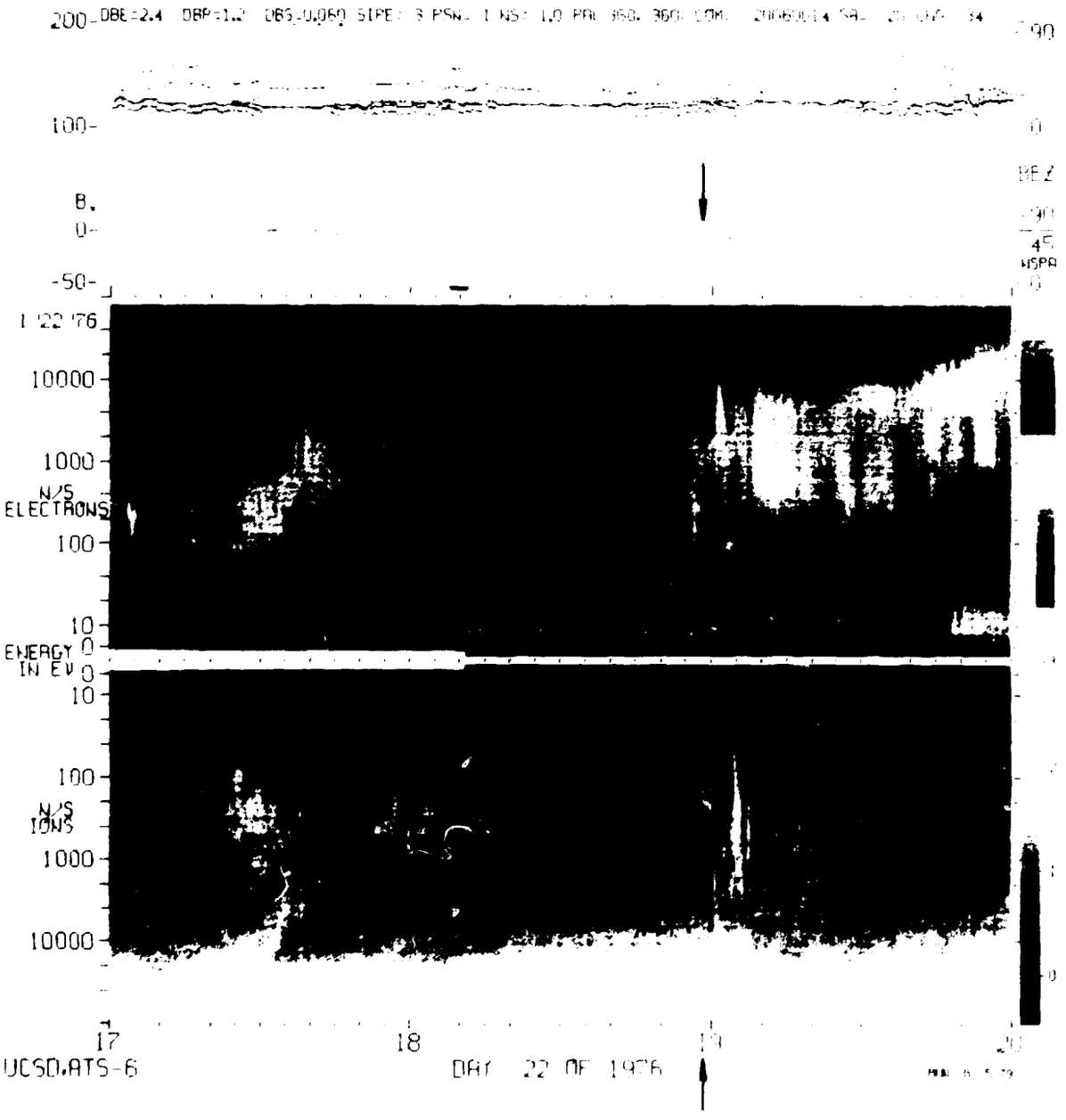

Figure 4.25 "E-t"- spectrogram of the ATS-6 particle measurements. S17-1 launch is marked with arrows.

significant enhanced fluxes of plasma sheet electrons are very clear and dominate the spectrogram and remain rather stable from approximately 19.00 UT (S17-1 launch 18.58.36 UT). The vertical striations in the ATS-6 "E-t"-spectrograms are results of the mechanical scanning of the detectors. In the actual auroral display during the measuring phase small scale changings could be seen. These consisted of several east-west oriented auroral arcs, which moved northward during the time of measurement. This is evident in the series of the selected pictures from the TV-film recorded at Rappsåive during the S17-1 flight (see Figures 3.9 and 3.10).

Although the rocket had a northward trajectory the northward velocity component of the rocket payload was much less than the velocity of the poleward expansion of the aurora. The ATS-6 particle detectors were measuring in a region which was geomagnetically conjugate to regions south of the auroral structures, while the rocket instruments measured roughly the whole time interval fully within weak diffuse auroral structure. In the time interval 16.00-20.00 UT in which the S17-1 rocket flight occurred, the ATS-6 spectra showed a successive hardening. The low energy part of the electron fluxes showed a significant decrease, which was most evident at 19.00 UT, at the same time as discrete auroral structures started to move northward and an auroral arc changed to a more smeared out and diffuse display. The hardening of the ATS-6 electron spectra is illustrated in Figures 4.26 and 4.27 and is also evident in the S17-1 spectra.

A substorm injection of plasma in the equatorial region caused the increasing of the high energy particles. This temporal variation of the particle precipitation at the equator cooperated with the accumulation of ionospheric low energy particles at the auroral region. Energy spectra from the satellite position and the rocket altitude did not show full consistency due to the fact that the two measurements were located at different field lines and due to acceleration processes along the particle paths.

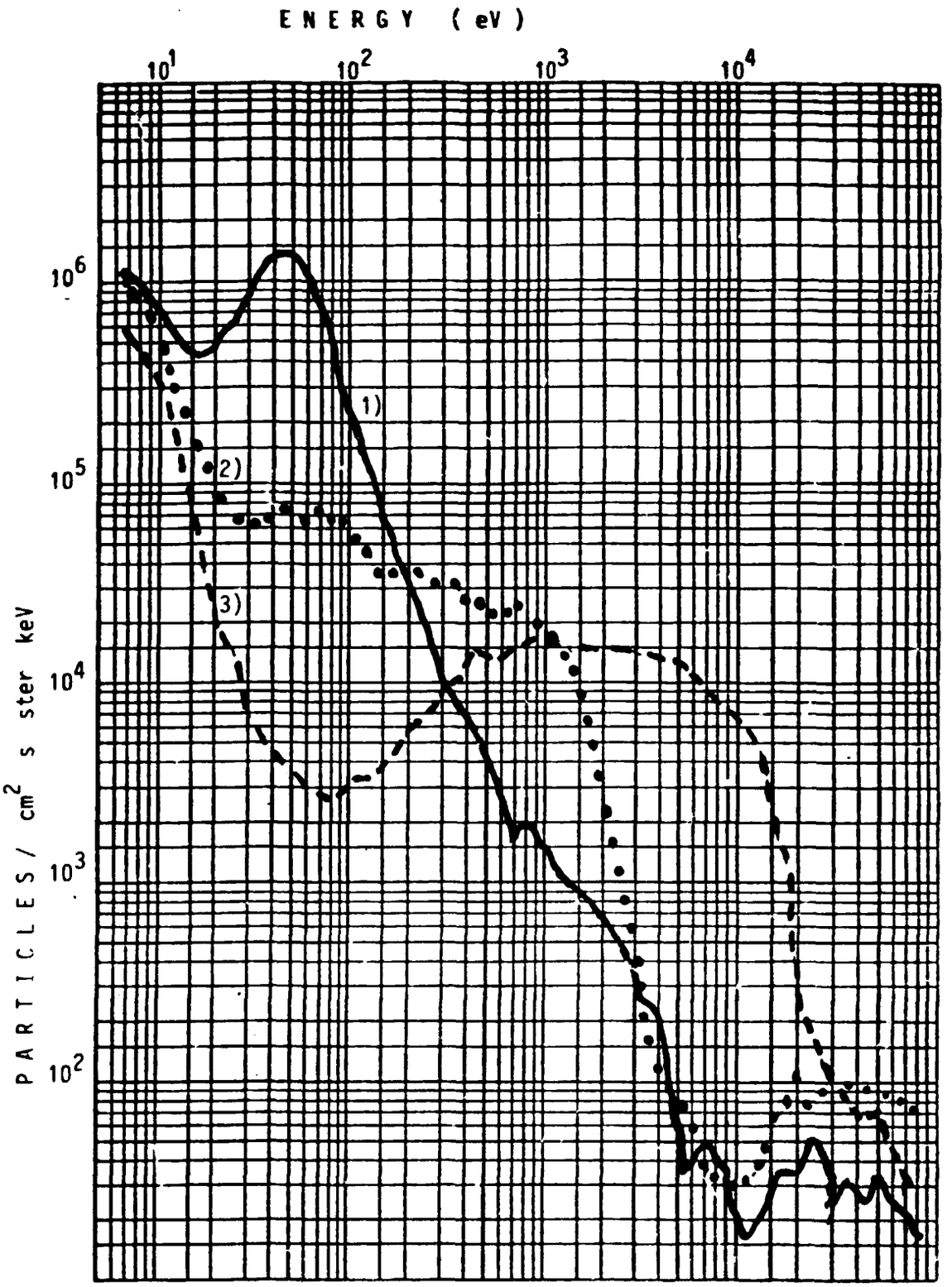

Figure 4.26 Three ATS-6 spectra of precipitating electrons selected to illustrate how the low energy electron flux decreases and the flux of higher energy electrons increases. Averges of 16 s intervals.

1) 16.11.30 - 16.11.46 UT ————————
2) 18.57.50 - 18.58.06 UT .....
3) 19.01.26 - 19.01.42 UT – – – – – – – –

Figure 4.27 Particle spectra obtained from the ATS-6 satellite illustrating the hardening of the flux of electrons during the S17-1 rocket flight (S17-1 launch: 18.58.36 UT).

4.4 Summary and conclusions

The Swedish sounding rocket S 17-2 was launched in the expansive phase of a magnetic substorm which was one in a series of consecutive substorms. The corresponding ionospheric disturbance was studied by means of data from a ground based magnetometer array and in situ measurements of electric fields and particles from the rocket. A very strong westward directed electrojet prevailed in the ionsophere during the rocket flight. At the rocket altitude the southward directed electric field component showed values in the 10-15 mV/m range and the westward directed component had an average value of about 5 mV/m.

These results agree with earlier measurements by Doupnik et al. (1972), De La Beaujardiere et al. (1977) and Horwitz et al. (1978). All these measurements have shown for comparable disturbances a southwest directed electric field. A special study by Mozer and Lucht (1974) has shown that the southward directed component is three times greater than the westward directed electric field component. This is in agreement with the S17-2 results.

The very distinct change in the electric field direction associated with the strong flux enhancement near apogee was an interesting feature. De La Beaujardiere et al. (1977) have observed similar electric field reversals in discrete auroral displays. All-sky films exposed at Esrange for the actual S17-2 period did not show any visible aurora in the rocket position. About 50-100 km further northward from Esrange some very weak and diffuse auroral arcs could be seen. Most likely this sudden change in the electric field direction is spatially strongly limited as the field already after some 40 s returned to the earlier direction. A more accurate confirmation of the size of this spatial region is not possible to find out from the S17-2 measurements, due to the fact that the electric field was measured only at one point (mother payload). Probably an enhancement of a spatially limited precipitation of energetic particles can explain the short and

locally limited electric field change. Jones (1976) has argued for a minimum energy for the particles to create visible aurora. This agrees with S17-2 measurements of enhanced fluxes mostly at low particle energies (see Figure 4.22). According to Lui et al. (1977) and also many other investigators discrete auroral forms are predominantly associated with peaked electron spectra. The lack of such peaks in S17-2 spectra is in agreement with the lack of discrete aurora on the magnetic field lines traversed by the rocket. The rocket S17-2 intersected a region with a horizontal width of 6 km during the time of the electron flux enhancement (at a flight time 220-270 s). Thus, the temporal intensity variations are limited to a local region of the same size. The ground based magnetometer array could not detect current structures of this size. The geosynchronous ATS-6 satellite measured the plasma sheet particles near the magnetopsheric equator simultaneously with the detection of the conjugate precipitating auroral particles by the sounding rocket S17-1. Direct qualitative comparisons of particle energy fluxes from the two measurements showed that the fluxes were generally higher at the auroral region than at the equator, which suggested that an acceleration mechanism along the particle paths occurred. The diurnal variation of the location of the foot print of the geomagnetic field line due to the solar wind compression of the dayside magnetosphere and the inflation of the geomagnetic field by increasing geomagnetic activity gave an uncertainty for the foot print location of around 50 km. A series of ATS-6 electron spectra from a time interval which embedded the rocket flight showed a successive hardening of the equator spectrograms during the rocket flight time. This suggested that ATS-6 was measuring in a conjugate region, which was more and more to the south of the auroral structures in the vicinity of the sounding rocket. The low energy trapped electron fluxes at ATS-6 were correlated with and even a condition for the auroral activity in the region of the foot print of the field line.

5. Spatial and temporal variations in the particle fluxes detected by the mother - daughter payloads

5.1 The mother - daughter philosophy

In the interpretation of data from measurements with intensity modulations in particle fluxes a very common difficulty is to determine whether the pulses are of temporal or of spatial origin. This is especially the fact in auroral particle measurements, where the variations in time and space very often are of the same magnitude and duration. With an identical and simultaneous particle detection in two from each other separated payloads a space - time resolution of the particle fluxes is possible, provided that the relative motion between the precipitation region and the payloads is known.

Figure 5.1a illustrates the passage of two rocket payloads, M and D, through a region with particle precipitation which is stationary relative to the Earth. Both these payloads are assumed to have identical particle detectors on board. When the payloads cross the precipitation region the particle flux variations will be recorded like in the diagrams shown in the lower part of Figure 5.1a.

Variations in the particle fluxes at the two energies, 8 keV (E_8) and 2 keV (E_2), will be detected simultaneously in each of the two payloads but there may be a time difference between the two payloads.

Simultaneous particle detection by the payloads M and D in a moving or a stationary structure could be explained by the relative velocity betwen the payloads and a favourable extension of the structure gradient. In the S17-1 measurements the aurora was elongated out into an east-west directed arc with a rather slow drift motion from the south to the north and also the S17-2 measurements were made in an aurora that exposed a parallel but no perpendicular drift motion of the auroral structure relative to the payload trajectory. If a stationary

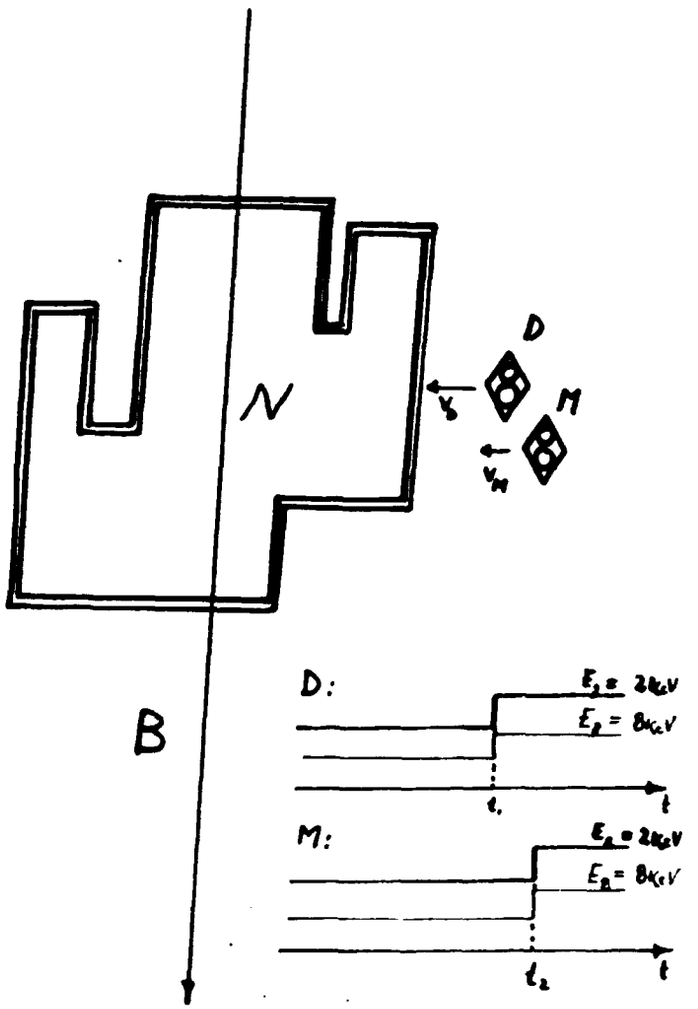

Figure 5.1a The rocket payloads M and D pass a particle precipitation region N with a time lag. In each payload the registration of particles at the energies E_2 and E_8 will occur simultaneously but with a time lag between the different payloads.

auroral structure shows significant variations of the particle fluxes with time, which are comparable with the measuring time, the reason to this modulation could be a precipitation of a new particle population into the region.

Variations of the fluxes then can be seen as due to a new population superimposed on the earlier stationary population.

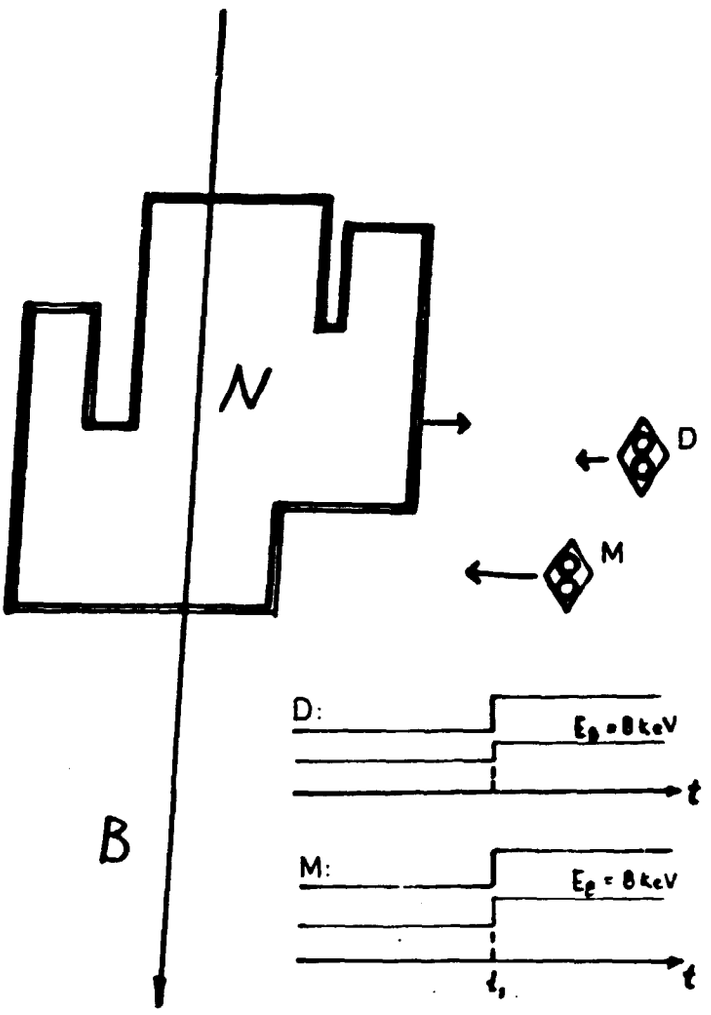

Figure 5.1b Simultaneous particle detection by the payloads M and D can be explained by a drifting or stationary structure N.

This is illustrated in Figure 5.1c and Figure 5.1d. The time dispersion, Δt, $t_1 - t_2$, respectively $t_3 - t_4$, is seen in the diagram of the Figure 5.1c and that gives a possibility to calculate the source distance s.

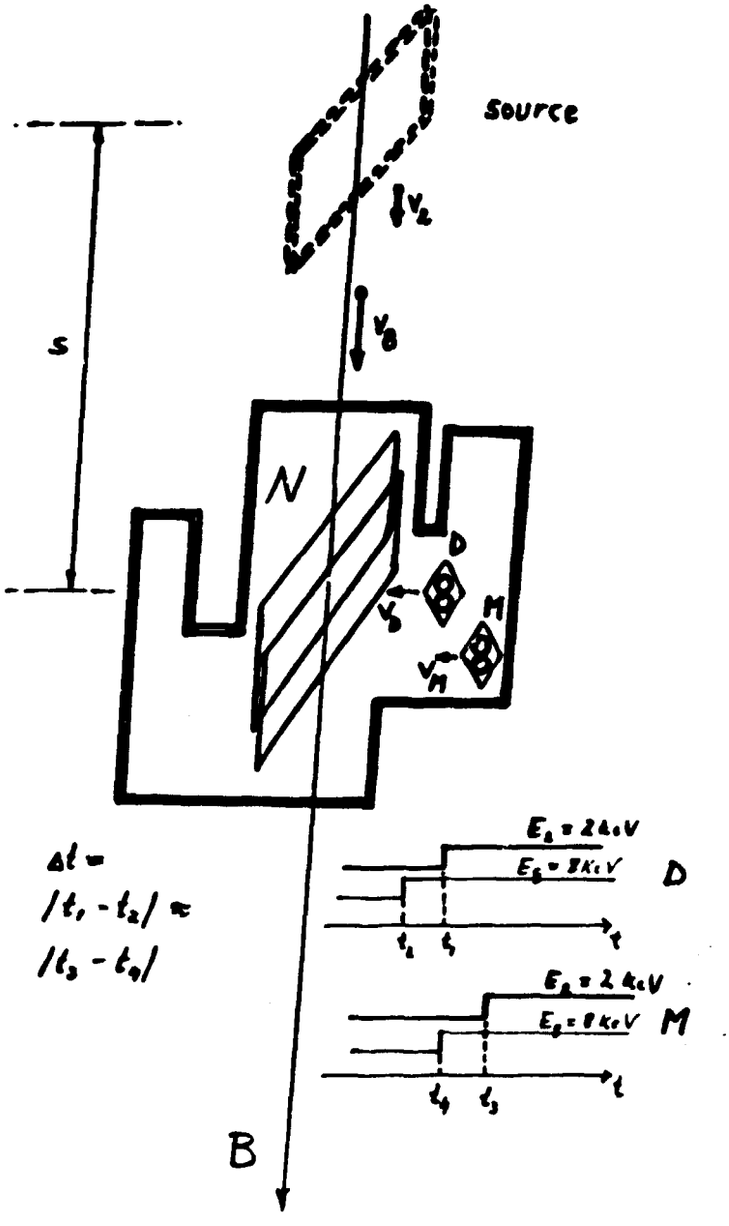

Figure 5.1c Measurement of the time difference Δt between the detection in the two payloads M and D at two different particle energies (E_2, E_8) gives a possibility to determine the distance (s) to the particle source.

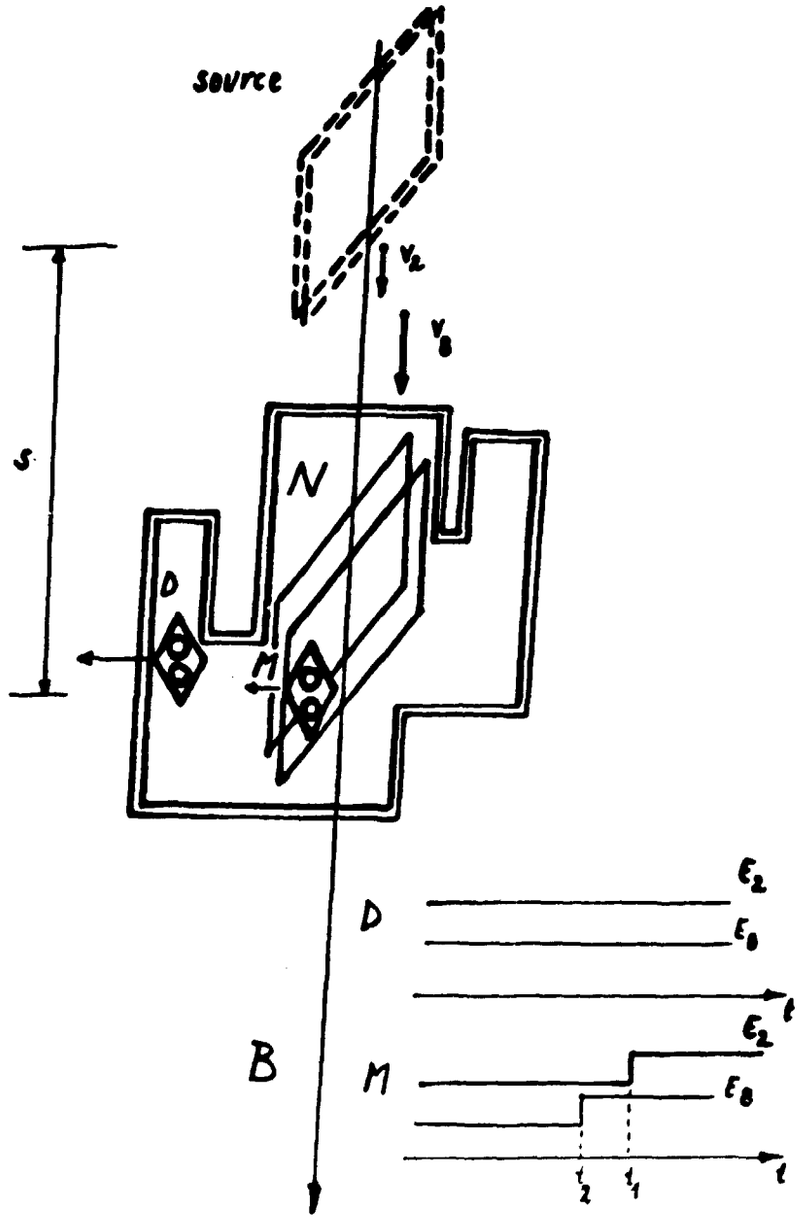

Figure 5.1d Spatial structures of precipitating particles in the auroral region may cause a modulation of the measured particle energies as illustrated in the diagram above.

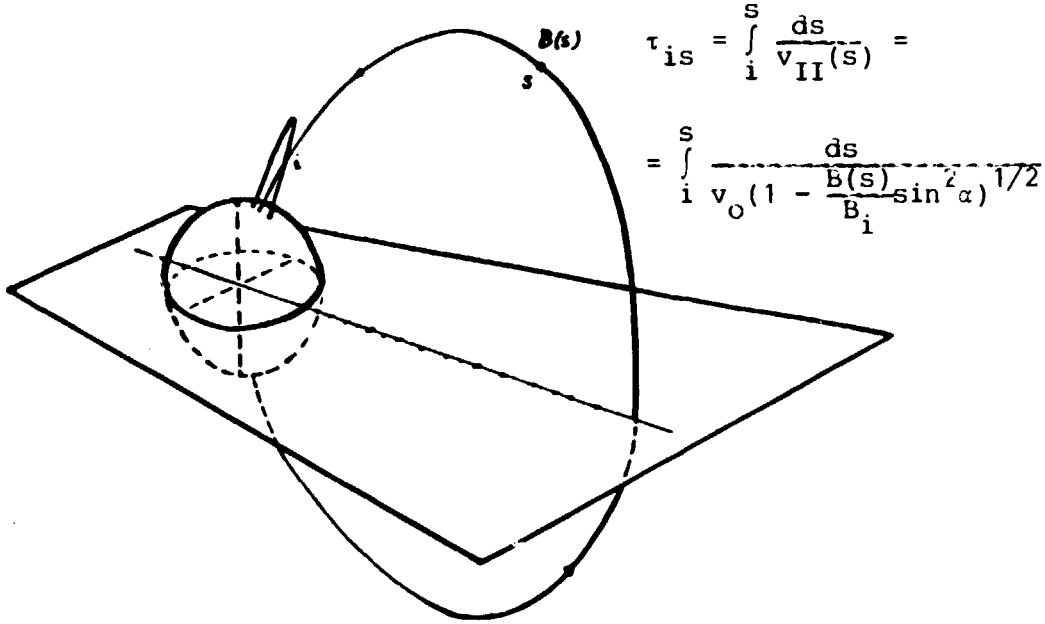

Figure 5.2 The formula for the period T_{si} of a particle's motion along a magnetic field line between the source (s) and the measuring point (i) gives a possibility to determine the distance i - s (Roederer, 1970).

5.2 A trapped particle's motion along the magnetic field line

The following relations exist between the components of the particles velocity, the pitch angle and the magnetic field

$v_{II} = v_0 \cos \alpha$;

$v_0 = \sqrt{\frac{2E}{m_e}}$ and

$v_{II} = v_0(1 - \frac{B(s)}{B_i} \sin^2\alpha_i)^{1/2}$; (Roederer, 1970).

Here E is the energy, m_e is the mass, α the pitch angle of the particles (electrons), B is the magnetic field, v_0 is the velocity of the particle and v_{II} is the velocity component parallel to the magnetic field lines, i is the point where the particle is detected.

The difference in particle velocities of two energies E_8 and E_2 can be calculated and thus the distance to the source of the modulations, s, can be estimated;

$$s = \frac{v_{8_{II}} \cdot v_{2_{II}}}{v_{8_{II}} - v_{2_{II}}} \cdot \Delta t$$

The bounce period of a trapped particle is

$$T_b = 2 \int_{s_m}^{s_m^1} \frac{ds}{v_{II}(s)} = \frac{2}{v} \int_{s_m}^{s_m^1} \frac{ds}{(1 - \frac{B(s)}{B_m})^{1/2}} \qquad \text{(Roederer 1970)}$$

where the period is the time for a trapped particle's motion along a magnetic field line from one mirror point s_m to the other s_m^1 and back again. The integral is extended along the field line (s), where B(s) is the magnetic field at a point s along the field line and B_m the magnetic field at the mirror point. A motion of a particle from a source, S_s, to the measuring point, S_i, can be described with the same formula

$$T_{si} = \frac{1}{v_0} \int_{S_i}^{S_s} \frac{ds}{(1 - \frac{B(s)}{B_i} \sin^2 \alpha_i)^{1/2}} \qquad (5f)$$

where i is the index for the particle pitch angle and the magnetic field at the rocket position.

5.3 Discrimination between spatial and temporal variations in the fluctuations of the particle fluxes.

By evaluating the integral in the formula 5f we got T_{si} as a function of s for the two energies 2 keV and 8 keV. Figure 5.3 shows a diagram of T_{si} for two energies and illustrates how Δt is obtained graphically [$\Delta t = T_{si}(2\ \text{keV}) - T_{si}(8\ \text{keV})$]. We assume that the measured particles are modulated simultaneously at the source and that their subsequent bouncing was an adiabatic motion along the magnetic field line.

Mostly there is no clear distinction between the time and space variations in the modulations of the particle fluxes. In some literature the time variations are identified as changes in the brightness of the emitted light and the space variations as changes in the shape of the precipitating region (Johnstone, 1978).

Another existing discrimination is to compare the intensity gradients with the sampling time of the experiment. When a variation occurs within the time resolution of the experiment, it is classified as a time variation.

Another possibility is to relate the difference in time between the occurrence of the flux variations at two different measuring points to the bouncing period of the actual parti-

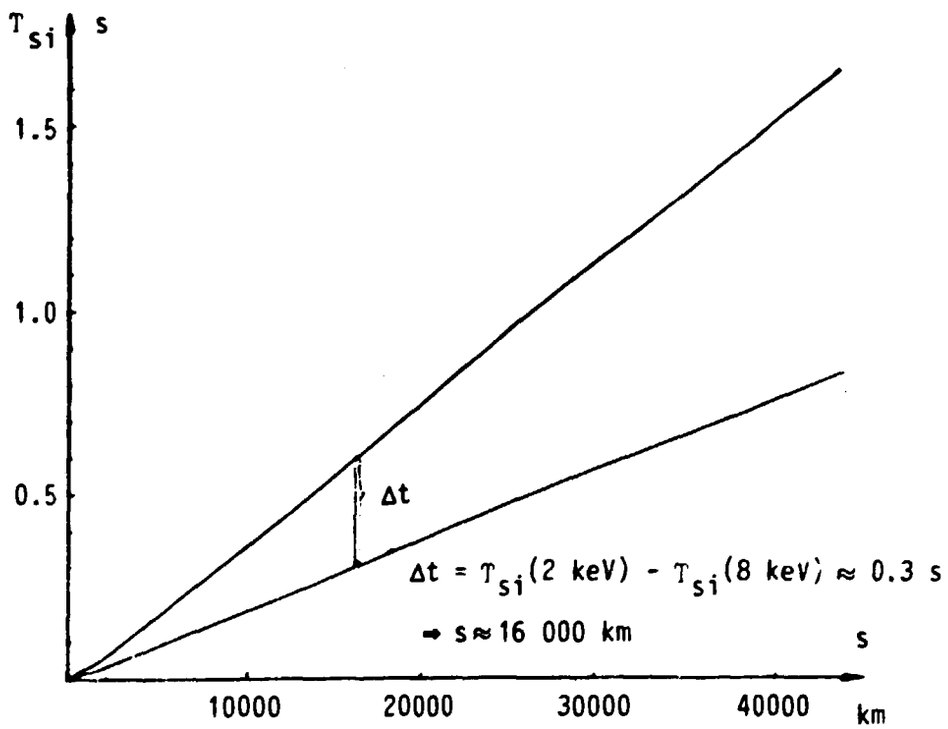

Figure 5.3. Diagram representing the time difference (Δt) between the occurrence of a gradient in the particle flux of two energies (2 keV, 8 keV) as a function of the distance to the modulation source (s).

cles. The classification for S 17 measurements is illustrated in Table 5.1. In the overlapping interval; the time resolution of the experiment < Δt < half the bouncing period; the discrimination must be based on combinations of several measurements or on special analyses.

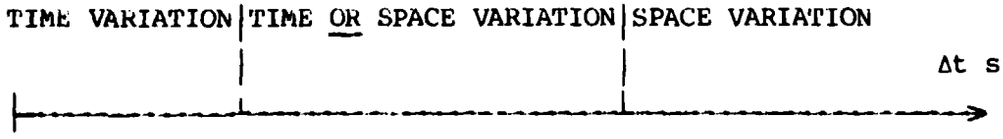

0	10 ms time resolution of the experiment	T/2 half the bouncing period of the actual particle	Δt = time difference between the two events

Table 5.1. Discrimination of the intensity variations by relating the time lags between the events to the time resolution of the experiment and to the particle bounce period.

5.4 Cross-correlation of data of electron fluxes of different energies obtained on the same payload

When two different signals are showing similarities in the intensity or time history, the signals exist with relationship (in Latin: cum relatio). By statistical analysis the magnitude of this relationship can be determined. If the signals are functions of time, $v_1(t)$ respectively $v_2(t)$ and T a time lag between them, the relationship is described by the cross-correlation coefficient r. r is a function of T and is defined

$$r(T) = \int v_1(t) \cdot v_2(t + T)\, dt \qquad (5g)$$

This cross-correlation function can have a maximum for an arbitrary T. In auroral particle measurements two data streams can be linearly correlated, but with one data set leading or

lagging the other by an unknown time shift. Therefore to answer the question what time lag optimizes the correlation, one performs a cross-correlation analysis. In the correlation analyses of S17 data we have used a computer program from Rutherford and Appleton Laboratories (courtesy of D.R. Lepine). In this cross-correlation program a number of samples of electron intensity data (counts per readout) were selected sequentially from a specific detector channel and compared with the same number of samples of the second electron data stream.

Determination of the correlation coefficient for different time lags (Δt) between the two signals was made to see if r had a maximum value for a specific time lag.

5.5 Some selected analyses of S17 data implicating the fluctuations to be temporal variations or spatial structures

Figure 5.4 shows the electron intensities plotted against flight time of two electron detectors (2 keV and 8 keV) throughout the flight of the mother payload of the S17-1 rocket. In order to eliminate the rocket spin modulation the intensities in this summary plot have been averaged over 2 payload spin periods ($\approx$ 0.6 s). The time resolution of the measurements was 10 ms in the mother payloads and 8 ms in the daughter payloads. No modulation effects on the intensities of the payload coning could be seen. There are obvious similarities in the shape and duration of the intensity fluctuations in the two detectors. All the major changes in the 8 keV electron intensity can be recognized in the 2 keV detector too. Similarities can also be seen in 2 and 8 keV electron detectors in both mother and daughter payloads, which is illustrated in the diagram for all four detectors in greater detail in Figure 5.5. This characteristic similarity existed also for the fluctuations in the recordings from the S17-2 payloads (see Figure 5.6), which suggests a common source for the measured particle intensity changes.

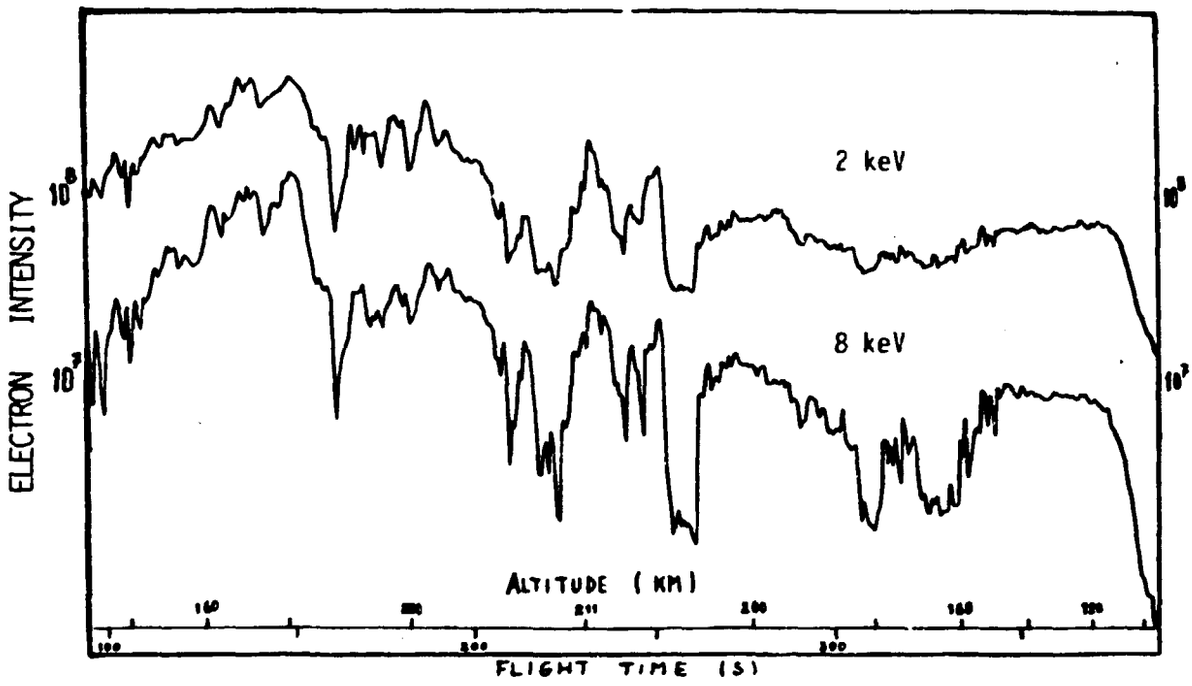

Figure 5.4 Averages over 2 rocket spin periods (≈0.6 s) of the changes in electron intensity as a function of rocket (S17-1) flight time and altitude.

However, clear time delays in the intensity changes were directly observable when corresponding electron channels from different payloads were studied. That was valid for both S17-1 and S17-2 payloads. According to the discussion in 5.3 the conclusion was made that the time delays demonstrated in Figures 5.7 - 5.10 were caused by spatial structures in the particle precipitation region. The distance between mother and daughter payloads increased during the flight (see Figure 1.15) and also the time delays are increasing with flight time (in Figure 5.8 $\Delta t \approx 0.5 - 1$ s).

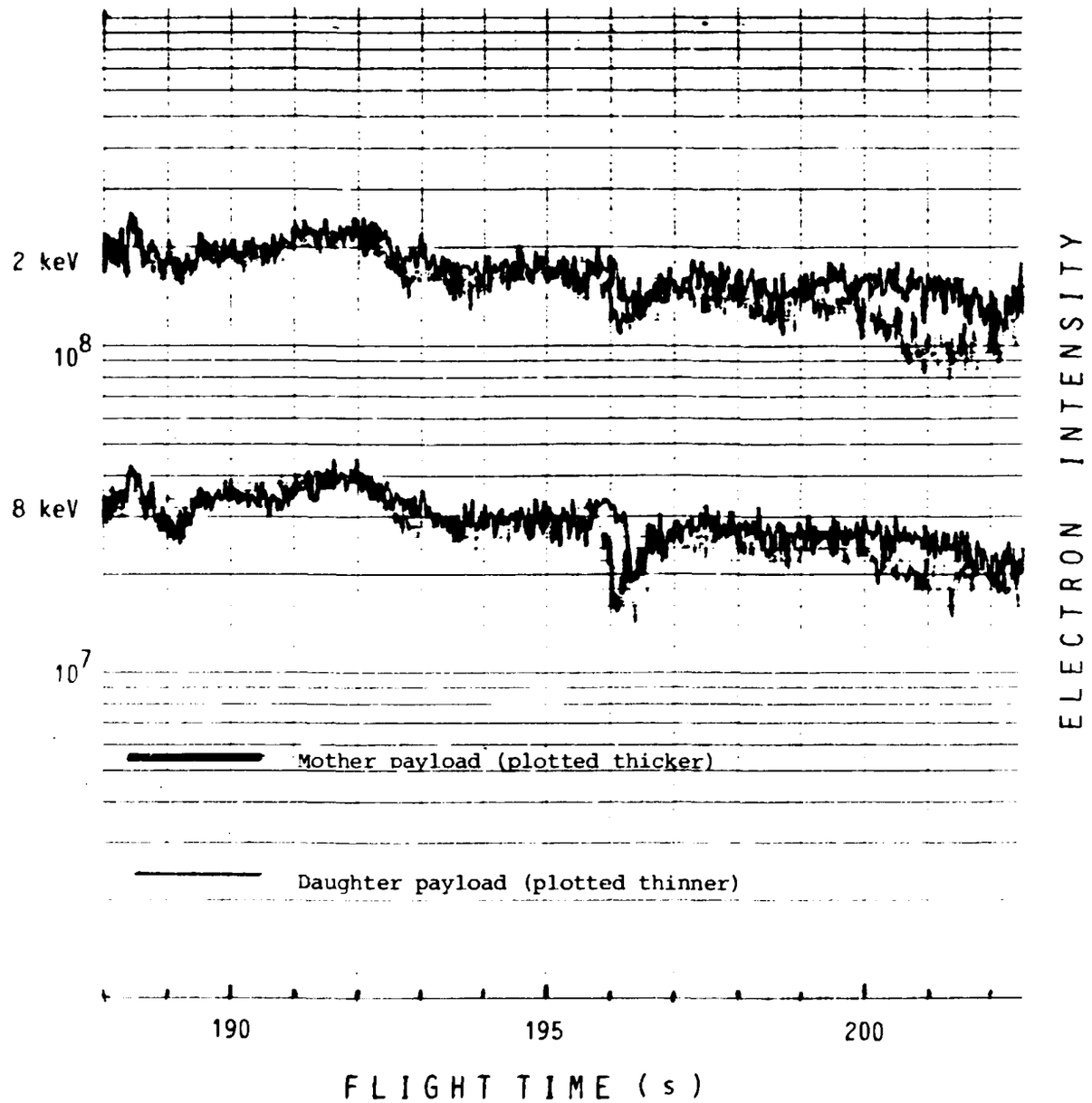

Figure 5.5 Electron intensity plots from both the mother and daughter payload (S17-1) showing similarities in all four electron recordings.

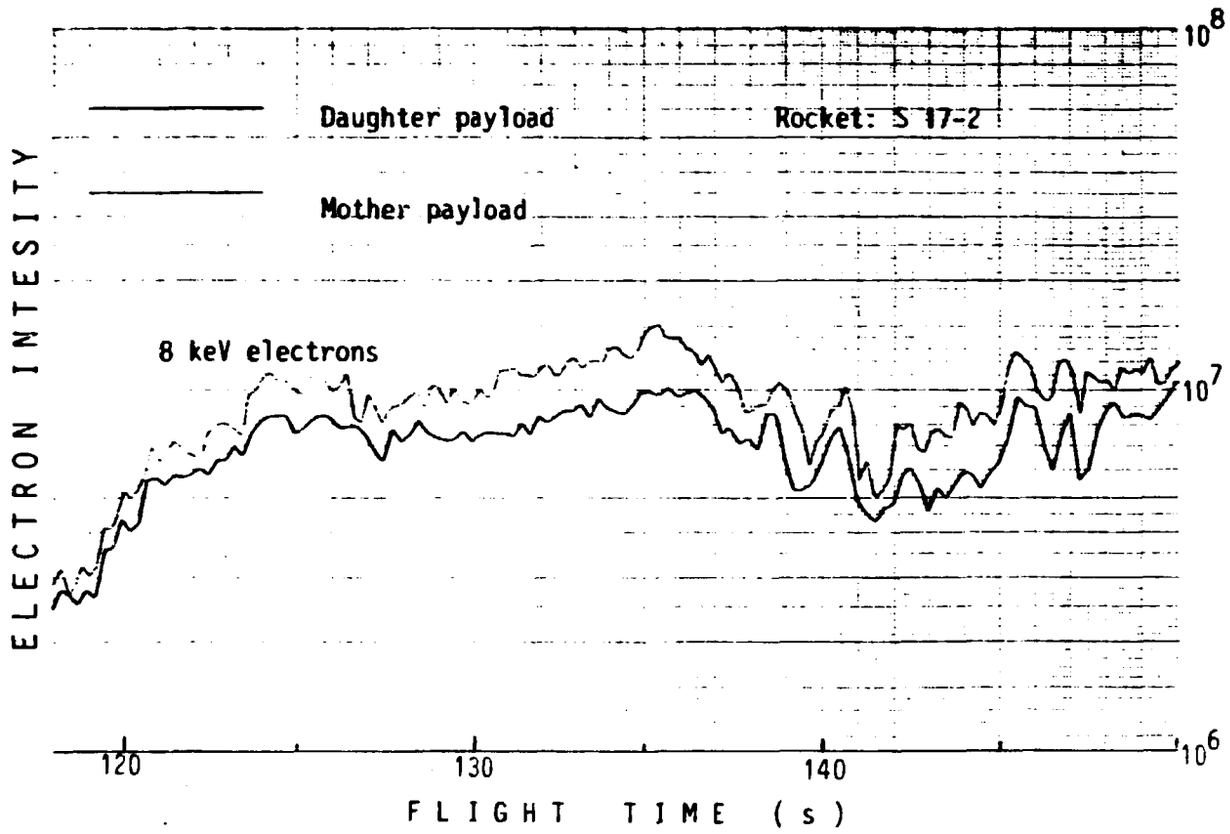

Figure 5.6 The 8 keV electron intensities (0.3 s averages) recorded at the mother and the daughter payload (S17-2) illustrating the similarities in the recordings.

A confirmation that the intensity changes which are illustrated in Figure 5.8 are of spatial origin is the fact that there is no obvious energy dependent time delay between the intensity changes recorded by detectors on the same payload (see Figure 5.11). The sharp gradients in the electron fluxes measured by the S17-1 payloads was the most striking event of the whole flight. In the event shown in Figure 5.6 the intensities changed by a factor of 10 in less than 1 s. between the drop at ≈251 s and the increase at ≈261 s the rocket traversed a horisontal distance of around 2 km.

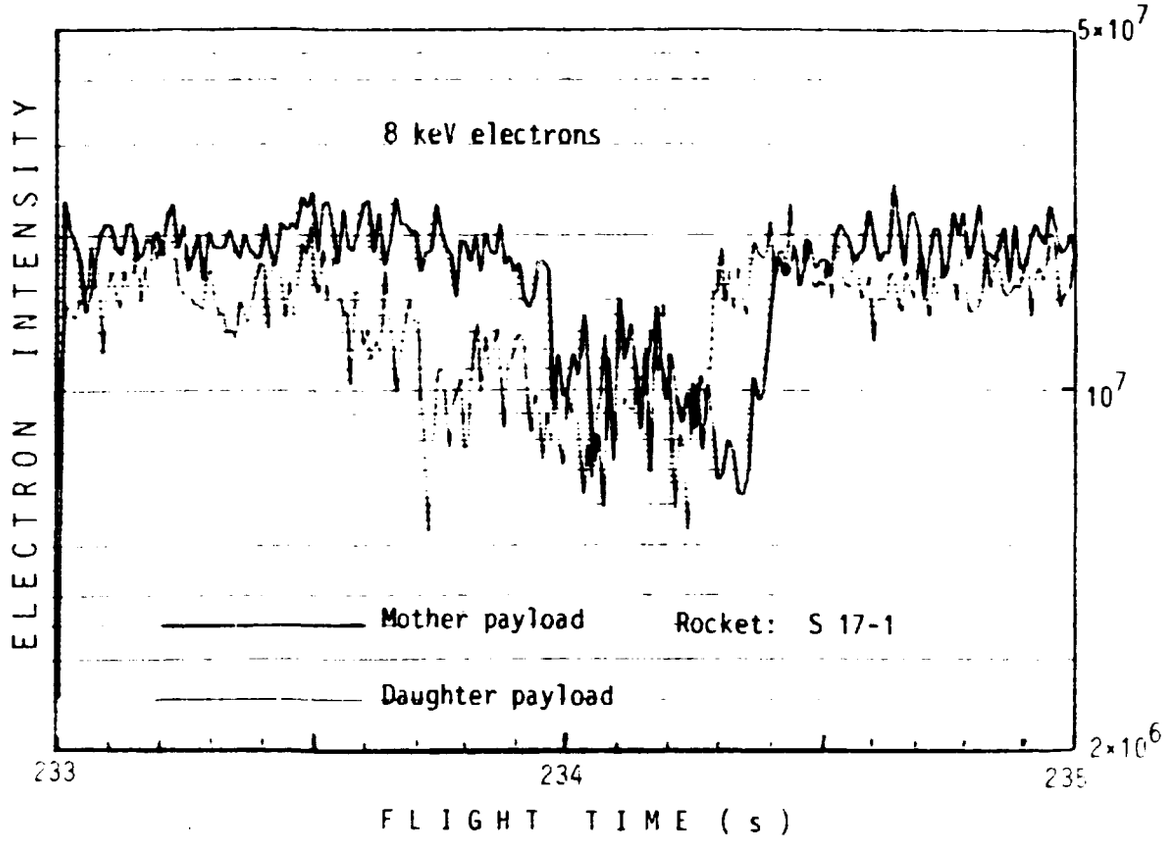

Figure 5.7 The 8 keV electron intensity recorded by mother and daughter payloads (S17-1). The two payloads intersected the structure in the particle precipitation region with a time lag of 0.15 - 1 s.

In the TV pictures obtained near the footpoint of the field line through the S17-1 rocket (Rappsåive) the drift to the north of the auroral structure was seen (see Figure 3.6 - 3.10). In 60 s the arc picture moved around 7 cm on the film. Opening angle of the camera was known and a rough calculation of the velocity of the arc and the expected time lag between mother and daughter was made. In the flight time interval 65-380 s time lags of the order of 0.3 - 3 s were expected. This agreed with the observations.

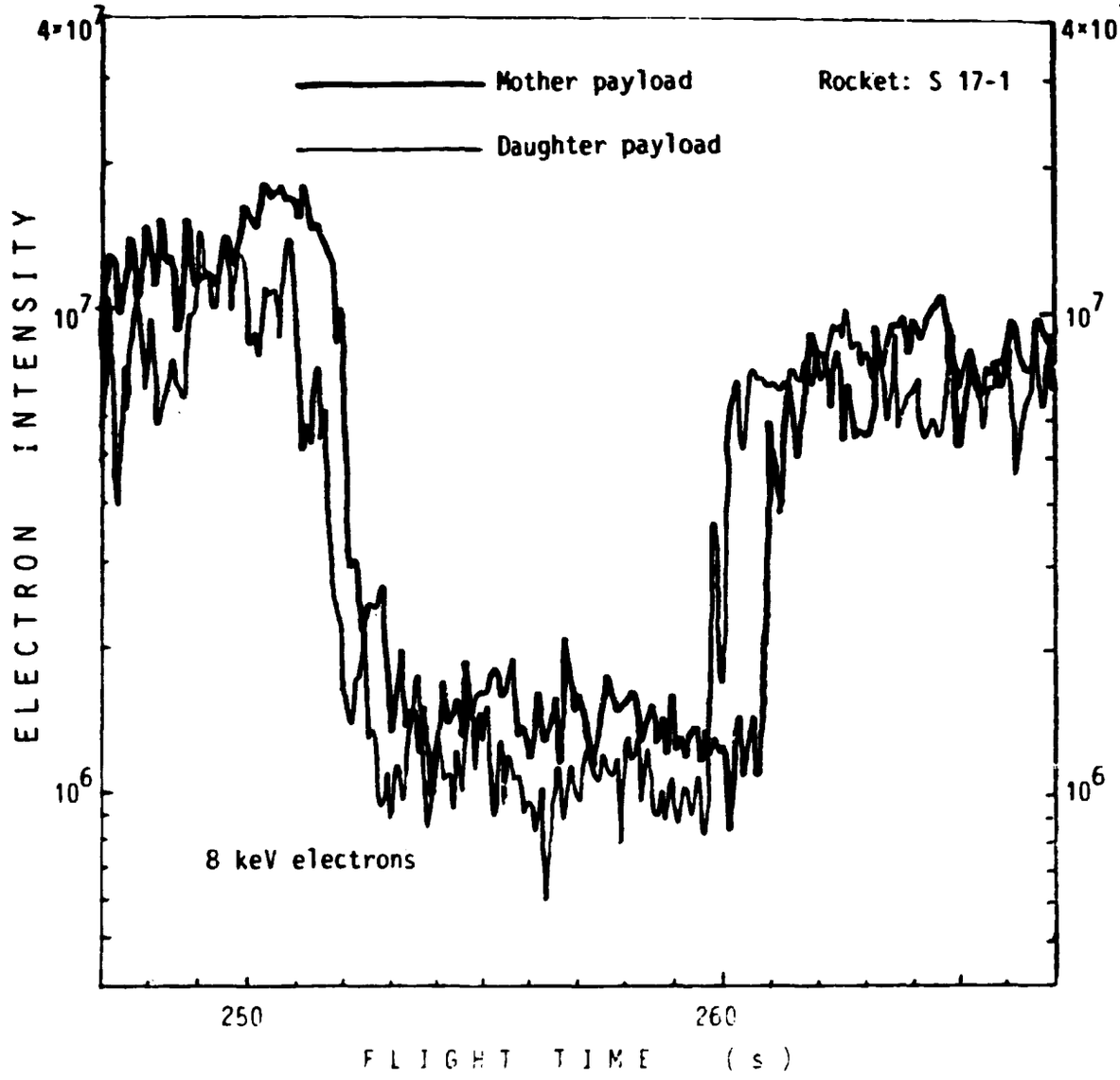

Figure 5.8 Time delayed changes ($\Delta t \approx 0.5 - 1$ s) in the 8 keV electron intensities caused by payload positions in the structures of the particle precipitation region.

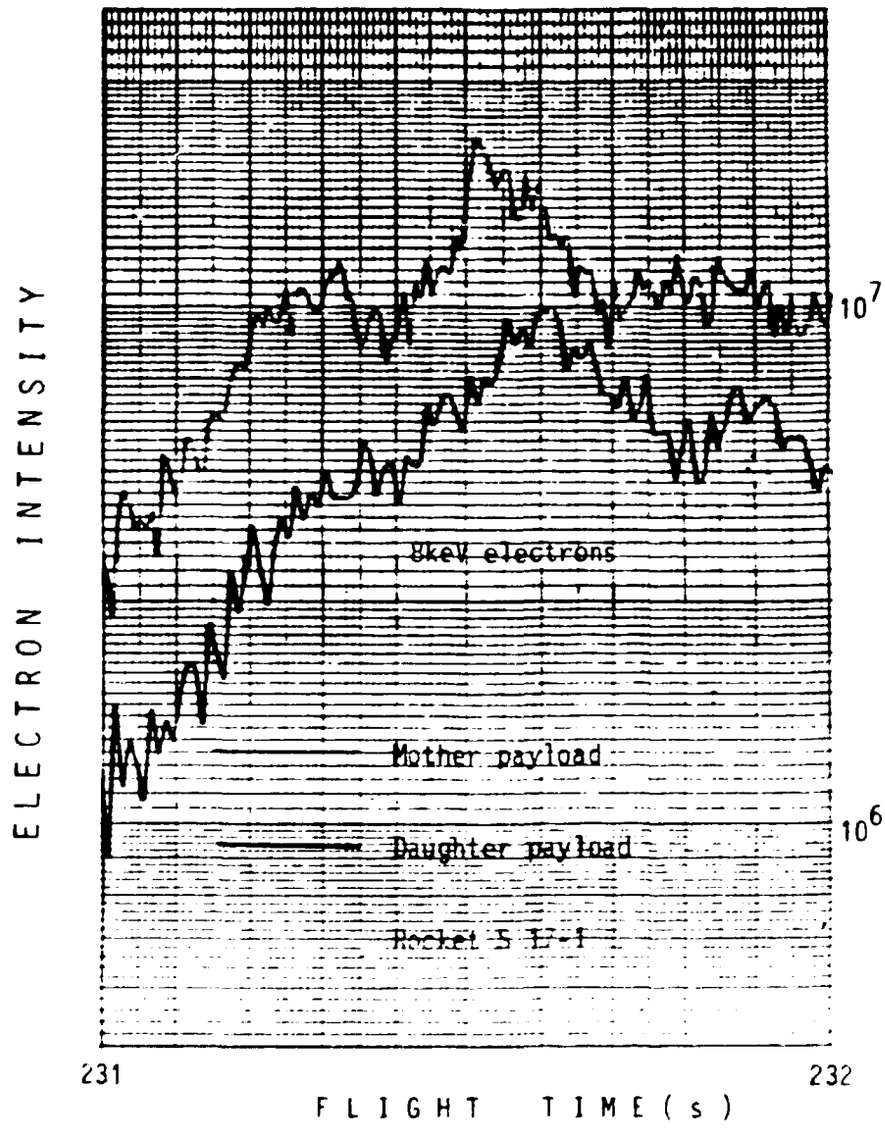

Figure 5.9a A time shift of around 0.1 s between observed electron intensities of the same energy (8 keV) at different payloads.

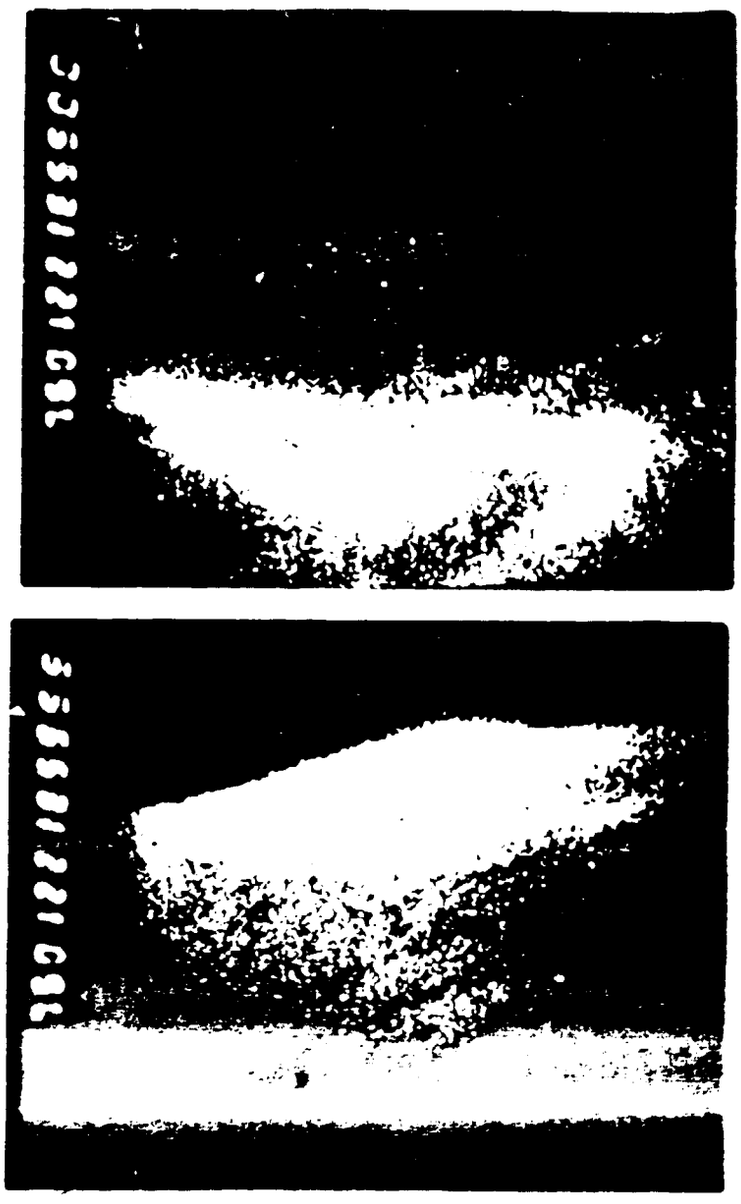

Figure 5.9b The northward movement of the aurora recorded on TV-film for a flight time interval of 60 s.

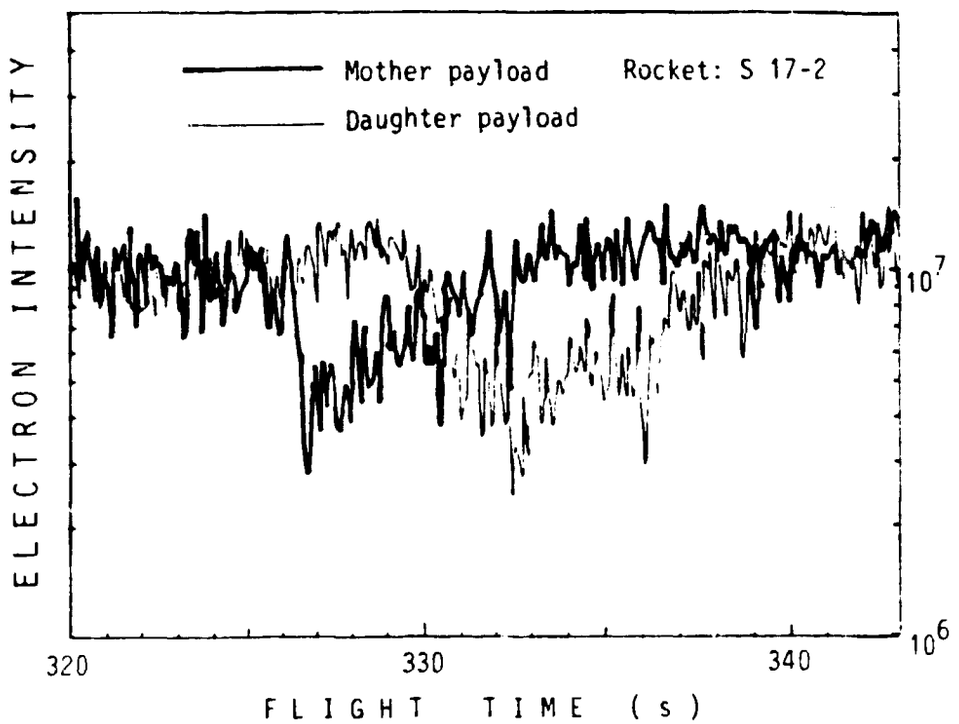

Figure 5.10 Observed 8 keV electron intensities from mother and daughter payloads (S17-2) indicating that the payloads are moving through a spatial gradient in the precipitation structure. Time difference between the recordings is around 5 s.

The time delays caused by the velocity dispersion of the particles were generally shorter than the delays which were of spatial origin. No consistent pattern of temporal or spatial intensity changes were found during the two rocket flights. Figure 5.12 represents one of the greatest time lags we have found in the S17 recordings and Figure 5.13 shows a selected number (two plots of each payload) of those time lags which gave a maximum value to the calculated cross-correlation coefficient r. In the correlation analyses we have used a program where the averages, the number of samples and time steps in the sequences were varied. Examples of the influence of the

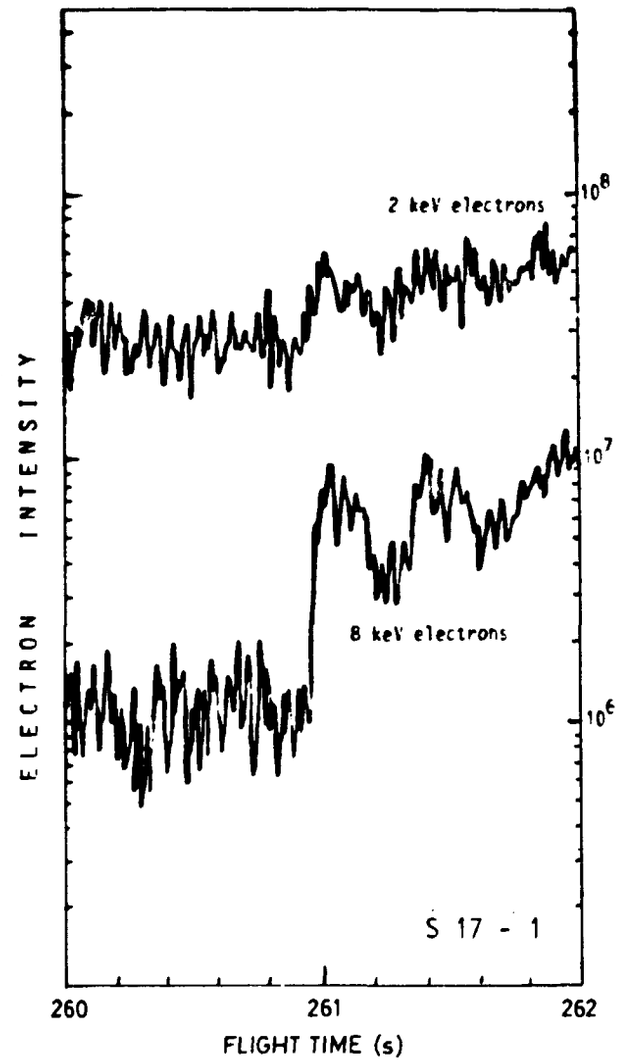

Figure 5.11 Two electron intensity plots from the same flight time interval as Figure 5.8, recorded on the same payload but of different energies.

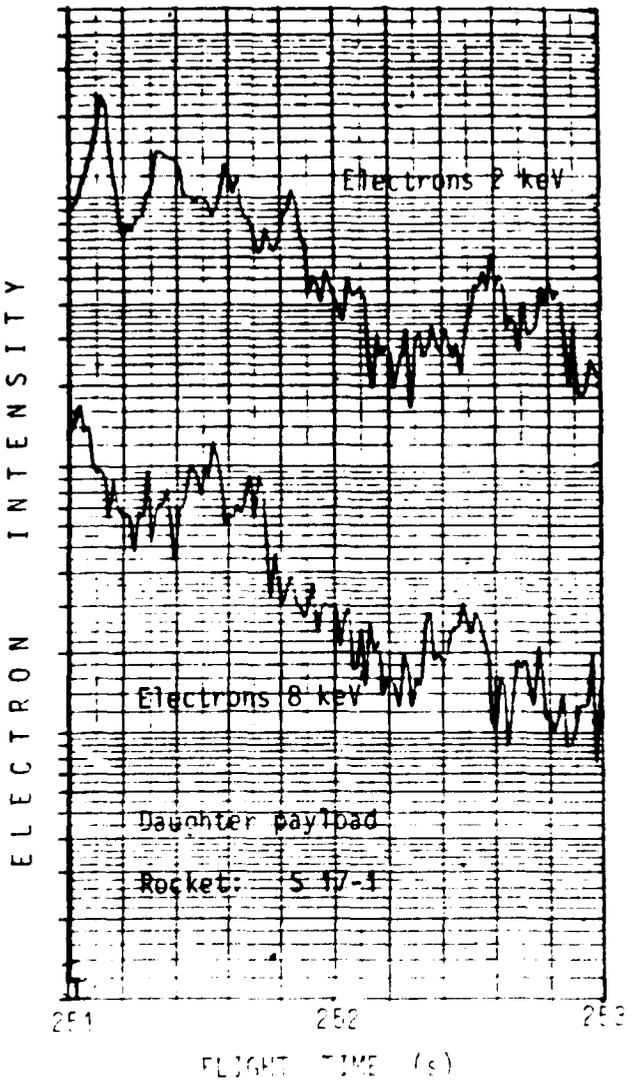

Figure 5.12 An apparent time delay ($\Delta t \approx 0.15$ s) between 8 keV and 2 keV electrons recorded by the daughter payload of S17-1. The intensity variations are interpreted as temporal ones.

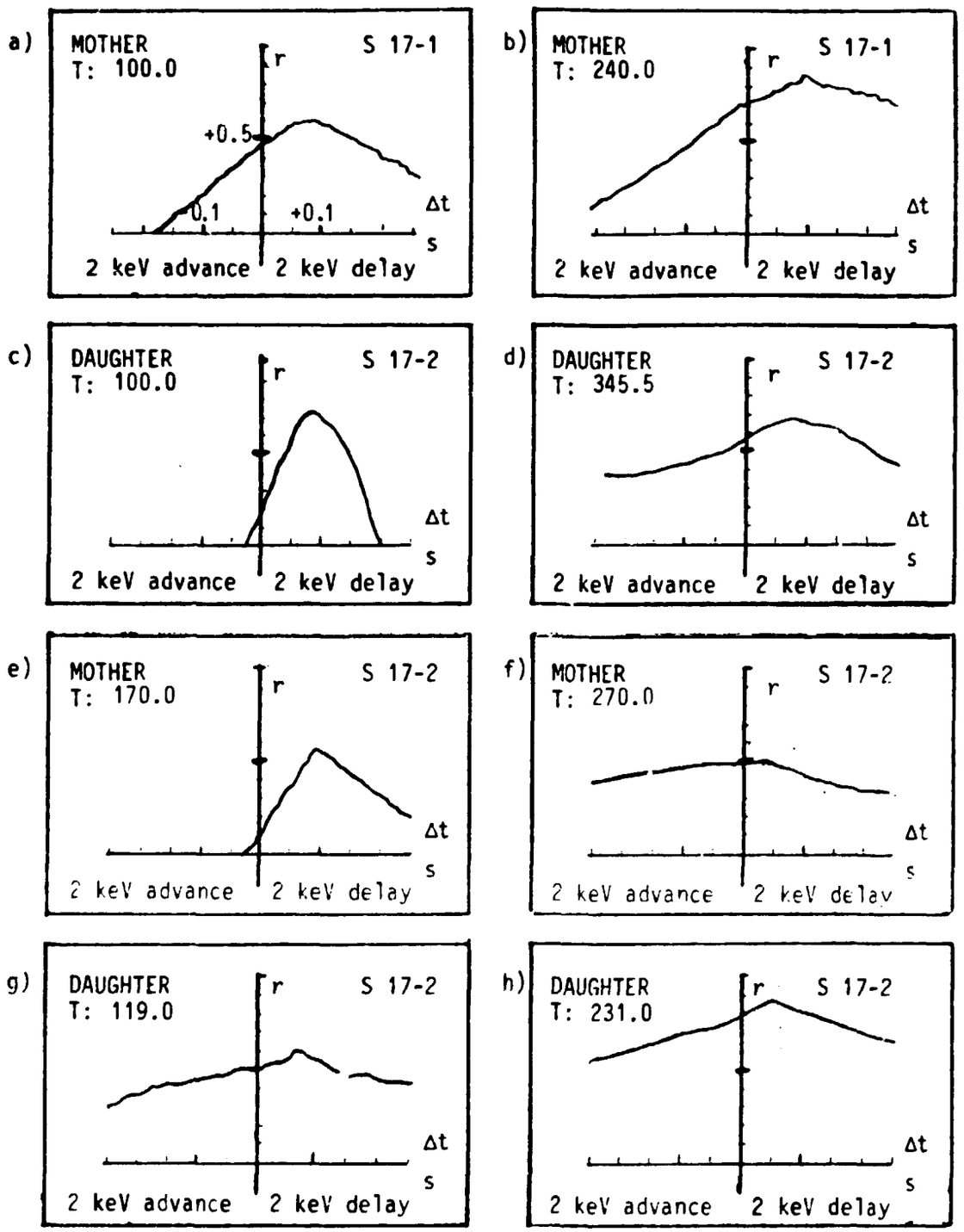

Figure 5.13 The cross correlation coefficient (r) between 8 keV and 2 keV electron intensities against a time shift (Δt) introduced between the two electron detectors. r was calculated for different time intervals (1-10 s). T is the beginning of the interval.

payload spinrate and the deduced r_{max} for a negative value of Δt are presented in Figure 5.14. If the assumptions are valid i.e. that the particle flux modulations originate from a common source for all particle energies, and that the particles later on their way along the flux tube were unaffected by acceleration or deacceleration mechanisms, then this modulation source must be situated less than 10 000 km from the rocket position.

5.6 Summary of precipitated particles and electric field measurements by the rocket S17-1

A summary of the particle data from the S17-1 rocket is presented in Figure 5.15. Here the measured electron fluxes of 2 keV and 8 keV energies and the precipitated total energy flux were depicted against the flight time. The 0.6 s averages of the electron intensities were determined from the two fixed energy detectors and the integrated energy of the precipitated electrons was obtained from the swept detector in the energy interval 1-16 keV. Weak spin modulations were observed in parts of the flight both on the mother and daughter payloads.

It is convenient to devide the S17-1 flight into three time intervals namely 1) 90-205 s, 2) 205-255 s and 3) >255 s. A relatively strong low energy electron flux dominated the first period. The fluxes in this period were over the whole energy range significantly higher than during the two latter intervals. 2 keV electrons displayed fluxes in excess of $10^8 cm^{-2}s^{-1}sr^{-1}keV^{-1}$. The fluxes were rapidly variating and a sudden drop in the middle of the interval (≈150 s) exceeded factors of 5-10. Apart from this rapid drop all energy channels stayed fairly constant during this interval. The ground based TV observations showed that two discrete auroral arcs were passed by the rocket at 110-150 s and 160-200 s flight time. When the payloads intersected the field lines of the first auroral arc the energy spectra were weakly peaked. The peak energy increased slowly with time and at 125 s the spectrum had its peak at 8 keV. After 125 s the spectra became

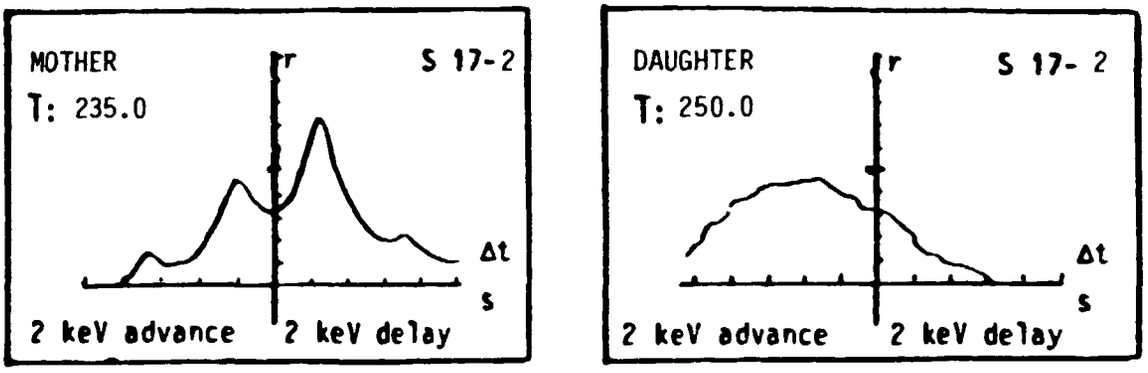

Figure 5.14 These diagrams illustrate
a) the influence of the rocket spin rate on the cross correlation function $r(\Delta t)$.
b) an obtained result of r_{max} for a negative Δt value.

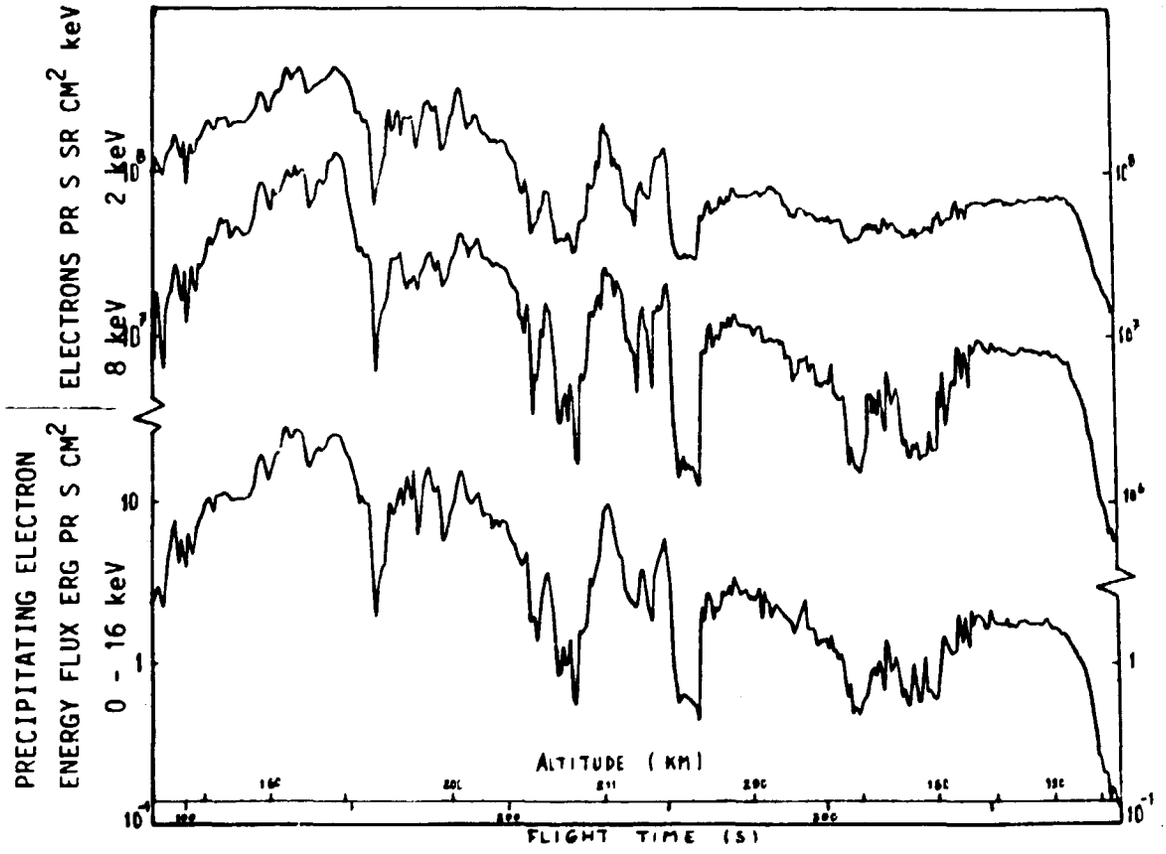

Figure 5.15 Observed precipitating electron fluxes (upper part) and the electron energy obtained at rocket S17-1.

softer again so the first part of interval 1 displayed energy spectra of type 'inverted V'. The hardest spectra were observed when the payload traversed field lines connected with regions of the intense discrete arc which is seen on the TV film picture at 19.01.00 UT (see Figure 3.9). The electron fluxes measured on the rocket agreed very well with the optical data obtained from the ground by low light level TV and all-sky cameras. Magnetic field-aligned potential drops together with inverted-V events in the particle energy distribution are included in models of the potential distribution at rocket altitudes. For measurements inside such regions a reversal of the electric field is predicted when the payload is traversing the field lines of the acceleration region (Lundin, 1977). We have observed a reversal of the electric field at ≈150 s suggesting that the rocket in this time interval passed inside a region with parallel potential drop.

During interval 2) (205-255 s) highly increased electron intensities at low energies were observed. The TV-film showed visible auroral structures but the energy of the precipitating particles was too low to create intense discrete arcs. Intervals 2 and 3 were separated by a large drop in the particle intensities which stayed for ≈10 s. The interval 3) (>260 s) showed fairly constant particle precipitation of low intensity.

As mentioned in Chapter 4 the electric field was measured at the S17-1 rocket. The results of these measurements are presented in Figures 5.17 and 5.18 (courtesy of U. Fahlesson). Due to a technical failure only 2 of the 4 spherical electrodes in the probes worked, but in spite of that two horizontal components of the electrical field were obtained at the S17-1 mother payload. The measuring technique with spherical probes mounted on matched booms extended in opposite directions from the payload requires an accurate symmetry and very good connection between the probes and the surrounding plasma (Fahlesson, 1967). The accuracy of the presented values of the

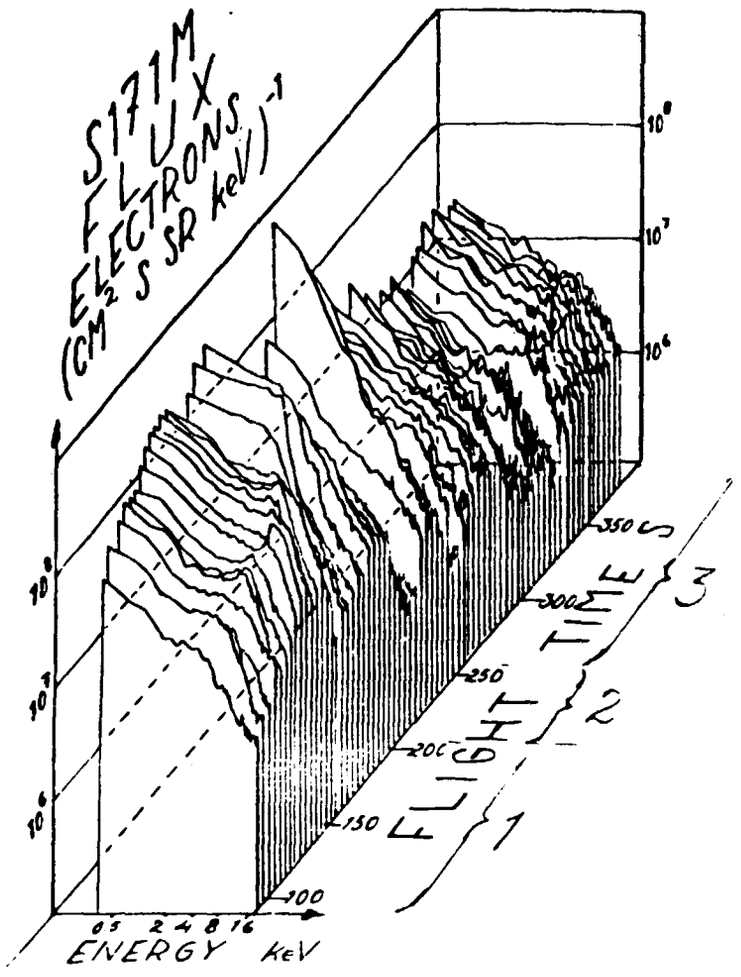

Figure 5.16 A three dimensional plot with spectra of precipitated electron intensities obtained at S17-1 rocket. The rocket flight is devided into 3 intervals 1) 90-205 s, 2) 205-255 s and 3) >260 s.

electric field is ±5 mV/m. A general characteristic of the electric field during the S17-1 flight is that the field was weak but rather stable with a north-west directed horizontal component. We have compared some features in the field components with the particle precipitation and the auroral situation. When the S17-1 payloads entered a structure of visual aurora (≈85 s) at an altitude of ≈120 km, the E_{NM} component increased, E_{WM} dropped to zero and turned to east. Inside the visible arc (≈85-205 s) the field had its maximum value

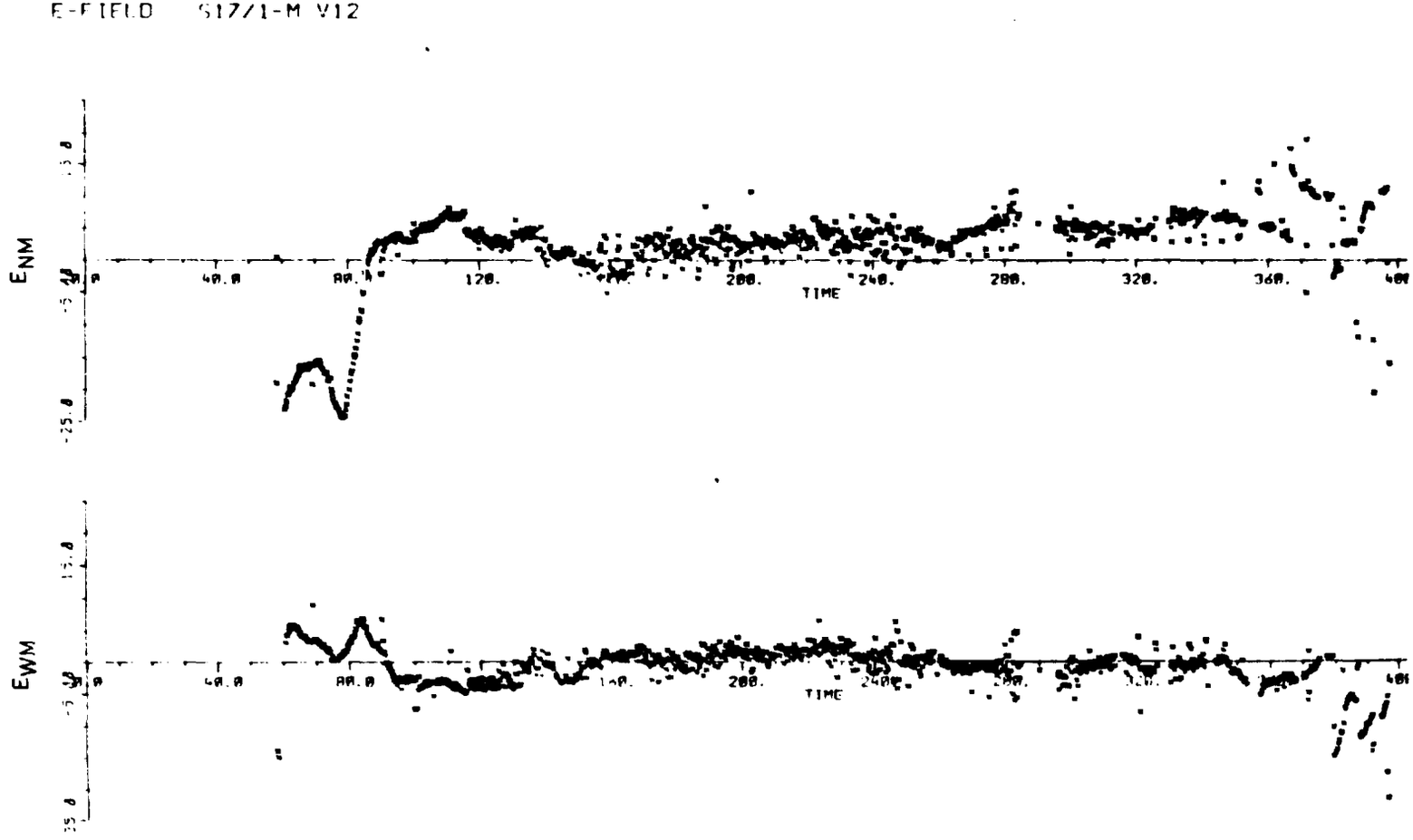

Figure 5.17 Two horizontal electric field components, E_{NM} with north as positive direction and E_{WM} with west as positive direction measured at the mother payload S17-1

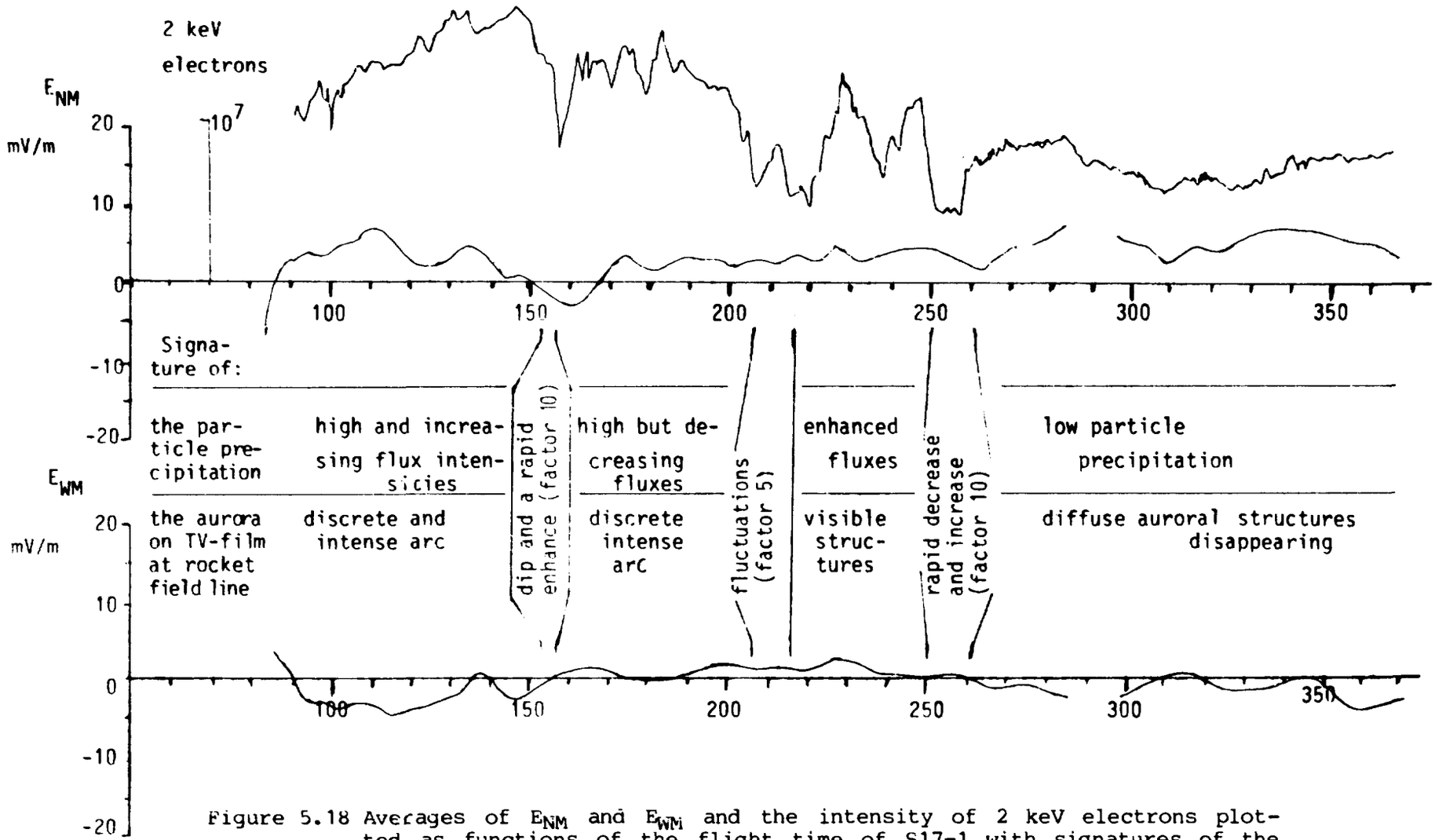

Figure 5.18 Averages of E_{NM} and E_{WM} and the intensity of 2 keV electrons plotted as functions of the flight time of S17-1 with signatures of the aurora on the TV film and the total particle precipitation.

(E_{NM} ≈ 7 mV/m at 210 s). This value was the highest and most stable during the entire flight of S17-1. After 280 s E_{NM} reached values in the same order of size but the recordings showed scattered values remaindering of a more unstable field character.

At 140-150 s both the electric field components dropped to zero when the payload passed a sharp gradient in the structure and the very intense particle fluxes in this period showed a sudden increase with a factor of 10 at ≈155 s.

In the flight period around 85-205 s (corresponding to the interval 1 in the particle precipitation) when the rocket traversed a structure of high particle precipitation a north-east directed horizontal electric field component with an average value around 5 mV/m was observed. The TV film showed that the rocket passed over a discrete arc. The sudden and deep increase in the particle precipitation data (≈155 s) occurred simultaneously with the changes of both the E_{NM} and the E_{WM} component. According to earlier reports (De La Beaujardiere et al., 1977) the east-west electric field component is expected to reverse when the payload is entering regions of discrete auroral arcs. This is in agreement with our observations.

During the latter part of this first interval (≈155-205 s) the electron flux intensities decreased but still showed values greater than what could be observed in later periods. Also the E_{NM} component decreased in this interval (≈155-205 s) but returned to higher values later during the flight, when no visible aurora occurred and the particle fluxes were lower.

For the period 205-255 s (corresponding to the interval 2 in the particle precipitation) the direction of the horizontal electric field component turned from north-east to north-west. At 205 s the particle data showed a very sharp gradient (decrease of fluxes) and the rocket left the region of visible arcs. The gradient in the particle precipitation was seen as a drop in E_{WM} component but a time lag of ≈5 s could be seen.

In general the gradients in the precipitating electron fluxes at 155 s, 205 s, 255 s and 305 s were observable later in the changes of the electric field components with a time lag of ≈5 s.

After 260 s (corresponding to the interval 3 in the particle precipitation) the horizontal electric field component began to change from north-east to the north-west direction like it had in the first part of the flight. However, the field was now weaker and much more variable. In this period a 10 s long gap in the electric field data occurred. In the beginning of this period some very weak and diffuse structures could be seen near the rocket field line but they disappeared afterwards and low energy particles dominated the precipitation.

5.7 Conclusion

The intensities of 8 keV and 2 keV electrons have been measured from one sounding rocket launched into a breakup aurora of moderate activity and from another rocket launched into a very active substorm situation. Both the rockets were of mother-daughter type i.e. had two separated payloads. The general features in the data of different particle energies were very similar over the whole flight time of the rockets. Special events and gradients and well identifiable shapes in the particle intensities were studied to see if the intensity fluctuations obtained from two detectors in one payload or from detectors into separate payloads were time delayed. Such time delays in the particle flux intensities were obvious in both of the rocket measurements and most of these time shifts could be understood as caused by spatial variations in the particle precipitation. In parts of the rocket flights the particle intensity variations were true temporal changes. The time lags between 8 keV and 2 keV electron intensities detected in the same payload, which could be observed and were obtained by crosscorrelation analyses, were in the range less than 0.3 s and most of them less than 0.1 s.

If the time differences are assumed to be caused by the velocity dispersion of the particles, the particle data reported here placed the modulation source at a distance of less than 10 000 km from the rocket position.

Measurements at the S17-1 mother payload of the electric field have been compared with data of precipitating electrons and low-light-level-TV-recording of the auroral situation. An inverted-V precipitation event was observed and was associated with auroral arcs and with reversals of the measured electric field components implicating the possibility of the existence of field-aligned potential drops as an acceleration mechanism for the precipitating auroral particles.

References

Akasofu, S.-I., The development of the auroral substorm, Planet. Space Sci., 12, 273, 1964.

Akasofu, S.-I., Polar and magnetospheric substorm, D. Reidel Publishing Company, Dordrecht, Holland, 1968.

Akasofu, S.I., and C.I. Meng, A study of polar magnetic substorms, J. Geophys. Res., 74, 293, 1969.

Archuleta, R.J., and S.E. DeForest, Efficiency of Channel Electron Multipliers for electrons of 1-50 keV, Rev. Sci. Instrum., 42 89, 1971.

Arnoly, R.L., Auroral particle precipitation and Birkeland currents, Rev. Geophys. Space Phys., 12, 217, 1974.

Aubry, M.P., A short review of magnetospheric substorm, In earth's magnetospheric processes, Edited by B.M. McCormac, p. 357, 1972.

Birkeland, K., The Norwegian Aurora Polaris expedition 1902-1903, vol. 1, On the cause of magnetic storms and the origin of terrestrial magnetism, Sect. 1, Christiana, H. Aschehoug 1908.

Birkeland, K., The Norwegian Aurora Polaris expedition 1902-1903, vol. 1, On the cause of magnetic storms and the origin of terrestrial magnetism, Sect. 2, Christiana, H. Aschehoug 1913.

Boström, R., A model of the auroral electrojet, J. Geophys. Res., 69, 4983, 1964.

Bryant, D.A., G.M. Courtier, and G. Bennett, Equatorial modulation of electrons in a pulsating aurora, J. Atmos. Terr. Phys., 33, 859, 1971.

Bryant, D.A., G.M. Courtier, and A.D. Johnstone, Modulation of auroral electrons at large distances from the Earth, J. Atmos. Terr. Phys., 31, 579, 1969.

Bryant, D.A., M.J. Smith, and G.M. Courtier, Distant modulation of electron intensity during the expansion phase of an auroral substorm, Planet. Space Sci., 23, 867, 1975.

Choy, L.W., R.L. Arnoldy, W. Potter, P. Kintner, and L.J. Cahill, Field-aligned particle currents near an auroral arc, J. Geophys. Res., 76, 8279, 1971.

Christophersen, P., Calibration of a satellite experiment for auroral particles and some relevant properties of the channel multiplier detector, Arkiv f. geofysik, 5, 659, 1971.

Cloutier, P.A., H.R. Anderson, R.J. Park, R.R. Vondrak, R.J. Spiger, and B.R. Sandel, Detection of geomagnetically aligned currents associated with an auroral arc, J. Geophys. Res., 75, 2595, 1970.

Cummings, W.D., and P.J., Jr. Coleman, Simultaneous magnetic field variations at the earth's surface and at synchronous, equatorial distance, Radio Sci., 3, 758, 1968.

DeForest, S.E., and C.E. McIlwain, Plasma clouds in the magnetosphere, J. Geophys. Res., 76, 3587, 1971.

De La Beaujardiere, O., R. Vondrak, and M. Baron, Radar observations of electric fields and currents associated with auroral arcs, J. Geophys. Res., 82, 5051, 1977.

Doupnik, J.R., P.M. Banks, M.J. Baron, C.L. Rino, and J. Petriceks, Direct measurements of plasma drift velocities at magnetic latitudes, J. Geophys. Res., 77, 4268, 1972.

Eather, R.H., S.B. Mende, and R.J.R. Judge, Plasma injection at synchronous orbit and spatial and temporal auroral morphlogy, J. Geophys. Res., 81, 2805, 1976.

Evans, D.S., and T.E. Moore, Precipitating electrons associated with the diffuse aurora: Evidence for electrons of atmospheric origin in the plasma sheet, J. Geophys. Res., 84, 6451, 1979.

Fahleson, U., Theory of electric field measurements conducted in the magnetosphere with electric probes, Space Sci. Rev., 7, 238, 1967.

Frank, L.A., N.A. Saflekos, and K.L. Ackerson, Electron precipitation in the postmidnight sector of the auroral zones, J. Geophys. Res., 81, 155, 1976.

Fukushima, N., Ground magnetic effect of field-aligned currents connected with ionospheric currents, Geophysical Research Laboratory, University of Tokyo, Japan, 1976.

Gurnett, D.A., and L.A. Frank, Observed relationship between electric field and auroral particle precipitation, J. Geophys. Res., 78, 145, 1973.

Gustafsson, G., A revised corrected geomagnetic coordinate system, Ark. Geofys. 5, 595, 1970.

Heppner, J.P., The Harang-discontinuity in auroral belt ionospheric currents, Geophysiske Publikasjoner, 29, 1972.

Hones, E.W., J.R. Asbridge, S.J. Bame, and S. Singer, Energy spectra and angular distributions of particles in the plasma sheet and their comparison with rocket measurements over the auroral zone, J. Geophys. Res., 76, 63, 1971.

Horwitz, J.L., J.R. Doupnik, and P.M. Banks, Chatanika radar observations of the latitudinal distributions of auroral zone electric fields, conductivities and currents, J. Geophys. Res., 83, 1463, 1978.

Hultqvist, B., On the production of a magnetic field-aligned electric field by the interaction between the hot magnetospheric plasma and the cold ionosphere, Plant. Space Sci., 19, 749, 1971.

Hultqvist, B., and H. Borg, Energetic ions in inverted-V events, KGI Preprint no 77:301, 1977.

Johnstone, A.D., and T.N. Davis, Low-altitude acceleration of auroral electrons during break-up observed by a mother-daughter rocket, J. Geophys. Res., 79, 1416, 1974.

Jones, A.V., Aurora, Dordrecht, Reidel, 1976.

Kisabeth, J.L., and G. Rostoker, The expansive phase of magnetospheric substorm. 1. Development of the auroral electrojets and auroral arc configuration during a substorm, J. Geophys. Res., 79, 972, 1974.

Küppers, F., J. Untiedt, W. Baumjohann, K. Lange, and A. Jones, A two-dimensional magnetometer array for ground-based observations of auroral zone electric currents during the International Magnetospheric Study (IMS), Submitted to J. Geophys., 1979.

König, R., Eine Untersuchung des magnetischen Sturms vom 6./7. März 1976 mit Auswertung und Interpretation einiger Messungen des Raketenexperiments S 17/2, Münster 1979.

Langel, R.A., Near-earth magnetic disturbance in total field at high latitudes, 2. Interpretation of Data from Ogo 2, 4 and 6, J. Geophys. Res., 79, 2373, 1974.

Lepine, D.R., D.S. Hall, D.A. Bryant, A.D. Johnstone, P.J. Christiansen, and M.P. Gough, 2.2 Hz oscillations in auroral electrons, Proceedings of the Vth ESA-PAC Symposium on European Rocket & Balloon Programmes & Related Research - Bournemouth (UK), 14-18 April 1980 - ESA SP-152, June 1980 a.

Lui, A.T.Y., P. Venkatesan, C.D. Anger, S.-I. Akasofu, W.J. Heikkila, J.D. Winninghan, and J.R. Barrows, Simultaneous observations of particle precipitations and auroral emissions by the ISIS 2-satellite in the 19-24 MLT sector, J. Geophys. Res., 82, 2210, 1977.

Lundin, R., and L.E. Andersson, Comparison of light emission and auroral particles in a post-break-up aurora, Proceedings of a symposium held at Örenäs slott, Sweden, ESRO SP-107, 267, 1974.

Lundin, R., Investigations of auroral electron precipitation by means of sounding rockets, KGI Report No 77:1, April 1977.

Maehlum, B.N., and H. Boestue, High temporal and spatial resolution observations of low energy electrons by a mother-daughter rocket in the vicinity of two quiescent auroral arcs, Planet. Space Sci., 21, 1957, 1973.

Marklund, G., L. Block, and P.-A. Lindqvist, Rocket measurements of electric fields, electron density and temperature during the three phases of auroral substorms, Planet. Space Sci., 29, 249, 1981.

Marklund, G., I. Sandahl, and H. Opgenoorth, A study of the dynamics of a discrete auroral arc, Planet. Space Sci., 30, 179, 1982.

Marklund, G., W. Baumjohann, and I. Sandahl, Rocket and ground based-study of an auroral breakup event, Planet Space Sci., 31, 207, 1983.

Maynard, N.D., Electric field measurements across the Harang-Discontinuity, J. Geophys. Res., 79 4620, 1974.

McPherron, R.L., Growth phase of magnetospheric substorms, J. Geophys. Res., 75, 5592, 1970.

Meng, C.-I., B. Mauk, and C.E. McIlwain, Electron precipitation of evening diffuse aurora and its conjugate electron fluxes near the magnetospheric equator, J. Geophys. Res., 84, 2545, 1979.

Mozer, F.S., and P. Lucht, The average auroral zone electric field, J. Geophys. Res., 79, 1001, 1974.

Olson, W.P., and K.A. Pfitzer, A quantitative model of the magnetospheric magnetic field, J. Geophys. Res., 79, 3739, 1974.

Persson, H., Electric field along a magnetic line of force in a low density plasma, The Physics of Fluids, Vol 6, Nr 12, December 1963.

Rearwin, S., and E.W. Hones; near simultaneous measurement of low-energy electrons by sounding rocket and satellite, J. Geophys. Res., 79, 4322, 1974.

Riedler, W., On the properties of cylindrical electrostatic analyzers in rocket and satellite instruments, Arkiv f. Geofysik, 5, 42, 1971.

Roederer, J.G., Dynamics of geomagnetically trapped radiation, Eds. J.G. Roederer, Denver and J. Zähringer, Heidelberg, Springer-Verlag, Berlin, Heidelberg, New York, 1970.

Rostoker, G., Classification of polar magnetic disturbances, J. Geophys. Res., 74, 5161, 1969.

Rostoker, G., Polar magnetic substorms, Rev. Geophys., 10, 157, 1972a.

Rostoker, G., Interpretation of magnetic field variations during substorms. In Earth's magnetospheric processes, Edited by B.M. McCormac, p. 379, 1972b.

Rostoker, G., S.-I. Akasofu, J. Foster, R.A. Greenwald, Y. Kamide, K. Kawasaki, A.T.Y. Lui, R.L. McPherron, and C.T. Russell, Magnetospheric Substorms - Definition and Signatures, J. Geophys. Res., 85, 1663, 1980.

Sandahl, I., Pitch angle scattering and particle precipitation in a pulsating aurora - an experimental study, KGI Report No 185, 1964.

Sandahl, I., L. Eliasson, and R. Lundin, Electron spectra over discrete auroras as measured by the Substorm-GEOS rocket, Proceedings of the 5th ESA-PAC Symposium on European Rocket & Balloon Programmes & Related Research - Bournemouth (UK), 14-18 april 1980 - (ESA SP-152 June 1980 a).

Sandahl, I., L. Eliasson, and R. Lundin, Rocket observations of precipitating electrons over a pulsating aurora, Geophys. Res. Lett., 7, 309, 1980 b.

Schield, M.A., J.W. Freeman, and A.J. Dessler, A source for field-aligned currents at auroral latitudes., J. Geophys. Res, 74, 247, 1969.

Sharp, R.D., D.L. Carr, R.G. Johnson, and E.G. Shelley, Coordinated auroral-electron observations from a synchronous and a polar satellite, J. Geophys. Res., 76, 7669, 1971.

Silsbee, H.C., and E.H. Vestine, Geomagnetic bays, their frequency and current systems, Terrest. Magnetism, 47, 195, 1942.

Steen, Å, and G. Gustafsson, The spectral hardening associated with the westward travelling surge, Planet. Space Sci., 29, 1011, 1981.

Störmer, C., The polar aurora, Oxford Claredon Press, Oxford Univ., London, England, 1955.

Swift, D.W., On the formation of auroral arcs and acceleration of auroral electrons, J. Geophys. Res., 80, 2096, 1975.

Vasyliunas, V.M., Low energy particle fluxes in the geomagnetic tail, in The Polar Ionosphere and Magnetospheric Processes, edited by Gunnar Sklovi, Gordon and Breach, New York, 1970.

Whalen, B.A., and I.B. McDiarmid, Pitch angle diffusion of low energy auroral electrons, J. Geophys. Res., 78, 1608, 1973.

Zanetti, L.J., T.A. Potemra, J.P. Doering, J.S. Lee, R.L. Arnoldy, and R.A. Hoffman, Coincident particle observations from AE-C and ATS 6 during the October 28, 1977, Geomagnetic storm, J. Geophys. Res., 85, 4563, 1980.